2015

Image-Based Modeling of Porous Media Using FEM and Lagrangian Particle Tracking

Paula Cysneiros Sanematsu
Louisiana State University and Agricultural and Mechanical College

IMAGE-BASED MODELING OF POROUS MEDIA USING FEM AND LAGRANGIAN PARTICLE TRACKING

A Dissertation

Submitted to the Graduate Faculty of the
Louisiana State University and
Agricultural and Mechanical College
in partial fulfillment of the
requirements for the degree of
Doctor of Philosophy

in

The Interdepartmental Program in Engineering Science

by
Paula Cysneiros Sanematsu
B.S., Siena Heights University, 2007
M.S., University of Tennessee Space Institute, 2010
December 2015

Acknowledgements

I would like to thank my advisor, Dr. Clinton Willson, for his time, encouragement, and mentoring. I also would like to thank my co-advisor, Dr. Karsten Thompson, for his guidance and support. This dissertation would not be possible without their help, guidance, support, and patience. I greatly appreciate the help of my committee members, Dr. Dimitris Nikitopoulos and Dr. Krishnaswamy Nandakumar, who offered valuable suggestions and contributed to improve my project.

I would like to thank Louisiana State University Graduate School Economic Development Assistantship for the financial support during the four years as a doctoral student as well as ExxonMobil Upstream Research Company and Advanced Energy Consortium for their financial support.

To my fellow graduate students, Yijie, Tim, Godfrey, and Seth, thank you for the support during this journey.

And to those outside the school, my parents and my husband, thank you for the endless patience and support.

Table of Contents

Abstract

The study of fundamental flow and transport processes at the pore scale is essential to understanding how the mechanisms affect larger, field-scale, processes that occur in oil and gas recovery, groundwater flow, contaminant transport, and CO_2 sequestration. Pore-scale imaging and modeling is one of the techniques used to investigate these fundamental mechanisms. Although extensive development of pore-scale imaging and modeling has occurred recently, some areas still need further advances. In this work, we address two areas: (1) imaging of bulk proppants and proppant-filled fractures under varying loading stress and flow simulation in these systems and (2) nanoparticle (NP) transport modeling in porous media. These are briefly explained below.

Rock fracturing, followed by proppant injection, has been used for years to improve oil and gas production rates in low permeability reservoirs and is now routinely used in low-permeability resources such as a shales and tight sands. While field data makes clear the effectiveness of this technique, there is still much room to improve on the science, including how the proppant-filled fracture system responds to changes in loading stress which affect permeability and conductivity. Here, we use high-resolution x-ray computed tomography (XCT) to image two unsaturated rock/fracture/proppant systems under a series of stress levels typical of producing reservoirs: one with shale, one with Berea sandstone. The resulting XCT images were segmented, analyzed for structural and porosity changes, and then used for image-based flow modeling of Stokes flow using both finite element (FEM) and Lattice Boltzmann methods.

NPs have been widely used commercially and have the potential to be extensively used in petroleum engineering as stabilizers in enhanced oil recovery operations or as tracers or

sensors to detect rock and fluid properties. In this work, we describe a Lagrangian particle tracking algorithm to model NP transport that can be used to better understand the impact of pore-scale hydrodynamics and surface forces on NP transport. Two XCT images, a Berea sandstone and a 2.5D micromodel, were meshed and used for image-based flow modeling of FEM Stokes flow. The effects of particle size, surface forces, flow rate, particle density, surface capacity, and surface forces mapped to XCT-image based mineralogy were studied.

1. Summary

This work uses x-ray computed tomography (XCT) to image and characterize porous media at the pore scale in three dimensions (3D). Image-based computational fluid dynamics and particle tracking simulations are then used to study fundamental flow and transport processes. Particular interest is given to Berea sandstone, proppant packs, and proppant-filled fractures due to their importance in oil and gas production.

1.1 Objectives

The study of fundamental flow and transport processes at the pore scale is essential to understanding how the mechanisms affect larger, field-scale, processes that occur in oil and gas recovery, groundwater flow, contaminant transport, and CO_2 sequestration. Pore-scale imaging and modeling is one of the techniques used to investigate these fundamental mechanisms. It has evolved tremendously in the past decade; from basic research of fundamental displacement processes to commercial exploitation with several companies providing "digital core analysis" (Blunt et al., 2013).

Although extensive development of pore-scale imaging and modeling has occurred recently, some areas still need further advances. In this work, we address two areas: (1) imaging of bulk proppants and proppant-filled fractures under varying loading stress and flow simulation in these systems and (2) nanoparticle (NP) transport modeling in porous media. These are briefly explained below.

Proppants are used in hydraulic fracturing – now a common technique used in unconventional reservoirs – to "prop" the fracture open after the hydraulic fracturing fluid retreats. Proppant arrangement directly impacts flow patterns which, in turn, is likely to affect oil and gas production. Additionally, it is reasonable to argue that proppant

arrangement is different at various depths due to the increased pressure within the Earth. Previous studies investigated the impact of loading stress (i.e., pressure) on permeability using loading cells (e.g, Cooke (1973); Much and Penny (1987), for more information, refer to Chapter 3). However, visualization of the pore space during the experiment was not possible. Therefore, the objectives in this first area are:

1. Use x-ray computed tomography to characterize: proppant packs, proppant-filled fractures, and reservoir rocks under varying loading stress.
2. Investigate the impact of high loading stress on proppant arrangement and flow behavior by using image-based flow modeling.

And some of the research questions that we aim to answer are:

1. Does the decrease in pore space due to increase in loading stress cause permeability reduction in the proppant-filled fractures?
2. How are the flow patterns affected when the pore space and morphology are changed?
3. Is permeability reduction due to the increased loading stress greater in proppant monolayer than in bulk proppant?

Nano engineered materials have emerged as a new technology with application across various areas such as drug delivery, contaminant remediation, enhanced oil and gas recovery, and cosmetics. Applications of NPs for oil and gas industry have great potential to create and improve processes in reservoir characterization and enhanced oil recovery. Current temperature and pressure tools can only be used near the wellbore, hence the development of nanosensors that travel through the reservoir and provide temperature and pressure measurements would greatly improve reservoir characterization (Alaskar et al., 2012).

Another idea is the use nanotracers that also travel through the reservoir but are detectable by seismic imaging or nuclear magnetic resonance. Moreover, nanosilica-stabilized CO_2 foam has been shown to improve oil recovery (Mo et al., 2014). These are a few examples of the many applications of NPs in oil and gas industry. Thus, it is important to understand how these NPs behave in the porous medium to assess the capabilities and limitation of NPs as sensors, tracers, or surfactants. Particularly, we are interested in NP transport in porous media at the pore scale and the mechanisms that cause retention and/or facilitated transport of NPs.

The studies that address NP transport in porous media generally use column experiments. Although they provide valuable information (e.g., effluent curves, adsorption rates), some details remain hard to identify, especially those related to visualization of NPs inside the porous media as, for example, location of adsorption sites and the effect of complex geometry at the pore scale. Another common approach to study NP transport in porous media, the modified colloid filtration theory (CFT), has brought new insights and improved our understanding about the mechanisms that affect NP retention. However, as with column experiments, it does not provide locations and visualization of retention sites. Thus, we aim to address some of these problems by simulating flow and NP transport in 3D images of rocks obtained through XCT. The objectives of this investigation are:

1. Develop a NP transport tracking code, based on first principles of physics, that will simulate NP transport in porous media. This program will be a tool to study the effect of porous medium geometry, flow rate, particle size, and particle-surface forces on NP retention behavior.

2. Use the developed model to provide: effluent concentration, location and concentration of adsorption sites. These results can be used as adsorption coefficients for field-scale simulations.
3. Use the developed model to understand how complex geometry of porous media affect NP transport.
4. Include realistic surface forces obtained from experimental and/or computational work.
5. Make this program user-friendly such that students/researchers can use it in the future.

1.2 Description

Chapter 2 provides a literature review on x-ray computed tomography, image-based pore-scale flow modeling, and NP transport modeling. Chapter 3 presents a manuscript on our first topic: imaging of bulk proppants and proppant-filled fractures under varying high loading stress and flow simulation in these systems. Chapter 4 presents the current work on the second topic: nanoparticle transport model, including assumptions, methods, preliminary results and limitations, and issues to be addressed.

1.3 Bibliography

Alaskar, M., Ames, M., Connor, S., Liu, C., Cui, Y., Li, K., and Horne, R. (2012). Nanoparticle and Microparticle Flow in Porous and Fractured Media: An Experimental Study. *SPE Journal*, 17(04):1160–1171. 10.2118/146752-PA. 2

Blunt, M. J., Bijeljic, B., Dong, H., Gharbi, O., Iglauer, S., Mostaghimi, P., Paluszny, A., and Pentland, C. (2013). Pore-scale imaging and modelling. *Advances in Water Resources*, 51:197–216. 10.1016/j.advwatres.2012.03.003. 1

Cooke, C. E. (1973). Conductivity of fracture proppants in multiple layers. *Journal of Petroleum Technology*, 25(09):1101–1107. 10.2118/4117-PA. 2

Mo, D., Jia, B., Yu, J., Liu, N., and Lee, R. (2014). Study nanoparticle-stabilized co2 foam for oil recovery at different pressure, temperature, and rock samples. In *SPE Improved Oil Recovery Symposium*, pages 1–11. 10.2118/169110-MS. 3

Much, M. and Penny, G. (1987). Long-term performance of proppants under simulated reservoir conditions. In *Low Permeability Reservoirs Symposium*, page 10, Denver, Colorado. Society of Petroleum Engineers. 10.2118/16415-MS. 2

2. Introduction

Flow in porous media occurs in many commonly known natural and engineered systems such as groundwater, contaminant transport and remediation, oil and gas exploration, geothermal energy production, CO_2 sequestration, packed beds, and membranes. It also occurs in some unusual cases in absorbent hygiene products like diapers, paper towels, wipes, and textile products like cotton and fabrics. Understanding the details of how fluids behave and how particles are transported in porous media can enhance our understanding of the process' physics. This, in turn, allows us to create more effective and efficient processes and/or products. For example, when Hassanizadeh and Gray (1993) presented that capillary pressure is an intrinsic property rather than hysteretic as believed until then, a finding that was based on fundamental principles of thermodynamics developed by Gray and Hassanizadeh (1991) and Hassanizadeh and Gray (1990).

Methods of investigating porous media include: core flood experiments, field data, imaging, serial sectioning, and two and two and half dimensional (2D and 2.5D) micromodels. Core flood experiments provide valuable effluent information for real materials, but when microscopic adsorption information is necessary, samples must be milled and analyzed, destroying samples and not allowing an exact replication of the experiment.

For this work, x-ray computed tomography (XCT) is used because it is a non-destructive technique that provides visualization in three dimensions (3D) and information at the microscopic level (i.e. micro scale or pore scale) that traditional methods fail to provide or are cumbersome (e.g. serial sectioning). Some advantages of this method when compared to others include:

- Three dimensions: images retain pore connectivity and packing structure information (Wildenschild and Sheppard, 2013)
- Non destructive: allows multiple analyses and comparisons
- Ease of image interpretation: x-ray attenuation of each material closely relates to its density, making the interpretation straightforward (Ketcham and Carlson, 2001)
- Analysis: digital data allow the use of computational methods for fast image analysis (Ketcham and Carlson, 2001)

2.1 X-Ray Micro Computed Tomography

2.1.1 Brief History

Wilhelm Röntgen discovered x-rays in 1895 (Röntgen, 1896), but the advancement of tomography (i.e. the superimposition of 2D projections to create a 3D image) was developed a few decades later in the late 1960s for medical purposes, when Hounsfield (1973) used Radon transform (Radon, 1917) to reconstruct 2D projections at different angles into a 3D image. Laboratory experiments using medical x-ray computed tomography were first used to study porous media in the 1980s. Sato et al. (1981) led the progress of laboratory-based x-ray micro-tomography while investigating optic fibers. In the following year, Elliott and Dover (1982) studied the shell of a freshwater snail (*Biomphalaria glabrata*) and later a human femur (Elliott and Dover, 1985). In wood technology, computed tomography was used by Onoe et al. (1984) to study annual rings of trees and by Taylor et al. (1984) to find internal knots of pine and red oak logs. In soil sciences, Petrovic et al. (1982) successfully measured soil bulk density, Crestana et al. (1985) measured soil water content and the same group but led by Vaz et al. (1989) later investigated soil compactation. In petroleum engineering, Vinegar and

Wellington (1987) analyzed relative saturation of up to three phases and Coles et al. (1991) investigated bulk density and porosity of cores as well as water saturation and distribution. Flannery et al. (1987) used for the first time both laboratory and synchrotron sources to characterize rocks. An extensive review of XCT history including evolution of hardware and techniques utilized to achieve better resolution and mitigate noise can be found in Ketcham and Carlson (2001); Cnudde and Boone (2013); Wildenschild and Sheppard (2013).

2.1.2 Conventional *vs.* Synchrotron

Two sources of x-ray radiation are commonly used in porous media research: conventional (laboratory based) and synchrotron. Figure 2.1 illustrates the major difference: conventional source produces a cone or fan beam whereas synchrotron produces a high intensity beam that passes through a monochromator and generates a parallel beam. Although monochromators have been used in conventional sources for clinical purposes (Zhong et al., 2001; Bingölbali and MacDonald, 2009), they generally deplete the source so much that noisy images would be generated and long scan times would be necessary (Wildenschild and Sheppard, 2013). Therefore, the use of monochromators is more common in synchrotrons because of its adequate high intensity (Bingölbali and MacDonald, 2009), a million times brighter than conventional sources (Wildenschild and Sheppard, 2013). Apart from this difference, the rest of the of the apparatus is fairly similar. After x-ray radiation passes through the sample and is attenuated, a scintillator converts x-ray radiation into visible light which is generally magnified by optical devices before it is captured by charge-coupled-device (CCD) or complementary-metal-oxide-semiconductor (CMOS) camera (Wildenschild and Sheppard, 2013). The sample is rotated and a 2D projection is captured at different angles; as resolution

increases, the angle interval needs to be smaller, increasing the number of 2D projections (Wildenschild and Sheppard, 2013). Each projection represents the transformation of the sample attenuation values from its plane onto the camera's plane, where corresponding points are connected between planes by parallel lines (Weisstein).

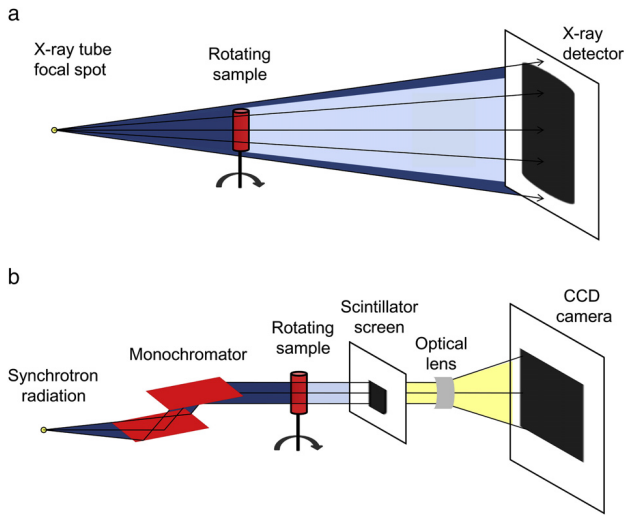

Figure 2.1: (a). Conventional and (b) synchrotron setups (from Cnudde and Boone (2013))

Main advantages and disadvantages of these two sources include:

- Synchrotron x-ray radiation requires a large facility: the Advanced Photon Source at Argonne National Laboratory (Argonne, Illinois, USA), where the data for this study was collected, has a storage ring that is 1104 m long with more than 1,000 electromagnets (APS).
- Accessibility: Conventional sources can be used in laboratories in universities and companies and are sold by more than 15 vendors worldwide (Wildenschild and Sheppard, 2013).
- Tune necessary energy for synchrotron: the use of monochromators enables one to choose narrow ranges of energy (Grodzins, 1983; Wildenschild and Sheppard, 2013).

This is a great advantage when specific energy is necessary for K-edge subtraction imaging. K-edge occurs when an element suddenly increases its attenuation coefficient because the photon energy is just above the K shell electron's biding energy (Fosbinder and Orth, 2011). Thus, a substance (e.g. iodine) can be added to a phase and imaging acquisition is done at below and above the element's K-edge providing good phase contrast between the below and above images (Dilmanian et al., 1997).

- Acquisition time: synchrotron acquisition times are much faster than conventional, the former requiring typically 10-15 minutes whereas the latter ranges from 15 minutes to 24 hours, depending on resolution, exposure time, and energy level (Wildenschild and Sheppard, 2013).
- Beam hardening: due to the polychromatic beam of conventional sources, the lower energies (soft x-rays) are absorbed more and mostly the higher energies (harder x-rays) penetrate deeply into the material causing the outer material to have a higher attenuation than the inner material (Cnudde and Boone, 2013; Ketcham and Carlson, 2001; Wildenschild and Sheppard, 2013). To minimize this problem, filters may be employed to pre- or post-harden the x-ray beam so the beam is attenuated before reaching the sample (Ketcham and Carlson, 2001). However, this procedure diminishes the quality of the beam, which could lead to noisier images unless acquisition time is adjusted (Ketcham and Carlson, 2001).

2.1.3 Reconstruction

After many projections are captured by the camera at different angles, it is necessary to combine these projections to compile a 3D image. Reconstruction is the process of recovering an object from its projections (Fessler, 2014). There are four main approaches to reconstruction: analytical, iterative, statistical, and model based.

2.1.3.1 Analytical Methods

Analytical methods are based on simplified models (for example, by assuming continuous measurements) and provide fast solutions (Beister et al., 2012; Fessler, 2014). Although fast, analytical methods require filtering methods to remove noise and artifacts (Li et al., 2004; Beister et al., 2012). Many models emerged after Hounsfield (1973) used Radon transforms (Radon, 1917) for the first time to reconstruct an image, such as back projection, direct Fourier, and filtered back projection (Fessler, 2014). Although the filtered back projection algorithm was developed thirty years ago (Feldkamp et al., 1984), modifications of this algorithm continue to be extensively used. Pan et al. (2009) even inquired and studied why filtered back projection has been the main reconstruction algorithm and why new algorithms have not been developed. An extensive historical review can be found in Defrise and Gullberg (2006) and detailed explanation of main analytical reconstruction methods is provided in books by Natterer and Wübbeling (2001), Deans (2007), and Fessler.

2.1.3.2 Iterative Methods

Iterative methods reconstruct an image by repeatedly computing a forward projection, followed by a back projection, until a fixed number of iterations or a convergence criterion is reached (Beister et al., 2012). *A priori* information may be given, for example, by a

filtered back projection reconstruction, which generally improves convergence (Beister et al., 2012). Because iterative methods remove some noise and artifacts during reconstruction, they provide better images than analytical methods (Beister et al., 2012; Fessler, 2014). Although successful, they are extremely computationally intensive (Agulleiro and Fernandez, 2011; Beister et al., 2012; Fessler, 2014), a major limiting factor for their advancement and usage (Pan et al., 2009). They were first proposed in the 1970s (Budinger and Gullberg, 1974; Brooks and Chiro, 1976), but only recently have become a more realistic option due to the improvement of processing units (CPU) and recent use of graphics processing units (GPU) (Agulleiro and Fernandez, 2011; Beister et al., 2012). Beister et al. define statistical methods as an algorithm that assumes photons have a Poisson distribution and this information is incorporated into the iterative reconstruction. This definition varies and some authors have a broader definition of statistical methods. For methods that include geometrical, physical, and more statistical information, Beister et al. define them as model-based methods. To explain the details of statistical and model-based methods is beyond the scope of this work. A review of iterative methods can be found in Beister et al. and more detailed information about various methods is described in De Man and Fessler (2010) and Fessler.

2.1.4 Filtering

Filtering is a post-processing method that consists on sharpening the features of interest. For medical purposes, the objective may be emphasizing soft tissue. For porous media XCT, the objective of filtering is to remove noise by smoothing homogeneous regions and maintaining sharp edges (Schlüter et al., 2014), as shown in Figure 2.2, where anisotropic diffusion filter was applied in a Berea sandstone XCT image – the gray scale was smoothed

within the grains while maintaining edges. There are thousands of filtering methods (Wildenschild and Sheppard, 2013); to give a general idea, Avizo – a common but expensive visualization software – and Matlab provide over ten filters each and Mathematica over thirty.

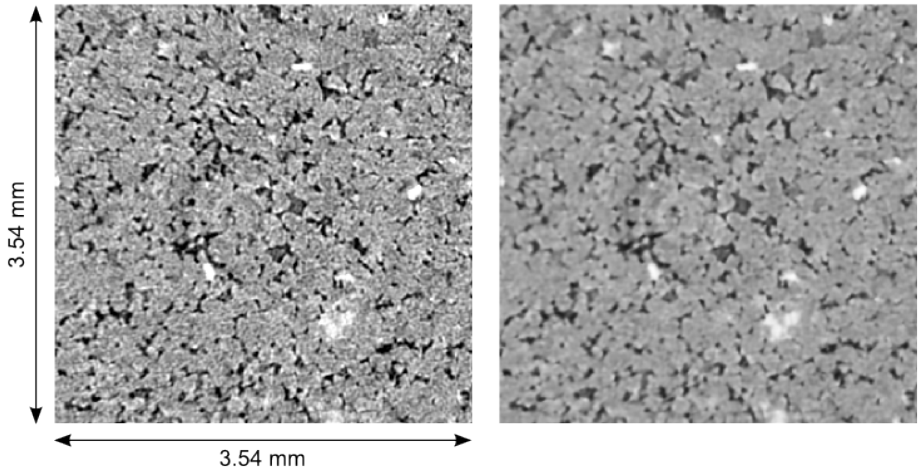

Figure 2.2: Left: raw XCT image before filtering. Right: anisotropic diffusion filter (Section 2.1.4.2) applied to the raw image.

In XCT, it is important to use a filter that accounts for the 3D geometry, for otherwise the full image information would not be used. Most filtering methods operate in 2D and are too computationally intensive to apply in large 3D images (Wildenschild and Sheppard, 2013). Buades et al. (2005a) provides an extensive review of 2D methods. 3D filtering methods used in XCT for porous media include linear and nonlinear filters. Linear filters, like Gaussian and mean, reduce noise but also blur edges (Zhong et al., 2004; Kaestner et al., 2008). Nonlinear filters better preserve edges while smoothing homogeneous regions (Kaestner et al., 2008; Schlüter et al., 2014). A brief description of main filters is given below.

2.1.4.1 Median Filter

Median filter is the simplest nonlinear filtering algorithm (Schlüter et al., 2014) first developed by Tukey (1977) and has been continuously improved (Huang et al., 1979; H and Haddad, 1995; Esakkirajan et al., 2011). It uses convolution ($*$) between the raw image u_0 and the median M of a region of diameter d at location $\mathbf{x}$ (Schlüter et al., 2014):

$$u(\mathbf{x}) = u_0(\mathbf{x}) * M_d(\mathbf{x}) \tag{2.1}$$

where u is the filtered intensity values.

This filter performs well in the presence of outliers, but because it is spacially invariant, it tends to smooth sharp edges as well (Kaestner et al., 2008).

2.1.4.2 Anisotropic Diffusion Filter

Perona and Malik (1990) first introduced this filter for edge detection by using a nonlinear function g controlled by the amplitude of the gradient as the diffusion coefficient:

$$\begin{aligned} u(0) &= u_0 \\ \frac{\partial u}{\partial t} &= \nabla \cdot [g(|\nabla u|)\nabla u] \end{aligned} \tag{2.2}$$

where t is the numerical time and u is short for $u(\mathbf{x}, t)$. The idea is to smooth homogeneous areas and perform almost no smoothing where the gradient is high, i.e. at the edges (Catté et al., 1992). A drawback mentioned by Perona and Malik is that the presence of noise may give oscillating gradients. To overcome this issue, Catté et al. introduced "selective smoothing" by using the gradient of a convolution between a Gaussian G with standard

deviation σ and the smoothed intensity values u:

$$\begin{aligned} u(0) &= u_0 \\ \frac{\partial u}{\partial t} &= \nabla \cdot \left[g\left(\left| \nabla \left(G_\sigma * u \right) \right| \right) \nabla u \right] \end{aligned} \tag{2.3}$$

Now, smoothing of the intensity values occurs "if and only if the gradient is estimated to be small" (Catté et al.). Schlüter et al. (2014) present the simplest implementation:

$$g\left(\left| \nabla \left(G_\sigma * u \right) \right| \right) = \begin{cases} 1, & \left| \nabla \left(G_\sigma * u \right) \right| \leq \lambda, \\ 0, & \left| \nabla \left(G_\sigma * u \right) \right| > \lambda, \end{cases} \tag{2.4}$$

where λ is the diffusion stopping criterion. By modifying the parameters for intensity level λ and the Gaussian region given by σ, different smoothing effects can be obtained (Kaestner et al., 2008). It is also important to set the maximum number of iterations manually, because otherwise the solution converges to a uniform intensity (Schlüter et al., 2014).

PDE-based filters require a lot of computer memory reaching up to seven times the image size, but can be highly improved by redesigning the filter algorithm implementation (Kaestner et al., 2008). Another drawback is the poor performance in flat regions (Buades et al., 2005a).

Anisotropic diffusion filters are available in open source from library ITK.

2.1.4.3 Total Variation Filter

Total variation is another nonlinear filter based on a partial differential equation (PDE), but with a different approach than anisotropic diffusion (Rudin et al., 1992). It uses a

minimization of a functional:

$$\min_u = \left[\underbrace{J(u)}_{\text{regularization}} + \underbrace{\beta H(u_0, u)}_{\text{fidelity}} \right] \tag{2.5}$$

where β is a scale parameter that controls the balance between fidelity of the original intensity values u_0 and the smoothing (or regularization). The solution is obtained by solving the system of coupled PDEs (Kaestner et al., 2008; Schlüter et al., 2014):

$$\begin{aligned} u(0) &= u_0 \\ \frac{\partial u}{\partial t} &= -p(u) + \beta q(u_0 + v, u) \\ \frac{\partial v}{\partial t} &= \alpha q(u_0, u) \end{aligned} \tag{2.6}$$

where $\alpha \leq \frac{1}{4}$ (Lie and Nordbotten, 2007) and $\beta \ll 1$ (Kaestner et al., 2008). For this algorithm, the fidelity term prevents the solution from converging to a uniform intensity and thus the maximum number of iterations is not as important (Schlüter et al., 2014).

Similarly to the anisotropic diffusion filter (Section 2.1.4.2), the total variation filter maintains edges but can smooth textures too much (Kaestner et al., 2008).

2.1.4.4 Shock Filter

This is another PDE-based filter first introduced by Osher and Rudin (1990):

$$\begin{aligned} u(0) &= u_0 \\ \frac{\partial u}{\partial t} &= -\left|\nabla u\right| \operatorname{sign}\left(\nabla^2 u\right) \end{aligned} \tag{2.7}$$

where ∇^2 is the Laplacian operator. This filter enhances every rapid change, including outliers due to noise (Kaestner et al., 2008). To avoid the enhancement of noise, Alvarez and Mazorra (1994) added an anisotropic diffusion term to Eq. (2.7) and Kaestner et al. rewrote it to include the curvature H in the diffusion term:

$$\begin{aligned} u(0) &= u_0 \\ \frac{\partial u}{\partial t} &= c\,|\nabla u|\,H - |\nabla u|\,\mathrm{sign}\left(\nabla_\sigma^2 u\right) \end{aligned} \tag{2.8}$$

where c determines how much smoothing is added and σ indicates the Laplacian uses a Gaussian filter. This extra term adds diffusion perpendicular to ∇u, smoothing both sides of edges, but maintaining the edge (Alvarez and Mazorra, 1994). The original term – but now slightly modified by the Gaussian filter – has a shock effect perpendicular to the edge (Kaestner et al., 2008).

The shock filter is suitable for images with smooth edges and low spatial noise correlation because, when high noise correlation is present, noise regions are enhanced as features unless a lot of diffusion is added (Kaestner et al., 2008).

2.1.4.5 Nonlocal Means Filter

Nonlocal means is a linear filter that can potentially use the information of the entire image to change a pixel value – unlike means filter that uses the information from local neighbors (Schlüter et al., 2014). Nonlocal means filter was developed by Buades et al. (2005a) to overcome some of the shortcomings of Gaussian and anisotropic diffusion filters (Section 2.1.4.2). It uses a weighting function, W, to smooth the original image, u_0 with

domain Ω, at pixel $\mathbf{x} \in \Omega$:

$$u(\mathbf{x}) = \frac{1}{C(\mathbf{x})} \int_{\Omega} u_0(\mathbf{y}) W(\mathbf{x}, \mathbf{y}) d\mathbf{y} \tag{2.9}$$

where

$$C(\mathbf{x}) = \int_{\Omega} W(\mathbf{x}, \mathbf{y}) d\mathbf{y} \tag{2.10}$$

$$W(\mathbf{x}, \mathbf{y}) = \exp\left[-\frac{(G_\sigma * \|u_0(\mathbf{x} + .) + u_0(\mathbf{y} + .)\|^2)}{h^2} \right] \tag{2.11}$$

C is a normalizing factor, W is a Gaussian weighted Euclidean distance between image neighborhoods centered at $\mathbf{x}$ and $\mathbf{y}$, σ is the standard deviation of the Gaussian kernel, and h is a filtering parameter that gives the degree of filtering (Buades et al., 2005a, 2011). The weighting function gives larger weights for the pixel neighborhoods that are similar; this means that W not only considers the grey value of a single pixel, but also its neighborhood geometry (Buades et al., 2005b)

Nonlocal means filter can be computationally intensive while searching neighborhoods in a big image, which may require restriction of the neighborhood area (Schlüter et al., 2014). To overcome computational cost, Avizo uses an accelerated implementation on multiple cores or on GPUs (Avizo, 2013).

An open source implementation if available in Buades et al. (2011).

2.1.5 Segmentation

In computed tomography, segmentation (Figure 2.3) is the process of separating discrete phases in a reconstructed XCT image, commonly performed for two phases at a time (i.e.

binarization) (Iassonov et al., 2009; Wildenschild and Sheppard, 2013), but can also be performed in multiple phases simultaneously such as rock matrix, air, and oil (Schlüter et al., 2014). Segmentation is the most critical process because it affects all subsequent quantitative analysis (Cnudde and Boone, 2013; Houston et al., 2013; Iassonov et al., 2009; Schlüter et al., 2014; Tuller et al., 2013). Once each phase is separated, then pore-scale parameters – porosity, pore connective, specific surface area, saturation, etc. – can be determined (Iassonov et al., 2009).

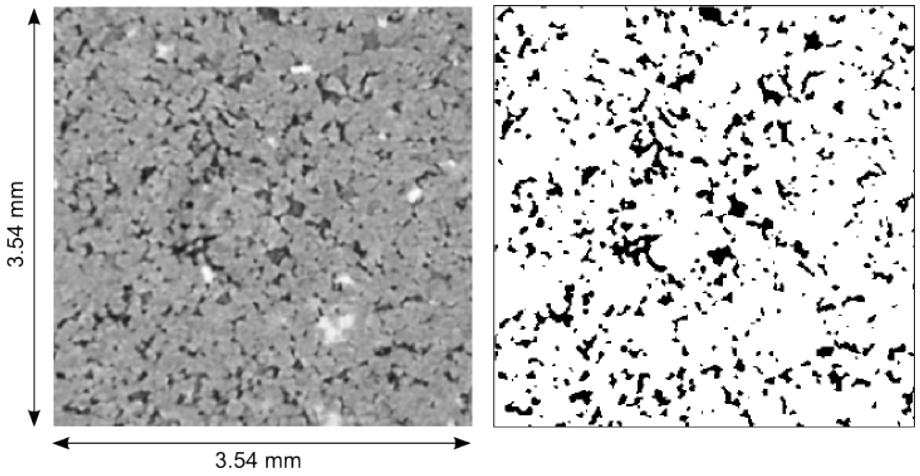

Figure 2.3: Left: anisotropic diffusion (Section 2.1.4.2) filtered image of a Berea sample applied to the raw image. Right: segmented image using indicator kriging (Section 2.1.5.2).

Segmentation can be automated or require input from a skilled operator. In theory, automated methods would be preferable because they are faster and also eliminate operator bias (Wildenschild and Sheppard, 2013). However, results from operator-based methods have been more reliable and consistent than automated methods (Iassonov et al., 2009; Wildenschild and Sheppard, 2013) because automated methods are unable to produce consistent results when images from the same sample have small differences (Wildenschild and Sheppard, 2013).

Over a hundred segmentation methods have been published, most with application outside of geomaterials (Iassonov et al., 2009). Each method is optimal to a certain instrument and sample; for example, images of glass beads are extremely high quality when compared with soil samples, and an optimal method for glass beads may not be useful for soil (Wildenschild and Sheppard, 2013). Here, the main segmentation methods for geomaterials are presented. For a good comparison of segmentation methods refer to Iassonov et al.; Pal and Pal (1993); and Schlüter et al. (2014).

2.1.5.1 Global Thresholding

This is the most common segmentation method (Iassonov et al., 2009). A value from the image histogram[1] is chosen that separates two different phases (Iassonov et al., 2009). For an n-phase segmentation, $n-1$ threshold values are chosen. Many approaches exist to find the optimal threshold value and they can classified into subcategories based on the information used, for example (Iassonov et al., 2009; Sezgin and Sankur, 2004):

- Histogram shape
- Background and foreground (object) gray scales or entropy
- Similarity between grey scale and binary images by a certain function (e.g. fuzzy shape)
- Higher-order probability distribution of pixels

A good description and comparison of thresholding methods is given by Sezgin and Sankur.

Iassonov et al. (2009) compared many thresholding methods for geomaterials scanned in both conventional and synchrotron systems. They obtained poor and/or inconsistent results

[1] A histogram shows the image gray scale distribution

except for the methods by Otsu (1979) and Kittler and Illingworth (1986). Images with low contrast and partial volume effects produced even worse results. The authors concluded that thresholding methods are not suitable for images with unimodal histograms. However, they also asserted that better techniques for filtering (a median filter was used) could have produced better results.

2.1.5.2 Indicator Kriging

This common method in the geosciences was first developed by Oh and Lindquist (1999) and improved by Bhattad et al. (2013) and Houston et al. (2013). Two *a priori* threshold values are defined by the user such that two phases are defined (i.e. one below the lower threshold value and one above the higher threshold value) and the range between threshold values remains unidentified (Oh and Lindquist, 1999). The assignment of these unidentified values are given by a weighted average (Schlüter et al., 2014), where the "weights are calculated from the two point spatial covariance relation calculated using smoothed indicators" (Bhattad et al., 2013).

Indicator kriging has been successfully used to segment clean synchrotron images (Porter and Wildenschild, 2009) and noisy images (Iassonov et al., 2009; Prodanović et al., 2007) and for multiphase segmentation (Bhattad et al., 2013; Schlüter et al., 2014). Nonetheless, Schlüter et al. point out that the segmentation process needs to be repeated $n-1$ times for n phases, a disadvantage when compared with other multiphase methods. The choice of the two thresholding values may also improve image segmentation (Iassonov et al., 2009).

2.1.5.3 Watershed

Watershed segmentation is emerging in the medical field (Wildenschild and Sheppard, 2013) and recently evaluated for geomaterials (Schlüter et al., 2014). To understand the watershed geographical/topographical concept, one can think of a gray scale image as a surface, where the dark areas represent basins or local minima and the brighter areas represent peaks or local maxima (Eddins, 2002). Suppose these local minima are slowly flooded. When the water from different basins meet, a watershed line is defined, where segmentation occurs (Roerdink and Meijster, 2001; Sheppard et al., 2004). A good graphical representation of the segmentation procedure is presented by Beucher (2010).

Summary of the watershed segmentation steps (Beucher, 2010; Schlüter et al., 2014) :

1. Create a gradient image from the original image
2. Use simple thresholding to determine local maxima and minima as seeding points for the immersion process
3. Perform immersion to find watershed lines
4. Voxels are assigned according to their predominant neighbors.

Watershed segmentation is generally applied to object detection in "topographic" data (Iassonov et al., 2009) and may not be optimal for geomaterials due to over segmentation.

2.1.5.4 Active Contours

Active contours (also called level set or snake) method was first proposed by Kass et al. (1988) with the intent of detecting edges, lines, subjective contours, and motion tracking. The idea is to evolve interfaces that start from seeding regions and converge to the nearest

edge by means of energy minimization (Kass et al., 1988; Sheppard et al., 2004). The specific energy term determines which feature (e.g. line, edge) is captured (Kass et al., 1988).

Although an appealing method, active contours is very computationally intensive – which can be aggravated by orders of magnitude depending on the speed at which the interface evolves (Sheppard et al., 2004). In addition, the energy minimization function can rarely be determined *a priori* (Sheppard et al., 2004).

2.1.6 Postprocessing

Noise in the gray scale image can be reduced by using filters before segmentation. When filtering prior to segmentation is not enough to produce segmented images without noise, postprocessing methods can help. Some examples include:

- Erosion and dilation: a common method to improve the morphology of the segmented image
- Filters: a simple filter (e.g. median, minimum and maximum) removes segmentation noise and phase boundaries badly defined (Schlüter et al., 2014)
- Object removal: the user defines a size such that objects smaller than this size and surrounded by another phase are removed and replaced by the surrounding phase.

2.1.7 Recent Advances

Advancements in beamlines and imaging processing have allowed development in different areas.

At GSECARS at APS, high loading pressure and high temperature experiments can be performed by using their large volume press (Wang et al., 2005b). This apparatus can simulate deep Earth environment of up to 8 GPa and allow the study and visualization of

geological formations. In a more recent study (Wang et al., 2011), the mechanical behavior of multiphase composites was studied under up to 6 GPa and 800 K.

In a recent study by Herring et al. (2013), they were able to image super critical CO_2 by controlling the hutch temperature and pressure. This is an important advancement for the study of CO_2 geologic sequestration to mitigate climate change.

Bésuelle et al. (2010) and Raynaud et al. (2008) have used a triaxial cell and XCT to understand rock physics, more specifically, they investigated different strain regimes (from brittle to ductile).

The advancement of imaging processing techniques coupled with multiphase segmentation allows the study of various materials altogether (rather than two materials at a time). This, in turn, allows the quantification of specific minerals and of multiphase flow processes such as drainage and imbibition. When minerals are determined, the effect of specific minerals on transport processes can be investigated.

2.2 Image-Based Pore-Scale Flow Modeling

There are two approaches to image-based flow modeling: direct and indirect methods.

Direct methods preserve the geometry of the image by discretizing the pore space and by using traditional computational fluid dynamics (CFD) to solve for flow and transport processes (Blunt et al., 2013; Joekar-Niasar et al., 2012; Shen, 2014). Common CFD methods used for flow in porous media are (1) continuum-based models such as finite difference (Manwart et al., 2002; Mostaghimi et al., 2012), finite element (Bird et al., 2014; Lane, 2011; Shen, 2014), and level set (Prodanović and Bryant, 2006) methods, and (2) particle-based models such as Lattice-Boltzmann (Hao and Cheng, 2010; Pan et al., 2004; Porter et al.,

2009) and smooth particle hydrodynamics (Ovaysi and Piri, 2010; Tartakovsky and Meakin, 2005). Honoring the porous media geometry and using first principle physics as governing equations are the obvious advantages of direct methods (Blunt et al., 2013; Joekar-Niasar et al., 2012; Thompson et al., 2008). However, they come at a high computational cost – especially Lattice-Boltzmann method (LBM) – which considerably limits the computational domain (Blunt et al., 2013; Joekar-Niasar et al., 2012; Thompson et al., 2008).

Fatt (1956) first introduced network modeling, an indirect method, with the idea of modeling flow as a network of tubes rather than a bundle of tubes – a more common approach at the time. Network modeling simulates flow in porous media by performing two levels of approximations (Thompson et al., 2008). First, a topologically representative network structure of the image pore space needs to be extracted (Blunt et al., 2013). Second, fluid dynamics need to be modeled by governing equations within the pore network (Thompson et al., 2008). Pore network models have extensively advanced and today include multi-phase flow (Joekar-Niasar and Hassanizadeh, 2012), inertial flow (Balhoff and Wheeler, 2009; Shen, 2014), non-Newtonian flow (Balhoff and Thompson, 2006; Lopez et al., 2003), reactive transport (Hannaoui et al., 2015; Kim and Lindquist, 2012), solute transport (Blunt et al., 2013), and multi-scale (Sheng and Thompson, 2013) processes. The main advantage of pore network modeling is its computational efficiency, allowing simulations in domains that are not feasible for direct methods. The major drawback of network modeling is the approximation of a heterogeneous and complex porous medium by simple geometric shapes and statistical parameters (e.g. pore connectivity, pore-throat aspect ratio, etc.) (Wildenschild and Sheppard, 2013). The representation depends on the method employed

to generate the pore network structure and may not be unique, even statistically (Blunt et al., 2013).

A brief explanation of pertinent methods to this work is given below. For more information of other methods, refer to detailed explanations from Blunt et al. (2013); Joekar-Niasar and Hassanizadeh (2012); and Meakin and Tartakovsky (2009).

2.2.1 Lattice Boltzmann Method

The idea of this particle-based method is to model the mean population of a lattice gas using Boltzmann equations (Succi et al., 1989). The solution of these equations approximates the incompressible Navier-Stokes equations for small Knudsen and Mach numbers and, therefore, well represents macroscopic flow behavior (Blunt et al., 2013; Succi et al., 1989). LBM uses particle streaming and collision to describe their motion with the following equation (Pham et al., 2014; Succi et al., 1989)

$$\underbrace{f_i(\mathbf{x}+\mathbf{e}_i\Delta t, t+\Delta t) = f_i(\mathbf{x},t)}_{\text{streaming}} + \underbrace{\Omega_i(\mathbf{x},t)}_{\text{collision}} \tag{2.12}$$

where f is the mean particle population at lattice i, $\mathbf{x}$ is the node position, $\mathbf{e}$ is the nodal velocity, t is the time, Δt is the time step, and Ω is the collision operator.

Succi et al. (1989) were among the first to use of LBM to simulate flow in complex geometries and Hazlett (1995) introduced the use of LBM on XCT images. Since then, the applications of LBM for porous media have evolved and now can simulate multi-phase flow (Pan et al., 2004; Porter et al., 2009; Schaap et al., 2007), multiscale flow (Kang et al., 2002), reactive transport (Hao and Cheng, 2010), solute transport (Mendoza et al., 2010), non-Newtonian flow (Boek et al., 2003), and non-Darcy flow (Chai et al., 2010). Some of

the main advantages of LBM include its ease of coding and parallelization, and adaptation to complex geometries (Blunt et al., 2013; Succi et al., 1989). However, even with massive parallel codes and the recent advance of computing power, the high computational demand limits the size of the simulation domain (Blunt et al., 2013; Wildenschild and Sheppard, 2013).

2.2.2 Finite Element Method

Although an established numerical technique with a wide range of applications in material deformation and stress analysis (e.g., aircraft and bridges) as well as in analysis of heat and magnetic fluxes and fluid flow (Chandrupatla and Belegundu, 1991), finite element method (FEM) has been seldom used in pore-scale modeling (Takbiri Borujeni et al., 2013). The idea behind FEM is to use simple geometric shapes – finite elements – to discretize complex continuum regions (Chandrupatla and Belegundu, 1991). Then, the material properties can be assigned to the elements and governing equations can be solved at the elements' nodes.

The use of unstructured grids is very suitable for porous media because the discretized pore space can (1) conform to the medium and (2) be refined in regions of interest (Takbiri Borujeni et al., 2013). The local refinement is a great advantage for heterogeneous systems because bigger pores can have coarse discretization whereas smaller features or areas of interest (e.g., pore throats, grain surface) can be finely discretized – this only increases computational cost at the necessary locations. The mesh generation (discretized domain) is, however, one of the major obstacles of FEM applied to porous media because of the high complexity of the mesh. The development of commercial software, such as Avizo and

COMSOL that allow mesh generation directly on the voxel image, has helped to overcome this problem.

Despite the use of FEM to simulate 2D Stokes and inertial flow in fibrous media as early as 1995 by Ghaddar, application of FEM to understand flow in porous media has been limited. For complex geometry such as XCT image-based (Akanji and Matthai, 2010) and complex physical processes such as non-isothermal two-phase flow (Akhlaghi Amiri and Hamouda, 2014), simulations were limited to a 2D domains. When performed in 3D (Chareyre et al., 2012; Fourar et al., 2004), geometries remained fairly simple (e.g., uniform sphere pack). As part of previous work in our research group, Lane (2011) developed a 3D FEM Stokes solver using an in-house mesh generation. These meshes were constructed based on 3D digital images that were computer generated or obtained by XCT. Their results were successfully validated against LBM simulations in Takbiri Borujeni et al. (2013). Bird et al. (2014) were another group that implement 3D XCT image-based FEM Stokes flow, but using the commercial software COMSOL. Due to computational constraints, their computational size was very limited (30-50 voxels on a side).

This study uses the 3D FEM Stokes code developed by Lane (2011). It solves Stokes equation with a Bubnov-Galerkin scheme using P_1P_2 or Taylor-Hood elements; this means that pressure and velocity are approximated linearly and quadratically, respectively. Pressure is defined at the vertices and velocity is defined at vertices and at edges' mid-points – the quadratic approximation for velocity requires more degrees of freedom (Figure 2.4). Constant traction (normal component) boundary conditions are set at inlet and outlet whereas no-slip conditions are imposed at the interior surfaces and on no-flow boundaries.

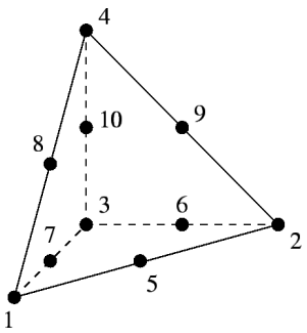

Figure 2.4: P_1P_2 element: pressure is defined at points 1, 2, 3, and 4 (vertices); velocity is defined at all points (from Shen (2014)).

2.3 Nanoparticle Transport Modeling

Column experiments are commonly used to study a wide range of factors that affect NP retention in porous media, including different types of porous media such as sand, crushed sedimentary rocks and core plugs (e.g., Neukum et al., 2014; Yu et al., 2012; Zhang et al., 2014), solution pH and ionic strength (e.g., Chowdhury et al., 2011; Li et al., 2011; Vitorge et al., 2014), flow rate (e.g., Ben-Moshe et al., 2010; Chowdhury et al., 2011; Zhang et al., 2014), NP size and material (e.g., Ben-Moshe et al., 2010; Zhang et al., 2014), NP concentration (e.g., El Badawy et al., 2013; Vitorge et al., 2014; Zhang et al., 2014), addition of organic matter (e.g., Ben-Moshe et al., 2010) or clay (e.g., Zhang et al., 2014). These experiments showed that various factors had an impact on NP retention, with adsorption capacities varying from 10^{-5} to 10^{1} mg/g (Zhang et al., 2014). This variation was dependent on porous medium, NP material, solution chemistry as well as operating conditions like NP concentration and flow rate.

Another approach to study NP retention in porous media is by modifying the classical colloid filtration theory (CFT) equations. CFT was proposed by Yao et al. (1971) and models the particle effluent concentration using a one-dimensional advection-diffusion equation.

They proposed that a particle may be captured by a collector either by interception, sedimentation, or diffusion (Figure 2.5). These processes were incorporated into the governing equation by a collector efficiency parameter. Since then, CFT has been extensively used to model fate and transport of colloids in porous media and also modified to account for different mechanisms of particle retention. Nelson and Ginn (2005) showed that, for submicrometer particles, CFT failed due to the independent treatment of diffusion and advection and concluded that diffusion and advection need to be modeled simultaneously. Modified CFT now accounts for favorable and unfavorable attachment conditions (e.g., Tufenkji and Elimelech, 2005) as well as more constraints for particle retention such as straining (e.g., Bradford et al., 2004) and capacity of attachment sites (e.g., Johnson and Elimelech, 1995).

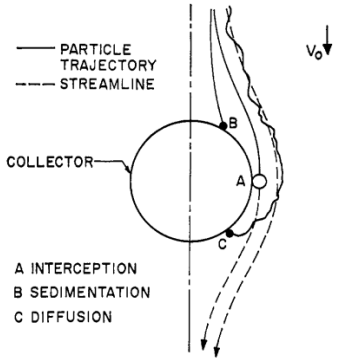

Figure 2.5: Particle retention mechanisms, from Yao et al. (1971).

The collector efficiency used in the CFT models are based on the Happel sphere-in-cell (Figure 2.6, a.), an ideal geometry that disregards collector-collector contacts. In order to account for these, Ma et al. (2009) developed a hemisphere-in-cell geometry (Figure 2.6, b.). Although the latter is a considerable improvement, both geometries are ideal and far from the complex geometries that occurs in many porous medium systems. Moreover, the main

result of modified CFT are breakthrough curves, which do not provide details on the location of retention sites and concentration at particular sites.

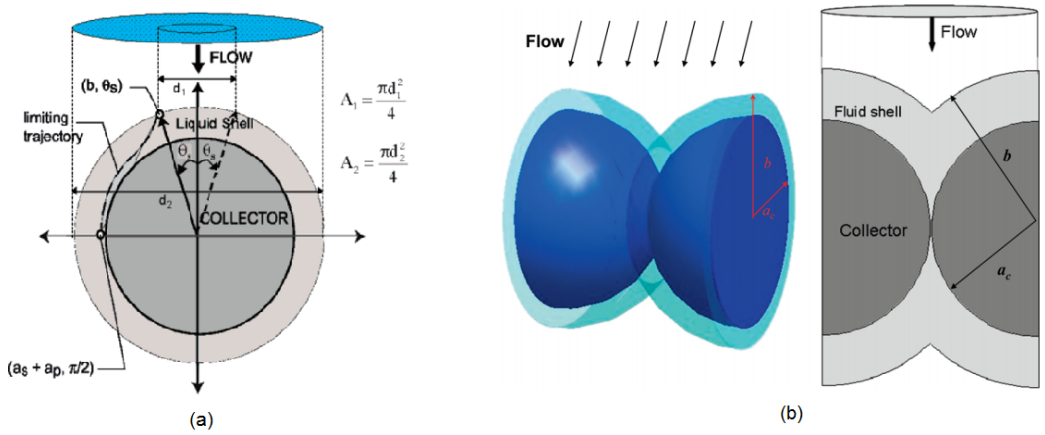

Figure 2.6: Collector geometries: (a) Happel in-cell-sphere, from Nelson and Ginn (2005), and (b) Hemisphere-in-cell, from Ma et al. (2009).

Molnar et al. (2014) used XCT to image silver NP (nAg) concentration in glass bead packs while conducting flow experiments. To the knowledge of the author, this is the first attempt of estimating nanoparticle concentration using XCT; this method determines a 3D distribution of NP concentration, results that column experiments and CFT models fail to provide. In addition, it provides visualization of nAg concentration in the porous medium.

Researchers have also modeled NP transport using computational methods. An Eulerian-Lagrangian approach is often used, where the flow is solved using an Eulerian method (e.g., lattice Boltzmann, FEM, finite different methods) and, subsequently, a Lagrangian particle tracking model is implemented using the velocity field solution. Wang et al. (2005a) implemented this methodology to model aerosol particles in gas in a 2D geometry of aerodynamic lenses. They used two coupled ordinary differential equations (ODEs) to

account for drag and Brownian forces:

$$\frac{d\mathbf{v}_p}{dt} = \mathbf{F}_D + \mathbf{F}_B \tag{2.13}$$

$$\frac{d\mathbf{x}_p}{dt} = \mathbf{v}_p \tag{2.14}$$

where $\mathbf{v}_p$ is the particle velocity, $\mathbf{x}_p$ is the particle position, $\mathbf{F}_D$ is the drag force, and $\mathbf{F}_B$ is the Brownian force. Mehel et al. (2010) used the same approach to model micro- and nano-particle deposition in wall-bounded turbulent flows by adding lift and gravity forces to the right hand side of Equation 2.13. Longest and Xi (2007) modeled deposition of ultrafine aerosols in upper airways, a more complex 3D geometry than previous works. The framework of coupling ODEs 2.13 and 2.14 is based on first principles and provides a robust approach to include extra forces when necessary. For example, Larimi et al. (2014) added a magnetic force term to account for magnetic field around the medium.

It is worthwhile noting that these previous methods were not applied in complex geometries of porous medium, which is a major challenge in the implementation. This is because particle-surface interactions are more common in porous media and these need to be handled carefully in the numerical scheme. Also worth noting, Pham et al. (2014) developed an Eulerian-Lagrangian method for porous media and validated against experimental results. Nevertheless, the geometry consisted of a sphere pack (an ideal porous media) with a few pores and they used one ODE (Equation 2.14) and introduced particle attachment through a probabilistic term.

The NP transport model presented in this work uses the coupled ODEs, Equations 2.13 and 2.14, and adds a surface force term to Equation 2.13. As work progresses, more force terms can be added/removed as necessary. A great benefit of this work's methodology is the use of unstructured mesh and FEM Stokes flow, which allows the simulations in XCT images of very complex geometries across thousands of pores.

2.4 Bibliography

Agulleiro, J. I. and Fernandez, J. J. (2011). Fast tomographic reconstruction on multicore computers. *Bioinformatics*, 27(4):582–583. 10.1093/bioinformatics/btq692. 12

Akanji, L. T. and Matthai, S. K. (2010). Finite element-based characterization of pore-scale geometry and its impact on fluid flow. *Transport in Porous Media*, 81(2):241–259. 10.1007/s11242-009-9400-7. 28

Akhlaghi Amiri, H. and Hamouda, A. (2014). Pore-scale modeling of non-isothermal two phase flow in 2d porous media: Influences of viscosity, capillarity, wettability and heterogeneity. *International Journal of Multiphase Flow*, 61:14–27. 10.1016/j.ijmultiphaseflow.2014.01.001. 28

Alvarez, L. and Mazorra, L. (1994). Signal and image restoration using shock filters and anisotropic diffusion. *SIAM Journal on Numerical Analysis*, 31(2):590–605. 10.1137/0731032. 17

APS (n.d.). The electron storage ring. Advanced Photon Source – Argonne National Laboratory. http://www.aps.anl.gov/About/APS_Overview/storage_ring.html. 9

Avizo (2013). Avizo reference guide. http://www.fei.com/software/avizo-3d-resources/. 18

Balhoff, M. T. and Thompson, K. E. (2006). A macroscopic model for shear-thinning flow in packed beds based on network modeling. *Chemical Engineering Science*, 61(2):698–719. 10.1016/j.ces.2005.04.030. 25

Balhoff, M. T. and Wheeler, M. F. (2009). A Predictive Pore-Scale Model for Non-Darcy Flow in Porous Media. *SPE Journal*, 14(04):579–587. 10.2118/110838-PA. 25

Beister, M., Kolditz, D., and Kalender, W. A. (2012). Iterative reconstruction methods in x-ray CT. *Physica Medica*, 28(2):94–108. 10.1016/j.ejmp.2012.01.003. 11, 12

Ben-Moshe, T., Dror, I., and Berkowitz, B. (2010). Transport of metal oxide nanoparticles in saturated porous media. *Chemosphere*, 81(3):387–393. 10.1016/j.chemosphere.2010.07.007. 29

Bésuelle, P., Viggiani, G., Lenoir, N., Desrues, J., and Bornert, M. (2010). X-ray micro CT for studying strain localization in clay rocks under triaxial compression. In *Advances in X-ray Tomography for Geomaterials*, chapter X-ray Micr, pages 35–52. ISTE, London, UK. 10.1002/9780470612187.ch2. 24

Beucher, S. (2010). The watershed transformation. http://cmm.ensmp.fr/~beucher/wtshed.html. Accessed: 28 October 2014. 22

Bhattad, P., Willson, C. S., and Thompson, K. E. (2013). Segmentation of low-contrast three-phase x-ray computed tomography images of porous media. In *Advances in Computed Tomography for Geomaterials*, pages 254–261. John Wiley & Sons, Inc. 10.1002/9781118557723.ch30. 21

Bingölbali, A. and MacDonald, C. A. (2009). Curved crystal x-ray optics for monochromatic imaging with a clinical source. *Medical Physics*, 36(4):1176–1183. doi: 10.1118/1.3083568. 8

Bird, M., Butler, S., Hawkes, C., and Kotzer, T. (2014). Numerical modeling of fluid and electrical currents through geometries based on synchrotron x-ray tomographic images of reservoir rocks using Avizo and COMSOL. *Computers & Geosciences*, 73:6–16. 10.1016/j.cageo.2014.08.009. 24, 28

Blunt, M. J., Bijeljic, B., Dong, H., Gharbi, O., Iglauer, S., Mostaghimi, P., Paluszny, A., and Pentland, C. (2013). Pore-scale imaging and modelling. *Advances in Water Resources*, 51:197–216. 10.1016/j.advwatres.2012.03.003. 24, 25, 26, 27

Boek, E., Chin, J., and Coveney, P. V. (2003). Lattice boltzmann simulation of the flow of non-newtonian fluids in porous media. *International Journal of Modern Physics B*, 17(1-2):99–102. 10.1142/S021797920301714X. 26

Bradford, S. a., Bettahar, M., Simunek, J., and van Genuchten, M. T. (2004). Straining and Attachment of Colloids in Physically Heterogeneous Porous Media. *Vadose Zone Journal*, 3(2):384. 10.2136/vzj2004.0384. 30

Brooks, R. A. and Chiro, G. D. (1976). Principles of computer assisted tomography ({CAT}) in radiographic and radioisotopic imaging. *Physics in Medicine and Biology*, 21(5):689. 10.1088/0031-9155/21/5/001. 12

Buades, A., Coll, B., and Morel, J. (2005a). A review of image denoising algorithms, with a new one. *Multiscale Modeling & Simulation*, 4(2):490–530. 10.1137/040616024. 13, 15, 17, 18

Buades, A., Coll, B., and Morel, J.-M. (2005b). A non-local algorithm for image denoising. In *Computer Vision and Pattern Recognition, 2005. CVPR 2005. IEEE Computer Society Conference on*, volume 2, pages 60–65. 10.1109/CVPR.2005.38. 18

Buades, A., Coll, B., and Morel, J.-M. (2011). Non-Local Means Denoising. *Image Processing On Line*, 1. 10.5201/ipol.2011.bcm_nlm. 18

Budinger, T. F. and Gullberg, G. T. (1974). Three-dimensional reconstruction of isotope distributions. *Physics in Medicine and Biology*, 19(3):387–389. 10.1088/0031-9155/19/3/012. 12

Catté, F., Lions, P., Morel, J., and Coll, T. (1992). Image selective smoothing and edge detection by nonlinear diffusion. *SIAM Journal on Numerical Analysis*, 29(1):182–193. 10.1137/0729012. 14, 15

Chai, Z., Shi, B., Lu, J., and Guo, Z. (2010). Non-darcy flow in disordered porous media: A lattice Boltzmann study. *Computers & Fluids*, 39(10):2069–2077. 10.1016/j.compfluid.2010.07.012. 26

Chandrupatla, T. R. and Belegundu, A. D. (1991). *Introduction to finite elements in engineering*. Prentice-Hall, Inc. 27

Chareyre, B., Cortis, A., Catalano, E., and Barthélemy, E. (2012). Pore-scale modeling of viscous flow and induced forces in dense sphere packings. *Transport in Porous Media*, 92(2):473–493. 10.1007/s11242-011-9915-6. 28

Chowdhury, I., Hong, Y., Honda, R. J., and Walker, S. L. (2011). Mechanisms of tio2 nanoparticle transport in porous media: role of solution chemistry, nanoparticle concentration, and flowrate. *Journal of colloid and interface science*, 360(2):548–555. 10.1016/j.jcis.2011.04.111. 29

Cnudde, V. and Boone, M. (2013). High-resolution x-ray computed tomography in geosciences: A review of the current technology and applications. *Earth-Science Reviews*, 123(0):1–17. 10.1016/j.earscirev.2013.04.003. 8, 9, 10, 19

Coles, M. E., Muegge, E. L., and Sprunt, E. S. (1991). Applications of CAT scanning for oil and gas production. *Nuclear Science, IEEE Transactions on*, 38(2):510–515. 10.1109/23.289350. 8

Crestana, S., Mascarenhas, S., and Pozzi-Mucelli, R. S. (1985). Static and dynamic three-dimensional studies of water in soil using computed tomographic scanning. *Soil Science*, 140(5):326–332. 7

De Man, B. and Fessler, J. A. (2010). Statistical iterative reconstructionfor x-ray computed tomography. In Censor, Y., Jiang, M., and Wang, G., editors, *Biomedical Mathematics: Promising Directions in Imaging, Therapy Planning, and Inverse Problems*, chapter 7. Medical Physics Publishing Madison (WI). 12

Deans, S. R. (2007). *The Radon transform and some of its applications*. Courier Dover Publications. 11

Defrise, M. and Gullberg, G. T. (2006). Image reconstruction. *Physics in medicine and biology*, 51(13):R139–54. 10.1088/0031-9155/51/13/R09. 11

Dilmanian, F. A., Wu, X. Y., Parsons, E. C., Ren, B., Kress, J., Button, T. M., Chapman, L. D., Coderre, J. A., Giron, F., Greenberg, D., Krus, D. J., Liang, Z., Marcovici, S., Petersen, M. J., Roque, C. T., Shleifer, M., Slatkin, D. N., Thomlinson, W. C., Yamamoto, K., and Zhong, Z. (1997). Single- and dual-energy CT with monochromatic synchrotron x-rays. *Physics in Medicine and Biology*, 42(2):371. 10.1088/0031-9155/42/2/009. 10

Eddins, S. (2002). The watershed transform: Strategies for image segmentation. http://www.mathworks.com/company/newsletters/articles/the-watershed-transform-strategies-for-image-segmentation.html. Accessed: 28 October 2014. 22

El Badawy, A. M., Hassan, A. A., Scheckel, K. G., Suidan, M. T., and Tolaymat, T. M. (2013). Key factors controlling the transport of silver nanoparticles in porous media. *Environmental science & technology*, 47(9):4039–45. 10.1021/es304580r. 29

Elliott, J. C. and Dover, S. (1985). X-ray microscopy using computerized axial tomography. *Journal of Microscopy*, 138(3):329–331. 10.1111/j.1365-2818.1985.tb02627.x. 7

Elliott, J. C. and Dover, S. D. (1982). X-ray microtomography. *Journal of Microscopy*, 126(2):211–213. 10.1111/j.1365-2818.1982.tb00376.x. 7

Esakkirajan, S., Veerakumar, T., Subramanyam, A., and PremChand, C. (2011). Removal of high density salt and pepper noise through modified decision based unsymmetric trimmed median filter. *Signal Processing Letters, IEEE*, 18(5):287–290. 10.1109/LSP.2011.2122333. 14

Fatt, I. (1956). The network model of porous media. *Petroleum Transactions, AIME*, 207:144–181. 25

Feldkamp, L. A., Davis, L. C., and Kress, J. W. (1984). Practical cone-beam algorithm. *Journal of the Optical Society of America A*, 1(6):612–619. 10.1364/JOSAA.1.000612. 11

Fessler, J. (2014). 2.11-fundamentals of CT reconstruction in 2D and 3D. In Brahme, A., editor, *Comprehensive Biomedical Physics*, pages 263–295. Elsevier, Oxford. 10.1016/B978-0-444-53632-7.00212-4. 11, 12

Flannery, B. P., Deckman, H. W., Roberge, W. G., and D'Amico, K. L. (1987). Three-dimensional x-ray microtomography. *Science*, 237(4821):1439–1444. 10.1126/science.237.4821.1439. 8

Fosbinder, R. and Orth, D. (2011). *Essentials of radiologic science*. Lippincott Williams & Wilkins. 10

Fourar, M., Radilla, G., Lenormand, R., and Moyne, C. (2004). On the non-linear behavior of a laminar single-phase flow through two and three-dimensional porous media. *Advances in Water Resources*, 27(6):669–677. 10.1016/j.advwatres.2004.02.021. 28

Ghaddar, C. K. (1995). On the permeability of unidirectional fibrous media: A parallel computational approach. *Physics of Fluids*, 7(11):2563. 10.1063/1.868706. 28

Gray, W. G. and Hassanizadeh, S. M. (1991). Unsaturated flow theory including interfacial phenomena. *Water Resources Research*, 27(8):1855–1863. 6

Grodzins, L. (1983). Critical absorption tomography of small samples: Proposed applications of synchrotron radiation to computerized tomography {II}. *Nuclear Instruments and Methods in Physics Research*, 206(3):547–552. 9

H, H. and Haddad, R. (1995). Adaptive median filters: new algorithms and results. *Image Processing, IEEE Transactions on*, 4(4):499–502. 14

Hannaoui, R., Horgue, P., Larachi, F., Haroun, Y., Augier, F., Quintard, M., and Prat, M. (2015). Pore-network modeling of trickle bed reactors: Pressure drop analysis. *Chemical Engineering Journal*, 262:334–343. 25

Hao, L. and Cheng, P. (2010). Pore-scale simulations on relative permeabilities of porous media by lattice Boltzmann method. *International Journal of Heat and Mass Transfer*, 53(9-10):1908–1913. 24, 26

Hassanizadeh, S. and Gray, W. G. (1990). Mechanics and thermodynamics of multiphase flow in porous media including interphase boundaries. *Advances in Water Resources*, 13(4):169–186. 6

Hassanizadeh, S. M. and Gray, W. (1993). Thermodynamic basis of capillary pressure in porous media. *Water Resources Research*, 29(10):3389–3405. 6

Hazlett, R. D. (1995). Simulation of capillary-dominated displacements in microtomographic images of reservoir rocks. *Transport in Porous Media*, 20(1-2):21–35. 26

Herring, A. L., Andersson, L., Newell, D. L., Carey, J. W., and Wilden (2013). High resolution x-ray CMT imaging of supercritical CO_2 in porous media: Experimental challenges, solutions, and results. In *AGU Fall Meeting*, number H31E-1226. American Geophysical Union. 24

Hounsfield, G. N. (1973). Computerized transverse axial scanning (tomography): Part 1. description of system. *The British Journal of Radiology*, 46(552):1016–1022. PMID: 4757352. 7, 11

Houston, A., Otten, W., Baveye, P., and Hapca, S. (2013). Adaptive-window indicator kriging: A thresholding method for computed tomography images of porous media. *Computers & Geosciences*, 54(0):239 – 248. 19, 21

Huang, T., Yang, G., and Tang, G. (1979). A fast two-dimensional median filtering algorithm. *Acoustics, Speech and Signal Processing, IEEE Transactions on*, 27(1):13–18. 14

Iassonov, P., Gebrenegus, T., and Tuller, M. (2009). Segmentation of x-ray computed tomography images of porous materials: A crucial step for characterization and quantitative analysis of pore structures. *Water Resources Research*, 45(9). 19, 20, 21, 22

ITK (n.d.). The insight toolkit. http://www.itk.org/. 15

Joekar-Niasar, V. and Hassanizadeh, S. M. (2012). Uniqueness of Specific Interfacial Area-Capillary Pressure-Saturation Relationship Under Non-Equilibrium Conditions in Two-Phase Porous Media Flow. *Transport in Porous Media*, 94(2):465–486. 25, 26

Joekar-Niasar, V., van Dijke, M. I. J., and Hassanizadeh, S. M. (2012). Pore-Scale Modeling of Multiphase Flow and Transport: Achievements and Perspectives. *Transport in Porous Media*, 94(2):461–464. 24, 25

Johnson, P. R. and Elimelech, M. (1995). Dynamics of colloid deposition in porous media: Blocking based on random sequential adsorption. *Langmuir*, 11(3):801–812. 10.1021/la00003a023. 30

Kaestner, A., Lehmann, E., and Stampanoni, M. (2008). Imaging and image processing in porous media research. *Advances in Water Resources*, 31(9):1174–1187. Quantitative links between porous media structures and flow behavior across scales. doi: 10.1016/j.advwatres.2008.01.022. 13, 14, 15, 16, 17

Kang, Q., Zhang, D., and Chen, S. (2002). Unified lattice Boltzmann method for flow in multiscale porous media. *Physical Review E*, 66(5):056307. 26

Kass, M., Witkin, A., and Terzopoulos, D. (1988). Snakes: Active contour models. *International Journal of Computer Vision*, 1(4):321–331. 22, 23

Ketcham, R. A. and Carlson, W. D. (2001). Acquisition, optimization and interpretation of x-ray computed tomographic imagery: applications to the geosciences. *Computers and Geosciences*, 27(4):381–400. 3D reconstruction, modelling; visualization of geological materials. 7, 8, 10

Kim, D. and Lindquist, W. B. (2012). Dependence of pore-to-core up-scaled reaction rate on flow rate in porous media. *Transport in Porous Media*, 94(2):555–569. 25

Kittler, J. and Illingworth, J. (1986). Minimum error thresholding. *Pattern Recognition*, 19(1):41–47. 21

Lane, N. M. (2011). *Numerical studies of flow in porous media using an unstructured approach*. PhD thesis, Louisiana State University. 24, 28

Larimi, M., Ramiar, A., and Ranjbar, A. (2014). Numerical simulation of magnetic nanoparticles targeting in a bifurcation vessel. *Journal of Magnetism and Magnetic Materials*, 362:58–71. 10.1016/j.jmmm.2014.03.002. 32

Li, T., Li, X., Wang, J., Wen, J., Lu, H., Hsieh, J., and Liang, Z. (2004). Nonlinear sinogram smoothing for low-dose x-ray CT. *Nuclear Science, IEEE Transactions on*, 51(5):2505–2513. 11

Li, Z., Sahle-Demessie, E., Hassan, A. A., and Sorial, G. a. (2011). Transport and deposition of ceo2 nanoparticles in water-saturated porous media. *Water research*, 45(15):4409–4418. 29

Lie, J. and Nordbotten, J. (2007). Inverse scale spaces for nonlinear regularization. *Journal of Mathematical Imaging and Vision*, 27(1):41–50. 16

Longest, P. W. and Xi, J. (2007). Effectiveness of direct Lagrangian tracking models for simulating nanoparticle deposition in the upper airways. *Aerosol Science and Technology*, 41(4):380–397. 10.1080/02786820701203223. 32

Lopez, X., Valvatne, P. H., and Blunt, M. J. (2003). Predictive network modeling of single-phase non-Newtonian flow in porous media. *Journal of Colloid and Interface Science*, 264(1):256–265. 25

Ma, H., Pedel, J., Fife, P., and Johnson, W. P. (2009). Hemispheres-in-cell geometry to predict colloid deposition in porous media. *Environmental science & technology*, 43(22):8573–8579. 10.1021/es901242b. 30, 31

Manwart, C., Aaltosalmi, U., Koponen, a., Hilfer, R., and Timonen, J. (2002). Lattice-Boltzmann and finite-difference simulations for the permeability for three-dimensional porous media. *Physical Review E*, 66(1):016702. 24

Meakin, P. and Tartakovsky, A. M. (2009). Modeling and simulation of pore-scale multiphase fluid flow and reactive transport in fractured and porous media. *Reviews of Geophysics,*, 47(3):1–47. 26

Mehel, A., Tanière, A., Oesterlé, B., and Fontaine, J.-R. (2010). The influence of an anisotropic Langevin dispersion model on the prediction of micro- and nanoparticle deposition in wall-bounded turbulent flows. *Journal of Aerosol Science*, 41(8):729–744. 10.1016/j.jaerosci.2010.04.011. 32

Mendoza, M., Wittel, F. K., and Herrmann, H. J. (2010). Simulation of flow of mixtures through anisotropic porous media using a lattice Boltzmann model. *The European physical journal. E, Soft matter*, 32(4):339–48. 26

Molnar, I. L., Willson, C. S., O'Carroll, D. M., Rivers, M. L., and Gerhard, J. I. (2014). Method for obtaining silver nanoparticle concentrations within a porous medium via synchrotron x-ray computed microtomography. *Environmental science & technology*, 48(2):1114–22. 31

Mostaghimi, P., Blunt, M. J., and Bijeljic, B. (2012). Computations of Absolute Permeability on Micro-CT Images. *Mathematical Geosciences*, 45(1):103–125. 24

Natterer, F. and Wübbeling, F. (2001). *Mathematical Methods in Image Reconstruction*. Society for Industrial and Applied Mathematics. 10.1137/1.9780898718324. 11

Nelson, K. E. and Ginn, T. R. (2005). Colloid filtration theory and the happel sphere-in-cell model revisited with direct numerical simulation of colloids. *Langmuir*, 21(6):2173–84. 10.1021/la048404i. 30, 31

Neukum, C., Braun, A., and Azzam, R. (2014). Transport of stabilized engineered silver (Ag) nanoparticles through porous sandstones. *Journal of contaminant hydrology*, 158:1–13. 29

Oh, W. and Lindquist, W. (1999). Image thresholding by indicator kriging. *Pattern Analysis and Machine Intelligence, IEEE Transactions on*, 21(7):590–602. 10.1109/34.777370. 21

Onoe, M., Tsao, J. W., Yamada, H., Nakamura, H., Kogure, J., Kawamura, H., and Yoshimatsu, M. (1984). Computed tomography for measuring the annual rings of a live tree. *Nuclear Instruments and Methods in Physics Research*, 221(1):213–220. Proceedings of the International Workshop on X- and Îş-Ray Imaging Techniques. 7

Osher, S. and Rudin, L. (1990). Feature-oriented image enhancement using shock filters. *SIAM Journal on Numerical Analysis*, 27(4):919–940. 16

Otsu, N. (1979). A threshold selection method from gray-level histograms. *IEEE Transactions on Systems, Man, and Cybernetics*, 9(1):62–66. 21

Ovaysi, S. and Piri, M. (2010). Direct pore-level modeling of incompressible fluid flow in porous media. *Journal of Computational Physics*, 229(19):7456–7476. 25

Pal, N. R. and Pal, S. K. (1993). A review on image segmentation techniques. *Pattern Recognition*, 26(9):1277 – 1294. 20

Pan, C., Hilpert, M., and Miller, C. T. (2004). Lattice-Boltzmann simulation of two-phase flow in porous media. *Water Resources Research*, 40(1):14. 24, 26

Pan, X., Sidky, E. Y., and Vannier, M. (2009). Why do commercial CT scanners still employ traditional, filtered back-projection for image reconstruction? *Inverse Problems*, 25(12):123009. 11, 12

Perona, P. and Malik, J. (1990). Scale-space and edge detection using anisotropic diffusion. *Pattern Analysis and Machine Intelligence, IEEE Transactions on*, 12(7):629–639. 14

Petrovic, A., Siebert, J., and Rieke, P. (1982). Soil bulk density analysis in three dimensions by computed tomographic scanning. *Soil Science Society of America Journal*, 46(3):445–450. 7

Pham, N. H., Swatske, D. P., Harwell, J. H., Shiau, B.-J., and Papavassiliou, D. V. (2014). Transport of nanoparticles and kinetics in packed beds: A numerical approach with lattice Boltzmann simulations and particle tracking. *International Journal of Heat and Mass Transfer*, 72:036304. 26, 32

Porter, M. L., Schaap, M. G., and Wildenschild, D. (2009). Lattice-Boltzmann simulations of the capillary pressure-saturation-interfacial area relationship for porous media. *Advances in Water Resources*, 32(11):1632–1640. 24, 26

Porter, M. L. and Wildenschild, D. (2009). Image analysis algorithms for estimating porous media multiphase flow variables from computed microtomography data: a validation study. *Computational Geosciences*, 14(1):15–30. 21

Prodanović, M. and Bryant, S. L. (2006). A level set method for determining critical curvatures for drainage and imbibition. *Journal of colloid and interface science*, 304(2):442–58. 24

Prodanović, M., Lindquist, W., and Seright, R. (2007). 3D image-based characterization of fluid displacement in a Berea core. *Advances in Water Resources*, 30(2):214–226. 21

Radon, J. (1917). On determination of functions by their integral values along certain multiplicities. *Ber. der Sachische Akademie der Wissenschaften Leipzig,(Germany)*, 69:262–277. 7, 11

Raynaud, S., Ngan-Tillard, D., Desrues, J., and Mazerolle, F. (2008). Brittle-to-ductile transition in Beaucaire marl from triaxial tests under the CT-scanner. *International Journal of Rock Mechanics and Mining Sciences*, 45(5):653–671. 10.1016/j.ijrmms.2007.08.007. 24

Roerdink, J. and Meijster, A. (2001). The watershed transform: Definitions, algorithms and parallelization strategies. *Fundamenta Informaticae*, 41:187–228. 22

Röntgen, W. C. (1896). On a new kind of rays. *Science*, 3(59):227–231. 7

Rudin, L. I., Osher, S., and Fatemi, E. (1992). Nonlinear total variation based noise removal algorithms. *Physica D: Nonlinear Phenomena*, 60(1âĂŞ4):259–268. 15

Sato, T., Ikeda, O., Yamakoshi, Y., and Tsubouchi, M. (1981). X-ray tomography for microstructural objects. *Appl. Opt.*, 20(22):3880–3883. 7

Schaap, M. G., Porter, M. L., Christensen, B. S. B., and Wildenschild, D. (2007). Comparison of pressure-saturation characteristics derived from computed tomography and lattice Boltzmann simulations. *Water Resources Research*, 43(12):n/a–n/a. 26

Schlüter, S., Sheppard, A., Brown, K., and Wildenschild, D. (2014). Image processing of multiphase images obtained via x-ray microtomography: A review. *Water Resources Research*, 50(4):3615–3639. 12, 13, 14, 15, 16, 17, 18, 19, 20, 21, 22, 23

Sezgin, M. and Sankur, B. (2004). Survey over image thresholding techniques and quantitative performance evaluation. *Journal of Electronic Imaging*, 13(1):146–168. 20

Shen, Y. (2014). *Image-based pore-scale modeling of inertial flow in porous media and propped fractures*. PhD thesis, Louisiana State University. 24, 25, 29

Sheng, Q. and Thompson, K. (2013). Dynamic coupling of pore-scale and reservoir-scale models for multiphase flow. *Water Resources Research*, 49(9):5973–5988. 25

Sheppard, A. P., Sok, R. M., and Averdunk, H. (2004). Techniques for image enhancement and segmentation of tomographic images of porous materials. *Physica A: Statistical Mechanics and its Applications*, 339(1-2):145–151. 22, 23

Succi, S., Foti, E., and Higuera, F. (1989). Three-dimensional flows in complex geometries with the lattice boltzmann method. *Europhysics Letters*, 10(5):433–438. 26, 27

Takbiri Borujeni, A., Lane, N., Thompson, K., and Tyagi, M. (2013). Effects of image resolution and numerical resolution on computed permeability of consolidated packing using LB and FEM pore-scale simulations. *Computers & Fluids*, 88:753–763. 10.1016/j.compfluid.2013.05.019. 27, 28

Tartakovsky, A. M. and Meakin, P. (2005). A smoothed particle hydrodynamics model for miscible flow in three-dimensional fractures and the two-dimensional RayleighâĂŞTaylor instability. *Journal of Computational Physics*, 207(2):610–624. 25

Taylor, F., Morgan, I., Hopkins, F., Wagner, F. J., and McMillin, C. (1984). Locating knots by industrial tomography–a feasibility study. *Forest products journal*, 34(5):42–46. 7

Thompson, K. E., Willson, C. S., White, C. D., Nyman, S., Bhattacharya, J. P., and Reed, A. H. (2008). Application of a new grain-based reconstruction algorithm to microtomography images for quantitative characterization and flow modeling. *Society of Petroleum Engineers Journal*, 13(2):164–176. 10.2118/95887-PA. 25

Tufenkji, N. and Elimelech, M. (2005). Breakdown of colloid filtration theory: Role of the secondary energy minimum and surface charge heterogeneities. *Langmuir*, 21(3):841–852. 10.1021/la048102g. 30

Tukey, J. W. (1977). Exploratory data analysis. 14

Tuller, M., Kulkarni, R., and Fink, W. (2013). Segmentation of x-ray CT data of porous materials: a review of global and locally adaptive algorithms. In Anderson, S. H. and Hopmans, J. W., editors, *Soil-Water-Root Processes: Advances in Tomography and Imaging*, pages 157–182. The Soil Science Society of America, Inc. 10.2136/sssaspecpub61.c8. 19

Vaz, C., Crestana, S., Mascarenhas, S., Cruvinel, P., Reichardt, K., and Stolf, R. (1989). Using a computed tomography miniscanner for studying tillage induced soil compaction. *Soil Technology*, 2(3):313–321. 7

Vinegar, H. J. and Wellington, S. L. (1987). Tomographic imaging of threeâĂŘphase flow experiments. *Review of Scientific Instruments*, 58(1). 7

Vitorge, E., Szenknect, S., Martins, J. M.-F., Barthès, V., and Gaudet, J.-P. (2014). Comparison of three labeled silica nanoparticles used as tracers in transport experiments in porous media. part ii: transport experiments and modeling. *Environmental pollution (Barking, Essex : 1987)*, 184:613–619. 29

Wang, X., Gidwani, A., Girshick, S. L., and McMurry, P. H. (2005a). Aerodynamic focusing of nanoparticles: II. numerical simulation of particle motion through aerodynamic lenses. *Aerosol Science and Technology*, 39(7):624–636. 10.1080/02786820500181950. 31

Wang, Y., Lesher, C., Fiquet, G., Rivers, M. L., Nishiyama, N., Siebert, J., Roberts, J., Morard, G., Gaudio, S., Clark, A., Watson, H., Menguy, N., and Guyot, F. (2011). In situ high-pressure and high-temperature x-ray microtomographic imaging during large deformation: A new technique for studying mechanical behavior of multiphase composites. *Geosphere*, 7(1):40–53. 24

Wang, Y., Uchida, T., Westferro, F., Rivers, M. L., Nishiyama, N., Gebhardt, J., Lesher, C. E., and Sutton, S. R. (2005b). High-pressure x-ray tomography microscope: Synchrotron computed microtomography at high pressure and temperature. *Review of Scientific Instruments*, 76(7):0737091–0737097. 10.1063/1.1979477. 23

Weisstein, E. W. (n.d.). Circle packing. http://mathworld.wolfram.com/CirclePacking.html. 9

Wildenschild, D. and Sheppard, A. P. (2013). X-ray imaging and analysis techniques for quantifying pore-scale structure and processes in subsurface porous medium systems. *Advances in Water Resources*, 51(0):217–246. 35th Year Anniversary Issue. 7, 8, 9, 10, 13, 19, 20, 22, 25, 27

Yao, K.-M., Habibian, M. T., and O'Melia, C. R. (1971). Water and waste water filtration: Concepts and applications. *Environmental science & technology*, 5(11):1105–1112. 29, 30

Yu, J., An, C., Mo, D., Liu, N., and Lee, R. L. (2012). Study of adsorption and transportation behavior of nanoparticles in three different porous media. *SPE Improved Oil Recovery Symposium*, pages 1–13. 29

Zhang, T., Murphy, M. J., Yu, H., Bagaria, H. G., Yoon, K. Y., Neilson, B. M., Bielawski, C. W., Johnston, K. P., Huh, C., and Bryant, S. L. (2014). Investigation of nanoparticle adsorption during transport in porous media. *SPE Journal*, preprint(preprint):1–11. 29

Zhong, J., Ning, R., and Conover, D. (2004). Image denoising based on multiscale singularity detection for cone beam CT breast imaging. *Medical Imaging, IEEE Transactions on*, 23(6):696–703. 13

Zhong, Z., Dilmanian, F. A., Bacarian, T., Zhong, N., Chapman, D., Ren, B., Wu, X. Y., and Weinmann, H.-J. (2001). Producing parallel x-rays with a bent-crystal monochromator and an x-ray tube. *Medical Physics*, 28(9). 8

3. Image-Based Stokes Flow Modeling in Bulk Proppant Packs and Propped Fractures Under High Loading Stresses

3.1 Abstract

Rock fracturing, followed by proppant injection, has been used for years to improve oil and gas production rates in low permeability reservoirs and is now a routine part of producing from low-permeability resources such as a shales and tight sands. While field data makes clear the effectiveness of this technique, there is still much room to improve on the science, including how the proppant-filled fracture system responds to changes in loading stress and the corresponding impact on the proppant structure and fracture width, which affect permeability and conductivity. Here, we use high-resolution x-ray computed tomography (XCT) to image two unsaturated rock/fracture/proppant systems: one with shale, one with Berea sandstone. Both systems were imaged under a series of stress levels typical of producing reservoirs. The resulting XCT images were segmented, analyzed for structural and porosity changes, and then used for image-based flow modeling of Stokes flow using both finite element (FEM) and Lattice Boltzmann (LBM) methods. The images and quantitative grain analysis showed expected changes as stress increased: rearrangement of the packing structure, corresponding reduction in porosity, and some embedding at rock walls to a depth of less than 0.5 times the proppant diameter. The shale system exhibited more embedding than the Berea system. At the highest stress in the Berea system (20 kpsi or 138 MPa), individual proppant particles failed and the broken particles caused significant loss of permeability. For the shale system, the embedding had a significant effect on the simulated permeability/fracture conductivity. Simulation results for each of the loadings showed that permeability is less sensitive to loading than experimental (vendor-reported)

permeability values, but also show reasonable agreement at 8 kpsi (55 MPa) for both systems. Another somewhat surprising result is that fracture permeability for the single-layer proppants confined between shale is similar to what would be predicted from bulk proppant results, despite the significantly different flow geometry in the monolayer fracture.

3.2 Highlights

- Bulk and monolayer proppant systems have similar permeability trends under loading
- Permeability loss due to bulk proppant failure under loading is quantified
- Loss of fracture conductivity due to proppant embedment is quantified
- Pore-scale velocity distributions become more uniform as loading stress increased

3.3 Keywords

Propped fracture conductivity, bulk proppant permeability, loading stress, Darcy flow, finite element method, Lattice Boltzmann method.

3.4 Introduction

Hydraulic fracturing with proppants has been used for many years to enhance extraction of oil and gas (Cooke, 1973; Graham and Kiel, 1968). In the past decade, advances in hydraulic fracturing and horizontal well techniques have enabled dramatic expansion of commercial shale gas production in North America (Hart et al., 2011; Sondergeld et al., 2010). This new source of natural gas will play an important role in energy resources worldwide due to reduced greenhouse gas emissions and its availability in the United States, as well as in China, Canada, Poland, etc. (Hart et al., 2011). Hydraulic fracturing and horizontal well techniques have also revived gas and oil recovery from existing vertical wells that were

becoming commercially non-viable (Castro et al., 2013; Gutiérrez et al., 2014; Ramurthy et al., 2013; Wornstaff et al., 2014).

Hydraulic fracturing is the process of injecting fluids at high pressure to fracture the producing rock and create high-conductivity flow paths from the source rock or reservoir to the well (Cipolla, 2009). Proppants are added to the fracturing fluid to prop the fracture open after the fracturing pressure is reduced. For the proppants to be effective, it is essential that they maintain paths of high conductivity (Brannon et al., 2006; Kaufman et al., 2008; Warpinski et al., 2008).

Despite its widespread use, many aspects of the hydraulic fracturing process remain poorly understood. For example, a field study showed that of more than 100 Barnett shale gas wells, almost half did not produce, and most of the production came from a small number of wells (Maxwell, 2011). Among many factors that can affect the productivity of a well, formation permeability and fracture conductivity are certainly two of the dominant factors. The network of fractures dominates early flow, whereas matrix permeability becomes important on the gas decline and ultimate recovery (King, 2010; Luffel et al., 1993; Warpinski et al., 2008).

While the permeability of bulk proppant can be considered an intrinsic property (a function of grain/pore size distribution, shape of the grains, tortuosity, specific surface, porosity), fracture conductivity, which combines proppant permeability with fracture width, depends on proppant interactions with the fracture walls. Thus, it is important to be able to evaluate bulk proppant permeability as well as relate this measurement to fracture conductivity. Different proppants can have different permeabilities due to factors such as material, size, roundness, sphericity, etc. Mechanical properties of a material also affect

conductivity due to compression or failure during loading. Other stress-related factors expected to impact fracture conductivity include rearrangement of the proppant packing structure and embedment into the fracture walls.

Work from as early as 1973, found a two-order-of-magnitude reduction in proppant conductivity when the loading stress was increased from 1000 to 10000 psi (6.895 to 68.95 MPa) (Cooke, 1973). A conductivity cell was developed to measure permeability of bulk proppants for different combinations of stress, temperature, fluids (oil, brine, and gas) and a variety of sizes and types of proppants. A load was applied to the piston of the stainless steel cell that contained the proppants, and permeability was determined by flow experiments. The author measured a reduction in permeability up to two orders of magnitude for sand proppants as the pressure was increased from 1000 to 10000 psi (6.895 to 68.95 MPa) at 150 °F (65.6 °C). Much and Penny (1987) used a similar setup to test the conductivity of sand and intermediate strength ceramic proppants (ISP) but used both steel pistons and sandstone cores as column walls. They found that as the loading stress increased, there was a large decrease ($> 50\%$) in Jordan sand conductivity, whereas ceramic proppants decreased $\sim$30%. In addition, ceramic proppants presented at least 50% higher conductivity than Jordan sand. Much and Penny (1987) attributed the differences to the observation that sand crushes at lower loading stresses than ceramic proppants. They concluded that "ceramic ISP proppants can provide conductivities over 1000% greater than sand proppants at equal concentrations and conditions." Fredd et al. (2001) observed similar behavior in a conductivity cell when they tested Jordan sand and bauxite proppants between two sandstones cores from the Texas Cotton Valley formation. Jordan sand started to crush after a loading stress of 2000

psi (13.79 MPa) whereas sintered bauxite did not crush below 5000 psi (34.47 MPa). Pre-experiment sieve analysis revealed that both proppants had less than 5% of the particles smaller than 300 μm. Post-experiment sieve analysis, however, showed that 65% of the Jordan sand particles were lower than 300 μm while bauxite had only 35%. The bauxite conductivity decreased from 2000 mD·ft to 10 mD·ft (6.48×10^{-6} m^2·m to 3.24×10^{-8} m^2·m) and Jordan sand from 400 mD·ft to 0.35 mD·ft (1.30×10^{-6} m^2·m to 1.13×10^{-9} m^2·m), when the stress increased from 1000 to 7000 psi (6.895 to 48.26 MPa). Dusterhoft et al. (2004) used a conductivity cell in which the proppant pack was sandwiched between two Ohio sandstones. They tested bauxite, ISP, and economical lightweight proppants (ELW). All of the proppant systems exhibited a trend of decreasing conductivity as the loading stress increased from 2000 to 12000 psi (13.79 to 82.74 MPa) (bauxite: 7050 to 2016 mD·ft or 2.283×10^{-5} to 6.528×10^{-6} m^2·m; ISP: 7874 to 946 mD·ft or 2.250×10^{-5} to 3.063×10^{-6} m^2·m; ELW: 6779 to 393 mD·ft or 2.195×10^{-5} to 1.273×10^{-6} m^2·m). However, each type of proppant had a different range in which the proppants crushed (bauxite: 8000-10000 psi (55.16-68.95 MPa); ISP: 6000-8000 psi (41.37-55.16 MPa); ELW: 4000-6000 psi (27.58-41.37 MPa)), showing that the material strength is an important factor affecting conductivity. This behavior was especially evident for coated proppants (coating was added to increase conductivity) because they had higher initial porosity but also exhibited crushing at higher stresses because of higher point-load stresses. The uncoated proppants, on the other hand, crushed less, which the authors attribute to the lower porosity. They also observed intrusion of formation fines due to significant failure at the interface. Ye et al. (2012) developed a dynamic compression device and investigated permeability changes for 20-40 high-strength ceramic proppant. Similar to other results, they measured a decrease in permeability from

680 D at 120 psi (6.71×10-10 m^2 at 827 kPa) to 420 D at 7100 psi (4.15×10-10 m^2 at 48.95 MPa), showing the high-strength ceramic proppants are not as susceptible to crushing as other materials. It is clear that the proppant material is an important factor in conductivity and that its failure point needs to be taken into account when comparing conductivity reductions.

Another important factor highlighted by these experiments is the type of column wall used for the flow experiments. Steel pistons are commonly used (Cooke, 1973; Ye et al., 2012). However, this arrangement has a number of distinct differences from a real system, including the inability of the proppant to embed into the wall and the smoothness of the container wall (which influences local packing structure). Experiments reported by Much and Penny (1987) showed different conductivities for steel pistons and sandstone cores. At lower loading stresses (< 2000 psi or 13.79 MP), when there is neither crushing nor embedding, conductivities are higher with steel pistons (except for Jordan sand at 225 °F or 107 °C), which the authors attribute to wall effects introduced by the pistons. In addition, they found that embedding becomes an important factor for loading stresses of 8000 psi (55.16 MPa) or higher for sandstone cores, a situation that is clearly not seen for steel pistons.

X-ray computed tomography (XCT), a technique that allows for the nondestructive imaging of the internal features of the system, is a valuable tool to visualize grains and pore space in 3D. Cheremisin et al. (2011) modified the standard conductivity cell to accommodate a large-scale XCT scanner and compared the performance of rod-shaped proppants with average diameter equal to 12-18 sieve of spherical proppants against 12-18 sieve ISP at different loading stresses. Experimental results showed a decrease in conductivity for both proppants from 2000 to 6000 psi (13.79 to 41.37 MPa): 7250 to 3250 mD·ft (2.348×10^{-5} to

1.052×10^{-5} m^2·m) for rod shaped and 2750 to 2000 mD·ft (8.904×10^{-6} to 6.476×10^{-6} m^2·m) for spherical. X-ray images at 100-μm voxel resolution were obtained for both proppants at 4000 psi (27.58 MPa). Cheremisin et al. (2011) then used pore network modeling to show differences between the pore structures of the two types of proppants and to simulate flow in the porous media. Finite element method was also used to simulate and visualize flow in the porous media. However, permeability or conductivity values were not reported.

Few groups have studied the effect of axial/vertical stress in conjunction with XCT. Raynaud et al. (2008) used XCT, scanning electronic microscopy (SEM), quantitative image analysis of thin sections, and mercury porosimetry to analyze Plaisancian marl and classify the different strain regimes (brittle-ductile transition, axial stress up to 1MPa or154 psi). Bésuelle et al. (2010) obtained XCT images (14 μm resolution) of a Callovo-Oxfordian argillite sample under axial load up to 10 MPa (1450 psi) to define localized deformation classifications from brittle (at 1 MPa) to ductile (at 10 MPa).

Petunin et al. (2011) studied the relationship between stress and permeability using a CMS-300 permeameter. Four types of rock were used and exposed to loadings from 5-35 MPa (725-5000 psi). One carbonate sample (1.5 mm in diameter, 3.0 mm in length) was imaged using XCT at 2.8-μm voxel resolution in order to check experimental results. However, XCT was only used for initial validation (no loading) and XCT images after loading were not obtained.

Compared to experimental studies, relatively few numerical studies of proppant/fracture systems have been reported. Zhao et al. (2008) developed a two-fluid model to simulate the particle migration process in the fracture with various proppant concentrations and flow velocities. Koyama et al. (2008) performed fluid and particle flow simulations in the

2D geometry of a single rock fracture using measured topographical data of the fracture surface obtained from laser scanning profilometer. In the work of Khanna et al. (2012), a fracture filled with a monolayer of proppant particles was modeled as an array of rigid spheres squeezed between two semi-infinite elastic bodies to evaluate the opening length of the fracture according to Hertz contact theory. Computational fluid dynamics (CFD) simulations were used to obtain conductivity at different loading stresses.

In this work, our approach is to use image-based pore-scale modeling, an increasingly popular method to predict flow and transport properties in porous media. The approach can help provide a fundamental understanding of transport in porous media and the topologic and geometric factors that affect it. Two main approaches for image-based pore-scale modeling have evolved since the use of XCT became widespread. One is network modeling, which discretizes the pore space into pores and throats and imposes mass conservation in this system (Bhattad et al., 2011; Lindquist et al., 1996; Oren and Bakke, 2003; Thompson et al., 2008). The second approach uses direct approximation of the equations of motion applied to the digitized image of the pore space. The Lattice Boltzmann method (LBM) is the most widely used of the latter approaches (Auzerais et al., 1996; Bosl et al., 1998; Jin et al., 2004; Schure et al., 2004). The alternatives to LBM are one of the more traditional computational fluid dynamics modeling methods such as finite element method (FEM) or finite volume method (FVM). Both structured grids (Arns et al., 2002; Zhan et al., 2010) and unstructured meshes (Lane, 2011) have been used with CFD techniques for pore-scale modeling.

In this paper we report on nondestructive imaging of dry fracture/proppant systems under different loading stresses, followed by direct numerical simulation of flow in the

digitized pore space to determine proppant permeability and fracture conductivity. Two rock/fracture/proppant systems were imaged using a high-pressure synchrotron-based XCT apparatus. The first system consisted of a bulk packing of 20-40 CarboHSP® high-strength sintered bauxite proppants placed between two Berea sandstone cores; the second was a monolayer of 30-60 CarboHSP® high-strength sintered bauxite proppants loaded between two shale cores. Both systems were imaged approximately at loads of 0, 4, 8, 12 kpsi (0, 28, 55, 83 MPa) and the Berea system was also imaged at 20 kpsi (138 MPa). The image datasets were segmented (void/solid) and packing parameters and pore structure were quantified. Two different image-based simulation techniques were used to compute permeability: finite element method approximation of the Stokes equation using unstructured meshes and the Lattice Boltzmann method operating directly on the voxel grid. For the proppant monolayer between shales, fracture conductivity was also calculated based on the average fracture width as determined from the images. From these results, we are able to better interpret the causes of permeability loss due to mechanical loading than has been possible from past experiments.

3.5 Materials and Methods

3.5.1 Experimental Setup

Two different rocks were used for this study: Berea sandstone and Pierre shale. Two Berea sandstone cores, 6.1 mm in diameter and 2 mm in height, were extracted from a 1 in (2.54 cm) core using a diamond-tipped hollow drill bit. The same approach was used for the Pierre shale, except that we were unable to extract single 6mm-long cores; hence, four cores were cut and stacked in pairs. The proppants, from CARBO Ceramics, were CarboHSP® high-strength sintered bauxite proppants. The proppants used in the Berea test were 20-40

(sieve) with a median particle diameter of 697 μm, and the proppants in the shale test were 30-60 (sieve) with a mean particle diameter of 430 μm.

The sample holder consists of an outer cylindrical plastic sleeve that is transparent to x-rays and strong enough to support the stresses with little deformation ($< 2\%$ for the Berea system and $< 1\%$ for the Shale system) (Figure 3.1). For the Berea system (Figure 3.1, a.), only one sleeve (inner diameter: 6 mm, outer diameter: 10 mm) was used. Steel anvils, used to apply the load to the rock-proppant-rock sample, were 6 mm in diameter and 2 mm in height. For the shale system (Figure 3.1, b.), two sleeves were used (inner diameters: 6, 10 mm; outer diameter: 10, 20 mm, respectively) to allow more stability for the stepped anvils. The rocks and proppants were packed by first placing a layer of rock on the lower anvil, then placing proppants while using a microscope to ensure they remained in a monolayer, and finally inserting another layer of rock on top.

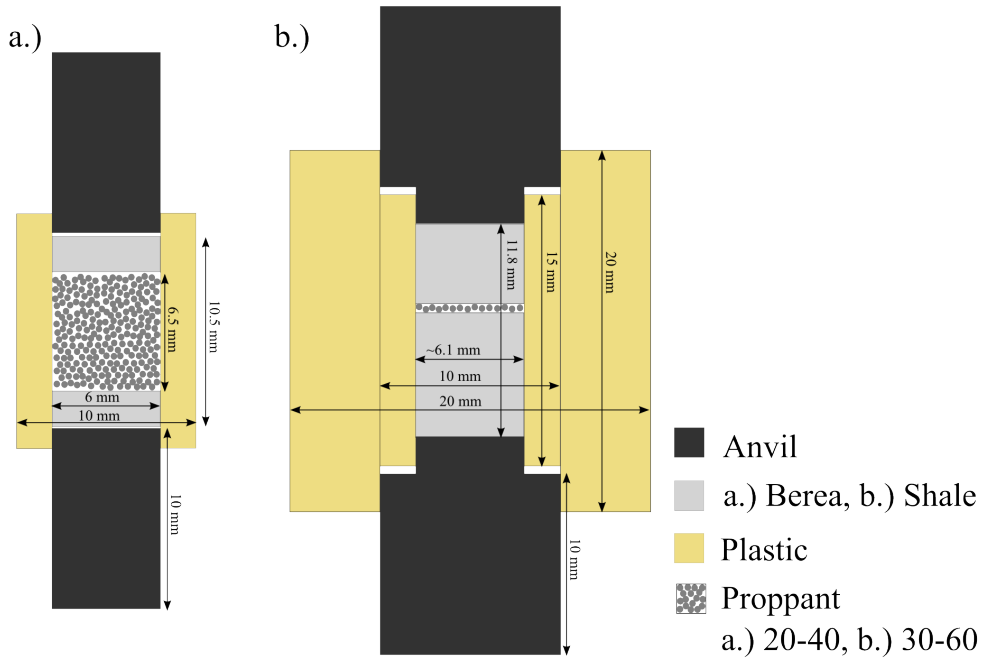

Figure 3.1: Schematic of experimental setup for a.) Berea and b.) Shale.

3.5.2 Data Acquisition

Once assembled, the samples were placed in the Advanced Photon Source GSECARS high pressure tomography module (Wang et al., 2005) in the 13-BMD hutch. The imaging at all loadings was performed using a total of 720 projection images as the specimen was rotated from 0° to 180° by 0.25° increments exposed to monochromatic x-ray beam at 37.00 and 35.00 keV (Berea and shale, respectively) while the incident x-ray flux was stabilized to within a few percent by monitoring the incident beam intensity using an ion chamber. The Berea sample was imaged in two overlapping volumes covering most of the Berea cores and all of the proppants. The entire shale sample (top steel anvil down through bottom steel anvil) was imaged in 3 overlapping regions. Imaging details are summarized in Table 3.1. After the entire sample was imaged at zero stress, a load was applied, and once stabilized at

Table 3.1: Imaging details.

Imaging Details	Berea	Shale
Voxel Dimensions (μm)	11.8	12.0
Energy (keV)	37.00	35.00
Exposure (s)	0.3	0.2
Rotations	720	720
Subvolumes scanned per load	2	3

the desired stress level, the sample was imaged again using the same procedure. The Berea system was imaged at 0, 0.09, 0.18, 0.27, 0.45 tons (1 ton = 2000 lbs), corresponding to loading stresses 0, 4.0, 7.9, 11.9, and 19.9 kpsi (0, 28, 54, 82, and 138 MPa) respectively. The shale was imaged at 0, 0.09, 0.18, and 0.26 tons, corresponding to loading stresses 0, 4.1, 8.2, and 11.9 kpsi (0, 28, 57, and 82 MPa). The loading stresses were calculated by

dividing the load applied at each step by the corresponding sample (Berea or shale) cross-sectional area. Henceforth, the loading stresses are denominated 0, 2, 4, 8, 12, and 20 kpsi for simplicity.

3.5.3 Image Processing

Image reconstruction, the process of converting 2D projection images into a 3D volumetric file, was performed using a filtered back-projection algorithm developed by GSECARS (Rivers, http://cars9.uchicago.edu/software/idl/tomography.html). Each voxel in the 3D volumetric data file (695×695×520 voxels) contains a linear attenuation value that depends on the composition of the phases within the voxel and the x-ray energy. The voxel sizes of the reconstructed images were 11.8 μm for the Berea system and 12.0 μm for the shale system.

The resulting 3D datasets were first converted to 8 bit data and then smoothed by an anisotropic diffusion (AD) filter Bhattad (2010). They were segmented using an indicator kriging (IK) algorithm based on the technique first developed by Oh and Lindquist (1999) and then modified as described in Bhattad et al. (2010). Each segmentation trial was evaluated both quantitatively (e.g., porosity) and qualitatively (i.e., comparison of segmented image to the original grayscale) to select the final segmented image to be used for further analysis. Finally, "islands-and-holes" removal was performed to remove physical voids from the proppant particles (for computational reasons) and to clean up additional speckled noise. The image-processing steps are illustrated for the Berea system at 0-kpsi loading in Figure 3.2.

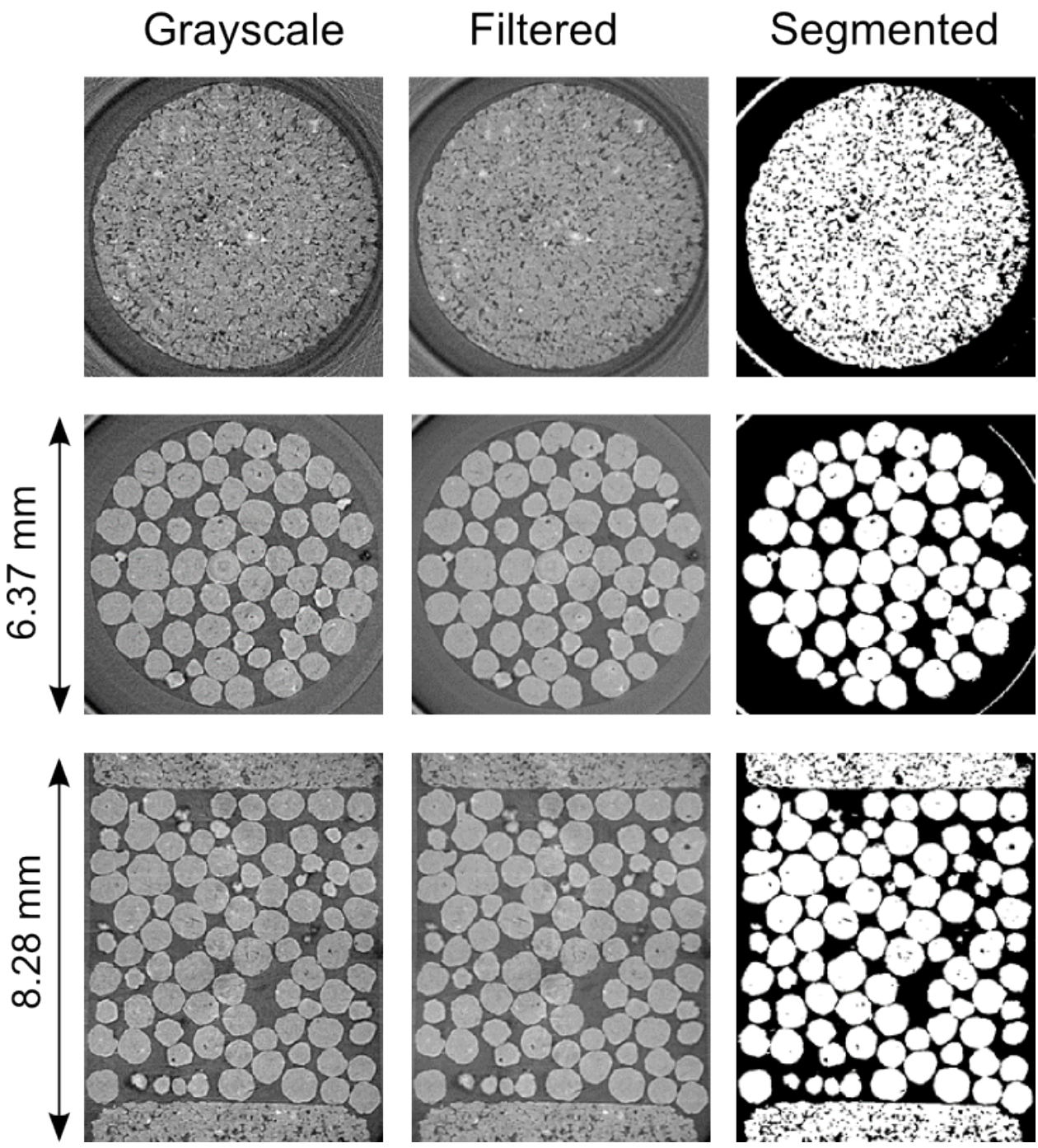

Figure 3.2: Image processing steps for the Berea-proppant system. Top to bottom: xy slice in the Berea; xy slice in the proppant-filled region; and xz slice showing the proppant-filled region with Berea above and below. Left to right: original 16-bit grayscale; after anisotropic diffusion; and after solid/void segmentation.

3.5.4 Image Analysis

3.5.4.1 Porosity and Surface Area

For a given volume of interest, porosity is the ratio of void voxels to total voxels and specific surface area is the ratio of solid surface area to total volume. The solid surface area is calculated using the algorithm described by (Thompson, 2007). For the Berea-proppant sample, two porosities are defined for the proppants. *Bulk porosity* is computed from a cubic cutout from the interior of the packing, 3.54 mm (300 voxels) on a side. *Total porosity* is the porosity of the cylindrical sample, 6 mm in diameter and 3.54 mm in height, excluding the Berea cores; hence it includes wall effects caused by the cylindrical container. See Figure 3.3 for a 3D representation of both cutouts.

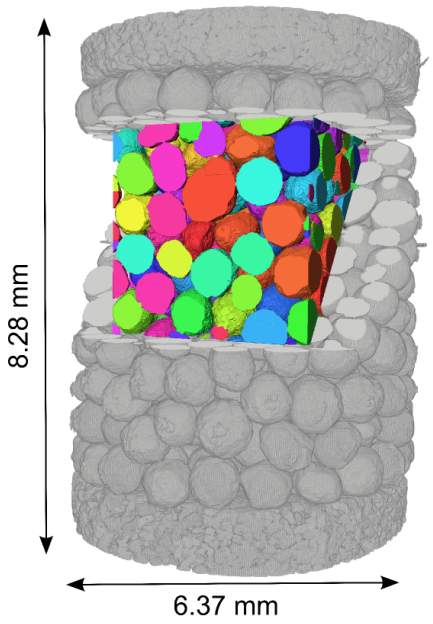

Figure 3.3: Berea-proppant system: 300^3 voxels cubic cutout (colored) used for permeability computation, bulk porosity, and bulk permeability. (For interpretation of the references to color in this figure legend, the reader is referred to the web version of this article.)

For the shale-proppant sample, a 4.80×3.60 mm (400×300 voxels) rectangle inscribed by the cylinder was selected in the *xy*-cross section. A vertical section 0.84 mm (70 voxels) high was extracted, which included portions of the top and bottom shale. Figure 3.13 shows the shale-proppant computational domain. The porosity of this selected single fracture was calculated and defined as the *fracture porosity*. It is important to note that porosity value for the shale sample is an arbitrary number because it depends on the cutout selected and the volume of shale that is included in the cutout. However, a true fracture porosity was difficult to obtain accurately because of the non-uniform geometry of the shale face relative to the Cartesian image grid, and this approach provides a consistent and quantitative way to present porosity differences from one load to another.

3.5.4.2 Embedding

The amount of proppant embedding was estimated by visual inspection followed by direct measurement of embedded length using the gray-scale images. More embedding was observed near the container walls because the rock cores are not cut at a perfect 90° angle, which creates some weakness and/or space for the proppants to move into as stress is applied. Therefore, when measuring embedment in the Berea sample, a 300×300 *xy*-centered cutout with axial length remaining from top to bottom of the Berea was used. For the shale sample, the entire *xy*-cross section was observed, but proppants on the boundary were not included in this estimation.

3.5.5 Grain Analysis

Grain analysis of the 300^3-voxel bulk proppant pack was performed using the methods described in Thompson et al. (2006). This algorithm finds the maximal inscribed sphere for each grain by using a combination of erosion and nonlinear optimization. The grain centers

are located and adjacent voxels belonging to that grain are collected by using a type of watershed algorithm. With this method, each grain is identified and labeled, which allows characterization of the grains to be performed by computing grain surface area, number of grain-to-grain contacts, contact areas, grain volume, grain position, grain orientation, and grain aspect ratio. The grain effective diameter was calculated as the average of the major and minor diameters; in other words, the average of the inscribed diameter and the particle length (Thompson et al., 2006; Willson et al., 2012). Only grains that were fully contained in the cutout were included in the analysis to ensure that the grain-characterization parameters are representative.

3.5.6 Simulation

3.5.6.1 Numerical Techniques: Finite Element Method

The finite element method was used to simulate fluid flow in the pore space. Unstructured meshes of the void space were created by importing segmented XCT images into the commercial software package AVIZO. While FEM simulations can be performed directly on the uniform grid structures from XCT images by using voxels as elements, unstructured meshes allow the mesh resolution to be decoupled from the number of voxels in the image dataset and also allow local mesh refinement to be performed. Therefore, mesh resolution can be tailored to the numerical problems independently of the original image resolution, while still preserving the image structure. In this work, approximately 0.15 elements per voxel were generated for the bulk proppant packing at each loading stress. This value was determined based on numerical convergence as the mesh was continually refined. Figure 3.14 shows the bulk proppant mesh refinement used at 0 psi for a smaller section of the domain ($\sim$1.2 mm or 100 voxels).

An in-house FEM algorithm (Lane, 2011) was used to determine permeability. In this algorithm, the Stokes equation is solved using P2P1 or Taylor-Hood tetrahedral elements (which employ quadratic approximations for velocity and linear shape functions for pressure). The boundary conditions at the inlet and outlet surfaces of the domain were assigned normal tractions equal to the desired applied pressure. No-slip boundary conditions were applied at the interior solid-void interfaces as well as the four sides of the simulation domain (not inlet or outlet). More details can be found in Lane (2011).

3.5.6.2 Numerical Techniques: Lattice Boltzmann Method

The Lattice Boltzmann method is a simplification of the Boltzmann equation that solves for particle distribution functions in a discrete phase space. For more details on the LBM equation and solution method, refer to Supplementary Information, Section 3.9.3.

LBM simulations in this study are done using the Parallel Lattice Boltzmann Solver (PALABOS, 2012) on Louisiana Optical Network Initiative (LONI) resources. The bounce-back boundary scheme is one of the no-flow boundary conditions commonly implemented in LBM simulations. The no-flow boundary is assumed to be at a halfway distance between the fluid and solid nodes for simple geometries. For more complex geometries this scheme puts the no-flow boundary somewhere between the fluid and solid nodes. The exact position of the no-flow boundary varies with the relaxation time used and the geometry (numerical resolution) of the numerical domain. The body force approach is used to replicate a pressure gradient at the inlet and outlet. More details can be found in Takbiri Borujeni (2013); Takbiri Borujeni et al. (2013); Chukwudozie (2011).

Ideally, the porous media domain used for simulations should be periodic representative elementary volumes (REVs) or unit cells. The domains used here for the LBM simulations were changed to periodic by adding ten layers of void voxels to each side. A body force approach, which is an alternative to specifying pressure values at the inlet and outlet of the domain, was used. Periodic boundary conditions were applied on all the external faces. A body force was not applied on these added layers.

Applying high-pressure gradients (large body forces) in LBM simulations may cause continuity errors that can grow at each time-step and break down the simulation. In order to increase numerical resolution and avoid errors, the original domain (300^3 voxels) was sub-divided on each side of the voxels by 2, i.e., increasing the total number of the voxels by a factor of 8.

3.5.6.3 Permeability Computations (Total, Bulk and Monolayer)

Permeability is a continuum-scale porous-media property that quantifies how easily a fluid can flow through the pore space. Permeability is generally related to porosity, tortuosity and the characteristic length in the pore space (the latter is often defined as hydraulic radius in unconsolidated packings). It is defined by Darcy's law, which describes the linear relationship between superficial (Darcy) velocity and pressure gradient:

$$\nu = \frac{k}{\mu} \nabla P \tag{3.1}$$

where k is the permeability and μ is the dynamic viscosity of the fluid. To determine permeability from the FEM or LBM flow simulations, we calculated the inlet/outlet flow

rate $Q = \iint \mathbf{v} \cdot \mathbf{dA}$ and then computed the superficial velocity Q/A based on the known inlet area.

Compared to permeability, conductivity is more widely used to describe transport in fractures. The conductivity of a fracture is calculated as

$$C = kw \tag{3.2}$$

where k is the permeability of the fracture and W is the opening width of the fracture.

We denote the permeability obtained from the 300^3-voxel interior section of the proppant pack as the *bulk permeability* and the permeability obtained from multilayer proppants confined by cylindrical walls as the *total permeability*. For the shale fracture sample, both permeability and conductivity were calculated and defined as the *fracture permeability* and *conductivity respectively*. The cross sectional area of the fracture is the xz-plane perpendicular to the flow direction (y). The opening width is not uniform along the cross-sectional area. Therefore it was approximated as the average opening width and was estimated by visual inspection of the segmented image at each loading stress. The width was measured manually three times at each cross section for 40 different xz-cross sections. The average of these 120 measurements was used as the fracture width for a given loading stress in both cross-sectional area and conductivity calculations.

3.5.6.4 Tortuosity

Tortuosity value quantifies the flow pattern of the fluid in the pore space of proppant packing. It can be defined as the ratio of the length of actual path of fluid to the shortest path length in the direction of the mean flow. Koponen et al. (1996) proposed that the

tortuosity can be calculated based on velocity values on grid points:

$$\tau = \frac{\sum_{i,j,k} u_{\mathrm{mag}(i,j,k)}}{\sum_{i,j,k} |u_z(i,j,k)|} \tag{3.3}$$

where u_{mag} is the magnitude of velocity, u_z is the z direction (flow direction) velocity and (i, j, k) is the location of lattice used to perform the computation.

3.6 Results and Discussion

XCT images of both the Berea and shale systems were analyzed to quantify the effects of loading stress on the proppant structure. For the Berea system, a detailed grain analysis on the proppant characteristics was performed (Section 3.1.2). The bulk permeability in the Berea system was predicted and the structural changes including particle rearrangement and breakage caused by stress on the predicted permeability were characterized. The wall effects were quantified by comparing the porosity and permeability values in the interior versus the complete packings. Permeability and conductivity values for the shale fracture with a monolayer of proppants were calculated to quantify the effect of proppant embedment and/or rearrangement on transport properties for this system.

For the Berea system, the design consisted of bulk proppants instead of a monolayer – which would be a more realistic configuration – because the characteristics and behavior of bulk proppants under high loading stress needed to be determined for direct comparison to previous studies of bulk proppants. In addition, embedment at the rock-proppant interface was captured and analyzed. For the second system, a proppant monolayer was placed between shale cores. In a complementary study (Sanematsu et al., 2013), we studied the effect of embedding and crushing of the rock matrix interface on the flow.

In this work, we were mostly interested in the effect of loading stress on the flow through the proppants rather than the effect of fracture geometry and proppant distribution. For this reason, as well as ease of imaging, the fracture was created by stacking small rock cores instead of artificially or hydraulically fracturing the rocks.

3.6.1 Berea-proppant System

3.6.1.1 General Observations

As loading stress increased, proppants rearranged, embedded into the rock and eventually crushed at the highest stresses (Figure 3.4). The rearrangement of proppant particles caused changes in the pore space, which in turn modified flow pathways and increased the number of grain-grain contacts and the tortuosity. As Figure 3.4 shows, crushing occurred at 12 and 20 kpsi (83 to 138 MPa), thus increasing the number of particles, creating more surface area, and reducing porosity. Embedment of proppants into the rock was relevant because it reduced the impact of near-wall packing structures that occur in rigid-wall systems. This embedment was first observed at 8 kpsi (55 MPa) (to an extent approximately 5% of d_{50}), similar to the trend found by Much and Penny (1987). At 20 kpsi (138 MPa), we observed single-particle embedment up to approximately 35% of the d_{50}. Overall movement of the Berea faces due to the applied stress was smaller: approximately 5-10% of d_{50}.

3.6.1.2 Detailed Grain Analysis on 300^3 Cutout

A detailed analysis on a 300^3 cutout (the same cutout used for flow simulations) was performed to quantify factors that could affect flow. Fractions of grains located at the faces and edges of the cutout were not used when computing average parameters on a per-grain basis (see Section 2.5 for details).

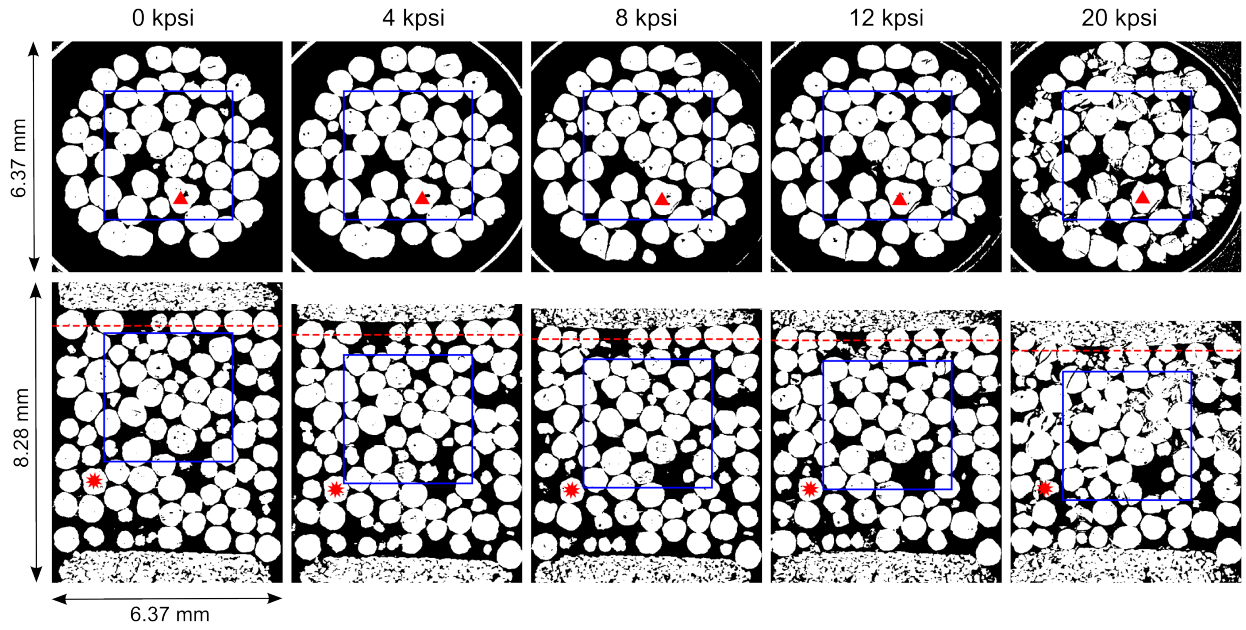

Figure 3.4: Horizontal (top row) and vertical (bottom row) cross-sections at each loading stress. Blue squares indicates FEM and LBM computational domains. Triangles and stars "follow" two different proppants at each loading stress. (For interpretation of the references to color in this figure legend, the reader is referred to the web version of this article.)

For the first 3 loadings (0, 4, 8 kpsi or 0, 28, 55 MPa respectively), similar values were found for porosity, tortuosity, permeability and the number of grains, as well as for average grain characteristics such as specific surface area, effective diameter, aspect ratio, number of grain-to-grain contacts (Table 3.2). As seen in the XCT images, these results support the finding that proppants did not crush from 0 to 8 kpsi (0 to 55 MPa), which agrees with Fredd et al. (2001), who found that a similar proppant did not crush up to 5 kpsi (34 MPa). At 12 kpsi (83 MPa), few grains were crushed (which agrees with Dusterhoft et al. (2004) who found that the crushing range for sintered bauxite was from 8 to 10 kpsi or 55 to 69 MPa). We also detected small changes in packing characteristics; i.e., the number of grains, number of grain-grain contacts, and aspect ratio, all increased (the latter indicating a departure away from spherical shape). The average grain volume, surface area and effective grain diameter decreased, supporting the visual observation that proppants were crushed.

Changes were more apparent at 20 kpsi (138 MPa), where significant changes occurred in all of these characteristics, especially the number of grains, average grain effective diameter, average number of grain to grain contacts and average aspect ratio.

Table 3.2: Detailed grain analysis (d_{50} = 697μm; *not performed in the 300^3 cutout. An xy-centered cutout including the Berea-proppant interfaces was used).

Loading (kpsi)	0	2	8	12	20
(MPa)	0	28	55	83	138
Porosity	32.92	31.69	32.75	32.14	28.46
Number of Grains	65	66	68	82	251
Inscribed Radius (μm)	319	313	304	251	131
Specific Surface Area ($\times 10^{-3} 1/\mu$m)	5.37	5.29	5.47	5.30	6.44
Effective Diameter (μm)	743	741	730	638	393
Aspect Ratio	1.34	1.36	1.47	1.83	2.70
Number of Grain-Grain Contacts	7.52	7.83	7.96	8.77	11.61
Tortuosity	1.27	1.27	1.26	1.28	1.36
Permeability (Darcy)	230.4	205.4	235.7	197.1	79.7
Single-Particle Embedment* ($\times 10\mu$m)	4.7	5.9	15	32	50

3.6.1.3 Bulk Permeability

Figure 3.5 shows predicted bulk permeability values using both FEM and LBM at all loading stresses. From 0 to 8 kpsi (0 to 55 MPa), bulk permeability remained essentially constant at approximately 225 Darcy. A small decline (12%) occurred at 12 kpsi (83 MPa), when crushing began to occur. From 12 to 20 kpsi (83 to 138 MPa), the permeability was reduced by around 60% which is due to substantial crushing of particles. Crushing was clearly the dominant factor causing permeability reduction, which is consistent with conclusions of Fredd et al. (2001) based on conductivity measurements and sieve analysis of the pre- and post-loaded proppants.

From 0 to 8 kpsi (55 MPa), structural parameters such as porosity, average grain surface area and inscribed radius, remained relatively constant, as did the tortuosity, all of which

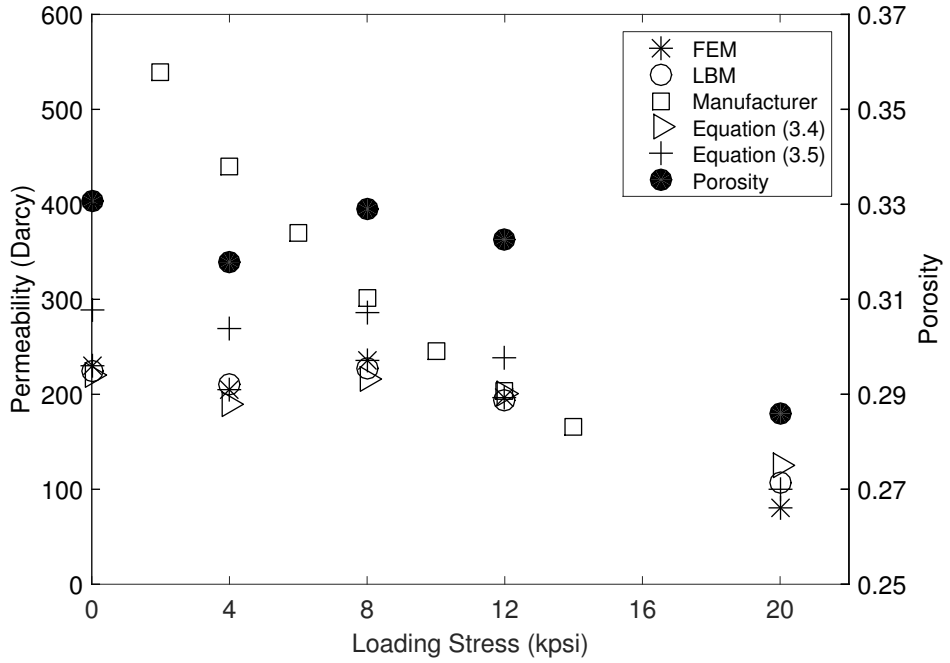

Figure 3.5: Berea-proppant system comparison of image porosity and bulk permeability predicted from FEM, LBM, CARBO Ceramics (proppant manufacturer) experimental results, Carman-Kozeny equation (3.4), Carman-Kozeny with tortuosity equation (3.5) at each loading stress.

caused permeability to remain essentially constant at these lower stresses. At 12 kpsi (83 MPa), however, proppant crushing began to alter the pore space, increasing tortuosity and thus reducing permeability. At 20 kpsi (138 MPa), the major structural changes led to increased tortuosity by approximately 6% and decreased permeability by 60% (Figure 3.5 and Table 3.2).

In Figure 3.5, bulk permeability values obtained from simulations are compared with Modified API RP-61 (ISO 13503-3) experimental results published by CARBO Ceramics, the manufacturers of the 20-40 proppant used in the Berea-proppant imaging experiments (Palisch et al., 2007). The experimental permeability results show a very smooth declining trend as loading stress was increased from 0 to 14 kpsi (0 to 97 MPa), in contrast to the

image-based flow simulations which show a more sudden onset of permeability loss at the point where major structural changes occurred.

Additional insight is gained by computing the expected permeability using the Carman-Kozeny equation, an empirical equation widely used to predict the permeability of random sphere packs. Here it is expressed in two different forms (Bear, 1988). The first is

$$k = \frac{d_p^2 \phi^3}{180(1-\phi)^2} \tag{3.4}$$

where $d_p = 697$ μm is the median particle diameter reported by the manufacturer and ϕ is the porosity (from Table 3.2).

The second form incorporates tortuosity (Wyllie and Spanger, 1952):

$$k = \frac{R_H^2 \phi}{k_0 \tau^2} \tag{3.5}$$

where R_H is the hydraulic radius, the ratio of void volume and surface area, k_0 is the shape factor of 2.5 and τ is the tortuosity (from Table 3.2).

Figure 3.5 shows that as loading stress increased from 0 to 12 kpsi (0 to 83 MPa), the discrepancy of permeability predicted from pore-scale simulations (FEM and LBM) and equation (3.4) was only ±8%. At 20 kpsi (138 MPa), equation (3.4) and equation (3.5) predicted permeability values 37% and 25%, respectively, higher than FEM simulations. The larger discrepancy of equation (3.4) – an equation used specifically for sphere packs – is likely because the significant crushing caused the proppant pack to no longer resemble a uniform sphere packing.

Velocity fields in the pore space provide a definitive link between the explanations offered above for permeability loss and the pore-scale physics that ultimately govern fluid flow. Figure 3.6 shows, for each loading stress, the normalized magnitude of velocity in cross sections from the middle of the domains obtained from 3D FEM simulation. At lower loadings, there were wide-open pore spaces where particles were not packed tightly and contain high velocities. As loading increased, pore spaces became more compact, resulting in lower and more uniform velocities in the pore space.

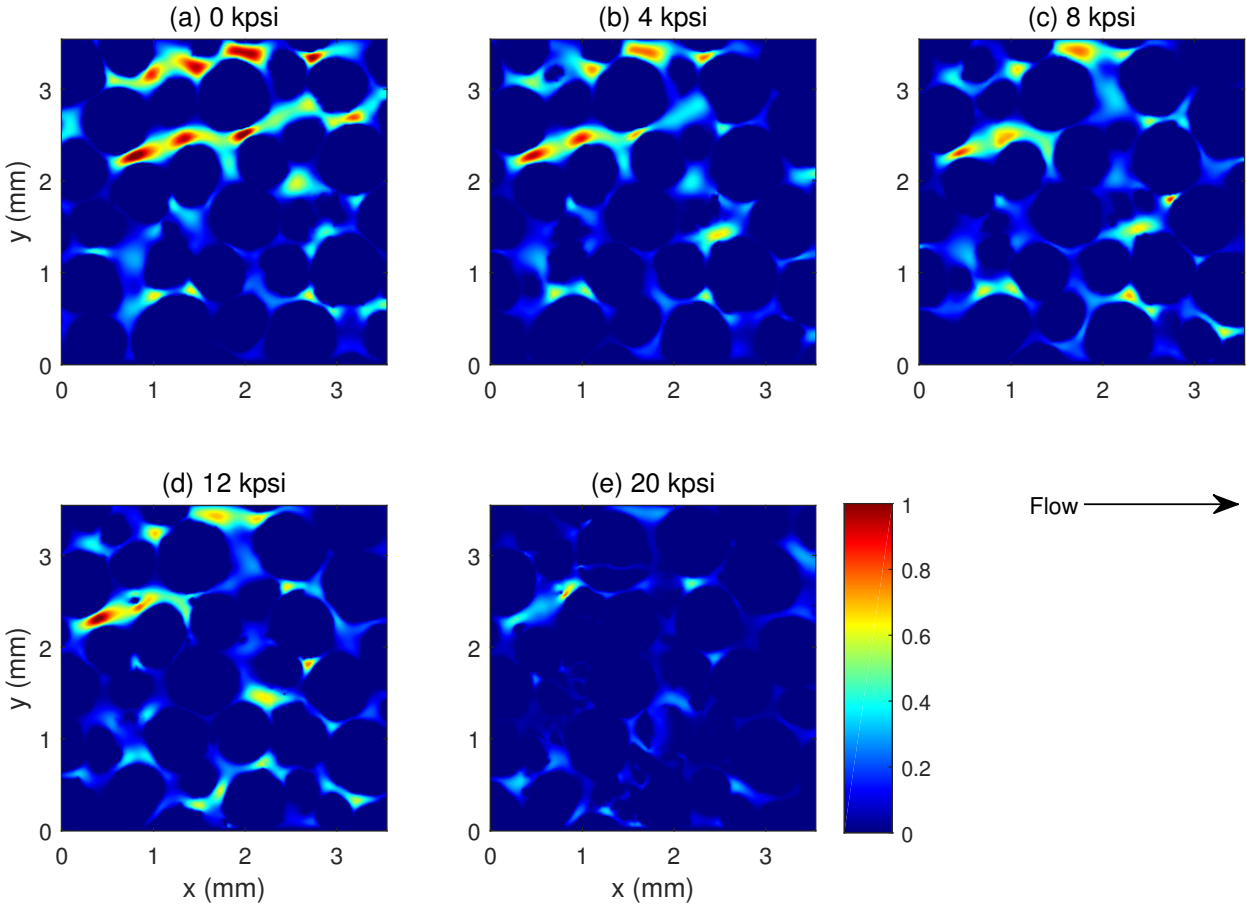

Figure 3.6: Berea-proppant system cross sections showing normalized magnitude velocity field at each loading stress.

3.6.1.4 Wall Effects

In order to investigate wall effects (which are expected to be relevant in a fracture geometry), the total porosity and total permeability were compared with bulk porosity and bulk permeability (where *bulk* refers to the internal cutout whereas *total* includes the full cross section including the area in contact with the container walls). It is important to note that the cylindrical plastic used as column walls did not deform considerably and proppants did not embed into the column walls. Thus, changes in porosity and permeability are not tied to wall deformation.

Figure 3.7 shows that both porosity and permeability follow the same declining trend as loading stress increases. The average total porosity (for all loadings) is around 6% higher than the average bulk porosity. The wall of the cylindrical container forces a more structured arrangement of proppants near the wall with sphere centers located a minimum of one radius away from the wall, which in turn corresponds to a larger local void fraction (Cohen, 1981; Sodré and Parise, 1998). From 0 to 12 kpsi (0 to 83 MPa), the total permeability is approximately 31% higher than the bulk permeability, however, at 20 kpsi (138 MPa), the total permeability is 58% higher than the bulk permeability. This result shows that wall effects became especially important at 20 kpsi (138 MPa) when proppants were crushed and the internal pore space became more tortuous and tightly packed. It also means that flow channels close to the wall remained important contributors to the total flow at all loadings, and suggests that the internal structure was more affected by crushing and/or rearrangement than the near-wall region.

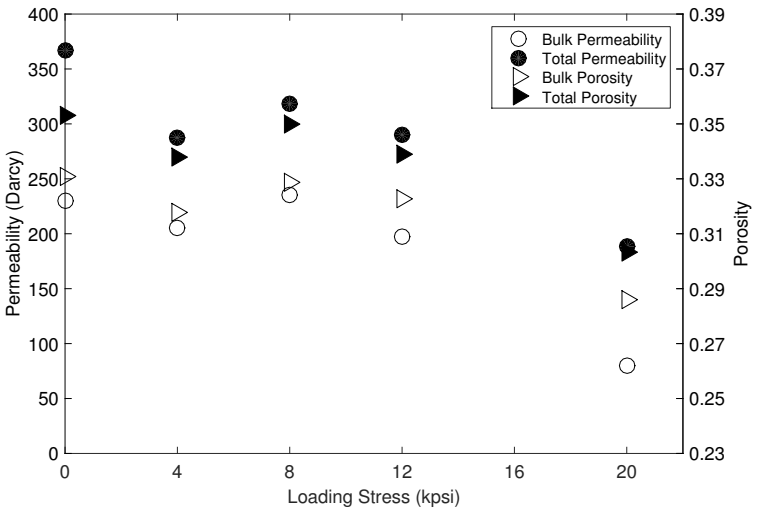

Figure 3.7: Comparison of bulk and total porosities and bulk and total permeabilities at each loading stress for the Berea-proppant system.

3.6.2 Shale-proppant Monolayer System

3.6.2.1 Observations: Embedment, Fracture Width, Porosity and Surface Area

Visual inspection shows that the rock walls changed little from 0 to 4 kpsi (0 to 28 MPa). However, from 4 to 12 kpsi (28 to 83 MPa), there was considerable embedment of proppants reaching, at the highest loading, single-particle embedment up to approximately 40% of d_{50} (see Table 3.3 for details). From the XCT images (Figure 3.8), one can see that pathways between proppants and the wall narrowed or closed after the other proppants embedded. Another important consequence of embedding for a monolayer system is the reduction of the fracture width, which decreases the fracture conductivity.

Table 3.3: Structural changes in the shale fracture system ($d_{50} = 430\mu$m).

Loading (kpsi)	0	2	8	12
(MPa)	0	28	55	83
Porosity	0.2	0.19	0.15	0.16
Specific Surface Area ($\times 10^{-3} 1/\mu$m)	5.05	4.26	4.07	5.49
Fracture Width ($\times 10\mu$m)	46	46	36	31
Single-Particle Embedment ($\times 10\mu$m)	34	37	49	66

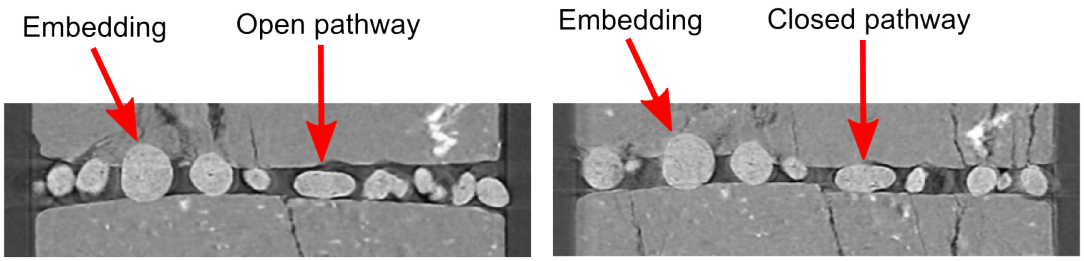

Figure 3.8: xz slice through the Shale-proppant system at 0 kpsi (left) and at 12 kpsi (right).

Fracture porosity decreased as the loading stress increased (Figure 3.9), which was a consequence mainly of the narrowing of the fracture width (allowed by particle embedment). Specific surface area of the fracture (i.e. the specific surface area of the proppants plus the shale wall) decreased significantly as the stress increased from 0 to 8 kpsi (55 MPa) (Figure 3.9), which could be attributed to the embedment of proppants into the shale. Although there was further embedment from 8 to 12 kpsi (55 to 83 MPa), specific surface area increased, reaching a value even higher than at 0 kpsi. The XCT images in Figure 3.8 indicate that some additional fissures in the shale became connected to the proppant-filled fracture at 12 kpsi (83 MPa), contributing to the large increase in total surface area. However, for the FEM

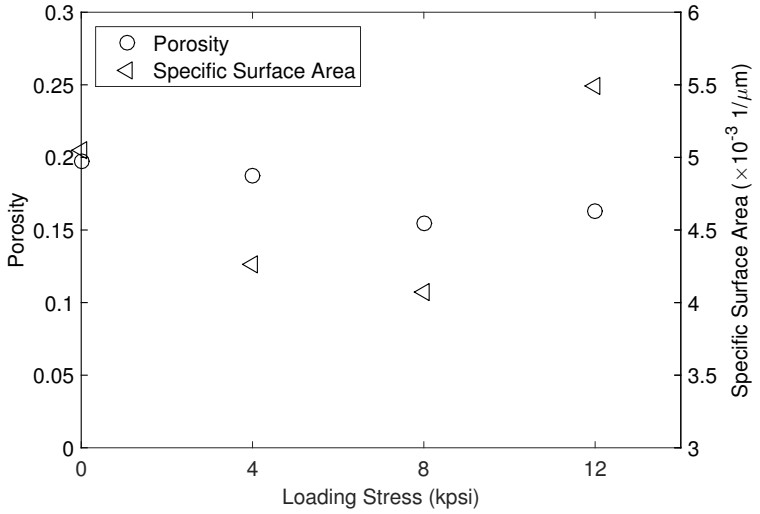

Figure 3.9: Porosity and surface area of the shale fracture as a function of the loading stress.

simulation, these additional fissures were removed from the images such that permeability and conductivity values would be comparable to other loadings.

3.6.2.2 Permeability and Conductivity

Conductivity is more relevant to well production than bulk proppant permeability because it takes into account both the width of the fracture and the material permeability between the fracture walls. In the shale system (Figure 3.10), permeability decreased by approximately 25% and another 15% when loading stress increased from 4 to 8 kpsi (28 to 55 MPa) and from 8 to 12 kpsi (55 to 83 MPa), respectively. The corresponding changes in conductivity were 40% and 25%, respectively. It can be seen from velocity fields (Figure 3.11) and the XCT images (Figure 3.8) that permeability reduction is mainly caused by two factors: particle rearrangement (which in turn causes a narrowing of the larger pores and pore throats) and embedment (which causes closure of flow channels at some locations). Conductivity is reduced by these two factors, but also decreases due to the narrowing of the overall fracture width (Table 3.3).

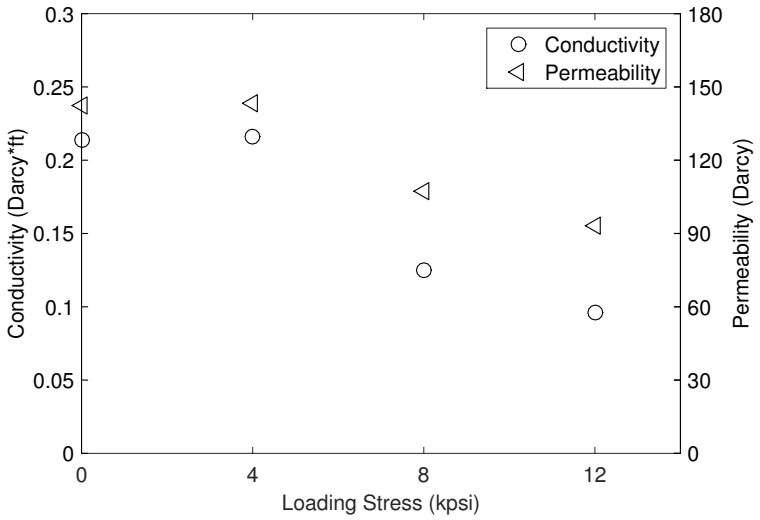

Figure 3.10: Conductivity and permeability of the shale fracture as a function of the loading stress.

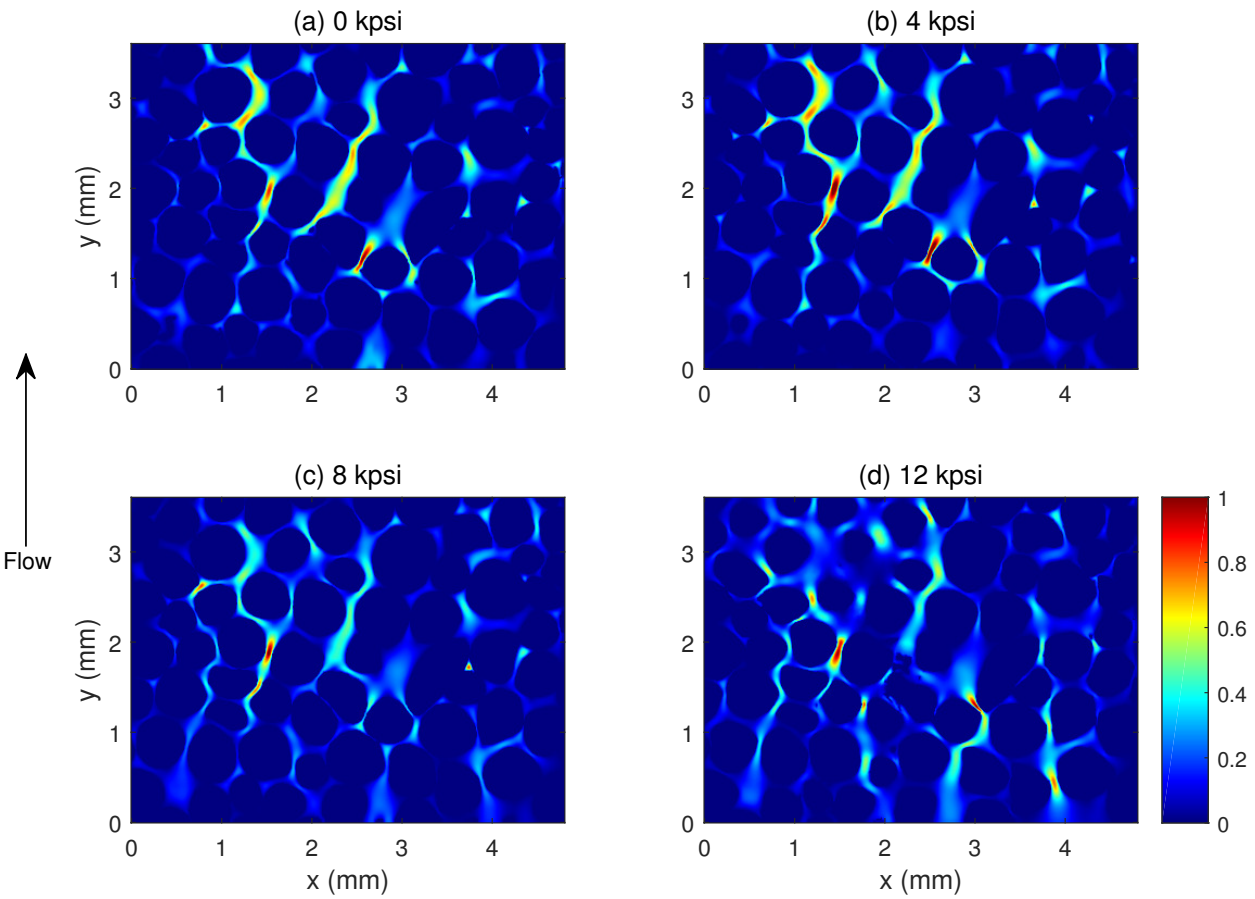

Figure 3.11: Shale-proppant system cross sections showing normalized magnitude velocity field at each loading stress.

3.6.3 Permeability Comparison: Berea Versus Shale Results

In Figure 3.12, bulk permeability values are presented for both the 20-40 proppant used in the Berea experiment and the 30-60 proppants used in the shale experiment. Results show lower permeability for the 30-60 proppant, as expected because of its smaller size. The 20-40 Berea results exhibit stress-independent permeability up to larger loadings, which is likely caused by the use of Berea versus shale at the walls and also the bulk versus monolayer packing geometry. All permeability results from our work are less dependent on applied stress than what is reported by earlier experimental work from the manufacturer (Palisch et al., 2007), until reaching stresses at which proppant particles start to crush.

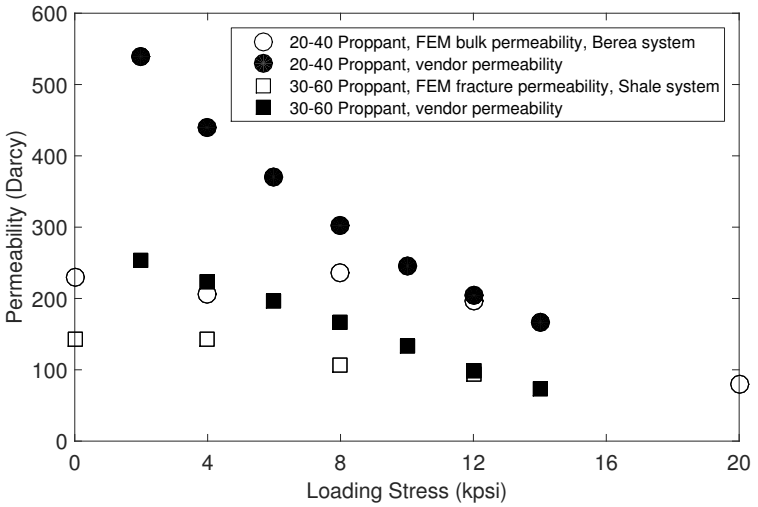

Figure 3.12: Comparison of permeability predicted from FEM simulations and experimental results from vendor of both bulk proppants and monolayer of proppants at each loading stress.

3.7 Summary and Conclusions

We have presented results from XCT imaging and image-based modeling that allow quantitative analysis of the impacts of loading on the proppant packing structure, pore space morphology, and flow properties.

For the bulk proppant contained between Berea sandstone faces, the XCT images captured structural changes (e.g. arrangement, embedding) for different loading stresses and failure of proppants at the highest loading stresses. These results are consistent with other studies that indirectly measured these changes. Flow simulations showed that the reduction of high velocity was due to elimination of the largest flow channels, which in turn led to a more uniform velocity field.

For the monolayer proppant placed between shale samples, proppant embedment was much more pronounced at high loading stress. This caused a reduction of the fracture width and a corresponding loss of fracture conductivity. As loading stress increased, narrowing of the main flow channels led to a more uniform velocity field.

The two image-based simulation approaches used here, FEM and LBM, predicted very similar permeabilities within the applied loading stresses. Finally, it is noteworthy that the permeability was essentially independent of loading at the lower stresses (below 12 kpsi or 83 MPa). This result differs from the manufacturer's data, which shows a correlation between loading and permeability over the entire range.

The images used in this study can be further used to simulate flow from the matrix into the fracture to understand skin effects, compaction of matrix pores, and effects of heterogeneity in the proppant pack. In addition to the environment studied in this paper, it would be valuable to understand how various fluids (e.g. oil, brine) affect the proppant arrangement and permeability reduction under increasing loading stress.

3.8 Acknowledgments

We thank Louisiana State University Graduate School Economic Development Assistantship (Paula Sanematsu) and ExxonMobil Upstream Research Company (URC) (Yijie Shen, Karsten Thompson and Clinton Willson) for their financial support. We thank Federico Tavarez from ExxonMobil URC for reviewing the paper and for his technical guidance on the Berea sandstone imaging. ExxonMobil URC also provided the rock and proppant samples as well as technical guidance.

Imaging was performed at GeoSoilEnviroCARS (Sector 13), Advanced Photon Source (APS), Argonne National Laboratory. GeoSoilEnviroCARS is supported by the National Science Foundation - Earth Sciences (EAR-1128799) and Department of Energy - Geosciences (DE-FG02-94ER14466). Use of the Advanced Photon Source was supported by the U. S.

Department of Energy, Office of Science, Office of Basic Energy Sciences, under Contract No. DE-AC02-06CH11357.

3.9 Supplementary Material

3.9.1 Shale-Proppant Computational Domain

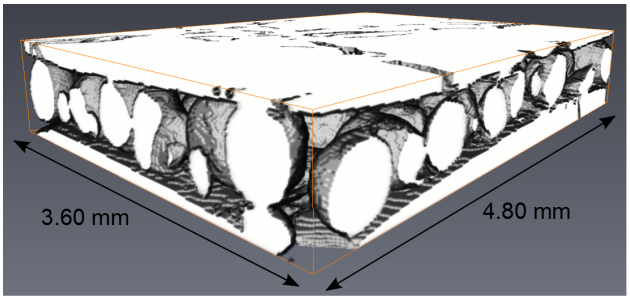

Figure 3.13: Computational domain of shale-proppant system: proppant monolayer between two shale cores.

3.9.2 Berea-Proppant Mesh

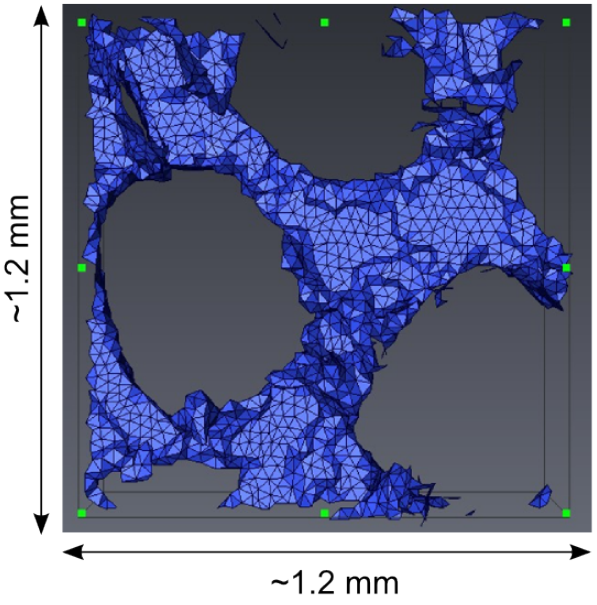

Figure 3.14: Unstructured tetrahedral mesh generated from bulk proppant segmented 3D image at 0 psi. Note: only a small section of the domain (∼1.2mm or 100 voxels) is shown here. Approximately 0.15 elements per voxel were generated at each loading stress. The commercial software Avizo was used to create unstructured mesh.

3.9.3 Lattice Boltzmann Method

The LBM equation with streaming and single velocity relaxation operator (LBGK) collision is

$$f_\alpha \left(x + e_\alpha \Delta t, t + \Delta t\right) = f_\alpha(x,t) - \frac{f_\alpha(x,t) - f_\alpha^{eq}(x,t)}{\tau} \tag{3.6}$$

where e_α are directions of particle and equilibrium distribution functions, f_α^{eq}, is

$$f_\alpha^{eq}(x,t) = w_\alpha \rho(x,t) \left[1 + \frac{e_\alpha \cdot u}{c_s^2} + \frac{(e_\alpha \cdot u)^2}{2c_s^4} - \frac{u^2}{2c_s^2}\right] \tag{3.7}$$

where w_α are weight factors specific to different directions, $c_s = 1/\sqrt{3}$ is the sound speed in the fluid, u is the velocity of the fluid, and ρ is the density of the fluid.

In LBM, positions of particles are limited to nodes of a lattice with equal spacing. In this work, the D3Q19 model is used. Velocity directions of a particle on a typical 3D lattice node is shown in Figure 3.15.

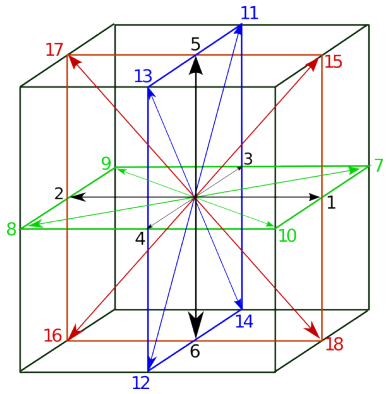

Figure 3.15: : Velocity directions of a particle on a typical 3D lattice node.

Velocity vectors for this model are described below,

$$e_\alpha = \begin{cases} (0,0,0) & \alpha = 0 \\ (\pm 1,0,0),(0,\pm 1,0),(0,0,\pm 1) & \alpha = 1,2,3,4,5,6 \\ (\pm 1,\pm 1,0),(\pm 1,0,\pm 1),(0,\pm 1,\pm 1) & \alpha = 7,8,9,10,11,12,13,14,15,16,17 \end{cases} \tag{3.8}$$

3.10 Bibliography

Arns, C. H., Knackstedt, M. a., Pinczewski, W. V., and Garboczi, E. J. (2002). Computation of linear elastic properties from microtomographic images: Methodology and agreement between theory and experiment. *Geophysics*, 67(5):1396–1405. 10.1190/1.1512785. 53

Auzerais, F. M., Dunsmuir, J., Ferréol, B. B., Martys, N., Olson, J., Ramakrishnan, T. S., Rothman, D. H., and Schwartz, L. M. (1996). Transport in sandstone: A study based on three dimensional microtomography. *Geophysical Research Letters*, 23(7):705–708. 10.1029/96GL00776. 53

Bear, J. (1988). *Dynamics of Fluids in Porous Media*. Courier Corporation. 70

Bésuelle, P., Viggiani, G., Lenoir, N., Desrues, J., and Bornert, M. (2010). X-ray micro CT for studying strain localization in clay rocks under triaxial compression. In *Advances in X-ray Tomography for Geomaterials*, chapter X-ray Micr, pages 35–52. ISTE, London, UK. 10.1002/9780470612187.ch2. 52

Bhattad, P. (2010). *Transient study of the wetting films in porous media using 3D x-ray computed micro-tomography: Effect of imbibition rate and pore geometry*. PhD thesis, Louisiana State University. 57

Bhattad, P., Willson, C. S., and Thompson, K. E. (2010). Segmentation of low-contrast three-phase x-ray computed tomography images of porous media. In *Advances in Computed Tomography for Geomaterials: GeoX 2010*, pages 254–261. John Wiley & Sons, Inc. 10.1002/9781118557723.ch30. 57

Bhattad, P., Willson, C. S., and Thompson, K. E. (2011). Effect of network structure on characterization and flow modeling using x-ray micro-tomography images of granular and fibrous porous media. *Transport in Porous Media*, 90(2):363–391. 10.1007/s11242-011-9789-7. 53

Bosl, W. J., Dvorkin, J., and Nur, A. (1998). A study of porosity and permeability using a lattice Boltzmann simulation. *Geophysical Research Letters*, 25(9):1475–1478. 10.1029/98GL00859. 53

Brannon, H. D., Wood, W. D., and Wheeler, R. S. (2006). Large-scale laboratory investigation of the effects of proppant and fracturing-fluid properties on transport. In *SPE International Symposium and Exhibition on Formation Damage Control*, pages 1–13, Lafayette, Louisiana, USA. Society of Petroleum Engineers. 10.2118/98005-MS. 48

Castro, L., Bass, C., Company, N. E., and Pirogov, A. (2013). A comparison of proppant placement, well performance, and estimated ultimate recovery between horizontal wells completed with multi-cluster plug & perf and hydraulically activated frac ports in a tight gas reservoir. In *SPE Hydraulic Fracturing Technology Conference*, pages 1–14, The Woodlands, Texas, USA. Society of Petroleum Engineers. 10.2118/163820-MS. 48

Cheremisin, A. N., Zinchenko, A., Lecerf, B. H., Pavlova, S., Thompson, K. E., and Lane, N. M. (2011). Unique, large-scale computer tomography scanner: Investigation of fracture cleanup with different materials. In *SPE Hydraulic Fracturing Technology Conference*, volume SPE-140448, pages 1–13, The Woodlands, Texas, USA. Society of Petroleum Engineers. 10.2118/140448-MS. 51, 52

Chukwudozie, C. (2011). *Pore-scale Lattice Boltzmann simulations of interial flows in realistic porous media: A first principle analysis of the Forchheimer relationship*. Master, Louisiana State University. 62

Cipolla, C. L. (2009). Modeling production and evaluating fracture performance in unconventional gas reservoirs. *Journal of Petroleum Technology*, 61(09):84–90. 10.2118/118536-JPT. 48

Cohen, Y. (1981). Wall effects in laminar flow of fluids through pocked beds. *AIChE Journal*, 27(5):705–715. 10.1002/aic.690270502. 72

Cooke, C. E. (1973). Conductivity of fracture proppants in multiple layers. *Journal of Petroleum Technology*, 25(09):1101–1107. 10.2118/4117-PA. 47, 49, 51

Dusterhoft, R., Nguyen, P., and Conway, M. (2004). Maximizing effective proppant permeability under high-stress, high gas-rate conditions. In *SPE Annual Technical Conference and Exhibition*, volume SPE-90398-, pages 1–16, Houston, TX. Society of Petroleum Engineers. 10.2118/90398-MS. 50, 67

Fredd, C., McConnell, S., Boney, C., and England, K. (2001). Experimental study of fracture conductivity for water-fracturing and conventional fracturing applications. *SPE Journal*, 6(03):288–298. 10.2118/74138-PA. 49, 67

Graham, H. L. and Kiel, O. M. (1968). Method for propping a fracture – patent us3399727. 47

Gutiérrez, G., Perazzo, G., Medina, E., Sierra, J., Henriquez, C., and Salguero, J. (2014). Successful alternating sequential hydraulic multifrac in two parallel horizontal wells in a low-permeability turbidite oil reservoir. In *SPE/EAGE European Uncoventional Conference and Exhibition*, page 13, Vienna, Austria. Society of Petroleum Engineers. 10.2118/167755-MS. 48

Hart, B. C., Sayers, C. M. S., and Jackson, A. S. (2011). An introduction to this special section: Shales. *The leading edge*, 30(3):272–273. 10.1190/1.3567257. 47

Jin, G., Patzek, T. W., and Silin, D. (2004). Direct prediction of the absolute permeability of unconsolidated and consolidated reservoir rock. In *SPE Annual Technical Conference and Exhibition*, volume SPE-90084-, pages 1–15, Houston, TX. Society of Petroleum Engineers. 10.2118/90084-MS. 53

Kaufman, P., Penny, G. S., and Paktinat, J. (2008). Critical evaluations of additives used in shale slickwater fracs. In *SPE Shale Gas Production Conference*, pages 1–9, Fort Worth, Texas. Society of Petroleum Engineers. 10.2118/119900-MS. 48

Khanna, A., Kotousov, A., Sobey, J., and Weller, P. (2012). Conductivity of narrow fractures filled with a proppant monolayer. *Journal of Petroleum Science and Engineering*, 100:9–13. 10.1016/j.petrol.2012.11.016. 53

King, G. E. (2010). Thirty years of gas shale fracturing: What have we learned? In *SPE Annual Technical Conference and Exhibition*, volume SPE-133456, pages 19–22, Florence, Italy. Society of Petroleum Engineers. 10.2118/133456-MS. 48

Koponen, a., Kataja, M., and Timonen, J. (1996). Tortuous flow in porous media. *Physical Review E*, 54(1):406–410. 10.1103/PhysRevE.54.406. 64

Koyama, T., Neretnieks, I., and Jing, L. (2008). A numerical study on differences in using NavierâĂŞStokes and reynolds equations for modeling the fluid flow and particle transport in single rock fractures with shear. *International Journal of Rock Mechanics and Mining Sciences*, 45(7):1082–1101. 10.1016/j.ijrmms.2007.11.006. 52

Lane, N. M. (2011). *Numerical studies of flow in porous media using an unstructured approach*. PhD thesis, Louisiana State University. 53, 62

Lindquist, W. B., Lee, S.-M., Coker, D. A., Jones, K. W., and Spanne, P. (1996). Medial axis analysis of void structure in three-dimensional tomographic images of porous media. *Journal of Geophysical Research*, 101(B4):8297. 10.1029/95JB03039. 53

Luffel, D. L., Hopkins, C. W., and Schettler, P. D. (1993). Matrix permeability measurement of gas productive shales. In *SPE Annual Technical Conference and Exhibition*, volume SPE-26633-. Society of Petroleum Engineers. 10.2118/26633-MS. 48

Maxwell, S. (2011). Microseismic hydraulic fracture imaging: The path toward optimizing shale gas production. *The leading edgeThe leading edge*, 30(3):340–346. 10.1190/1.3567266. 48

Much, M. and Penny, G. (1987). Long-term performance of proppants under simulated reservoir conditions. In *Low Permeability Reservoirs Symposium*, page 10, Denver, Colorado. Society of Petroleum Engineers. 10.2118/16415-MS. 49, 51, 66

Oh, W. and Lindquist, W. (1999). Image thresholding by indicator kriging. *Pattern Analysis and Machine Intelligence, IEEE Transactions on*, 21(7):590–602. 10.1109/34.777370. 57

Oren, P. l.-E. and Bakke, S. (2003). Reconstruction of berea sandstone and pore-scale modelling of wettability effects. *Journal of Petroleum Science and Engineering*, 39(3-4):177–199. 10.1016/S0920-4105(03)00062-7. 53

PALABOS (2012). Palabos CFD complex physics project. www.palabos.org. 62

Palisch, T. T., Duenckel, R. J., Bazan, L. W., Heidt, J. H., and Turk, G. a. (2007). Determining Realistic Fracture Conductivity and Understanding its Impact on Well Performance - Theory and Field Examples. In *SPE Hydraulic Fracturing Technology Conference*, volume SPE-106301, pages 1–13, College Station, Texas. Society of Petroleum Engineers. 10.2118/106301-MS. 69

Petunin, V. V., Yin, X., and Tutuncu, A. N. (2011). Porosity and permeability changes in sandstones and carbonates under stress and their correlation to rock texture. In *Canadian Unconventional Resources Conference*, volume SPE-147401, pages 1–14, Calgary, Alberta, Canada. Society of Petroleum Engineers. 10.2118/147401-MS. 52

Ramurthy, M., Magill, D., Parker, M., and Sanchez, P. W. (2013). Case history: Production results from partial monolayer proppant fracture treatments in the pictured cliffs formation horizontal wells of san juan basin. In *SPE Hydraulic Fracturing Technology Conference*, pages 1–12, The Woodlands, Texas, USA. Society of Petroleum Engineers. 10.2118/163815-MS. 48

Raynaud, S., Ngan-Tillard, D., Desrues, J., and Mazerolle, F. (2008). Brittle-to-ductile transition in Beaucaire marl from triaxial tests under the CT-scanner. *International Journal of Rock Mechanics and Mining Sciences*, 45(5):653–671. 10.1016/j.ijrmms.2007.08.007. 52

Sanematsu, P., Willson, C. S., and Thompson, K. E. (2013). Image-based modeling of the flow transition from a Berea rock matrix to a propped fracture. In *AGU Fall Meeting*, number H34E-04, San Francisco, CA. 65

Schure, M. R., Maier, R. S., Kroll, D. M., and Ted Davis, H. (2004). Simulation of ordered packed beds in chromatography. *Journal of Chromatography A*, 1031(1-2):79–86. 10.1016/j.chroma.2003.12.030. 53

Sodré, J. R. and Parise, J. A. R. (1998). Fluid flow pressure drop through an annular bed of spheres with wall effects. *Experimental Thermal and Fluid Science*, 17(3):265–275. 10.1016/S0894-1777(97)10022-X. 72

Sondergeld, C. H., Newsham, K. E., Comisky, J. T., Rice, M. C., and Rai, C. S. (2010). Petrophysical considerations in evaluating and producing shale gas resources. In *SPE Unconventional Gas Conference*, Pittburgh, Pennsilvania. Society of Petroleum Engineers. 10.2118/131768-MS. 47

Takbiri Borujeni, A. (2013). *Multi-scale modeling of inertial flows through propped fractures*. PhD thesis, Louisiana State University. 62

Takbiri Borujeni, A., Lane, N., Thompson, K., and Tyagi, M. (2013). Effects of image resolution and numerical resolution on computed permeability of consolidated packing using LB and FEM pore-scale simulations. *Computers & Fluids*, 88:753–763. 10.1016/j.compfluid.2013.05.019. 62

Thompson, K. E. (2007). Computing particle surface areas and contact areas from three-dimensional tomography data of particulate materials. *Particle & Particle Systems Characterization*, 24(6):440–452. 10.1002/ppsc.200601139. 59

Thompson, K. E., Willson, C. S., White, C. D., Nyman, S., Bhattacharya, J. P., and Reed, A. H. (2008). Application of a new grain-based reconstruction algorithm to microtomography images for quantitative characterization and flow modeling. *Society of Petroleum Engineers Journal*, 13(2):164–176. 10.2118/95887-PA. 53

Thompson, K. E., Willson, C. S., and Zhang, W. (2006). Quantitative computer reconstruction of particulate materials from microtomography images. *Powder Technology*, 163(3):169–182. 10.1016/j.powtec.2005.12.016. 60, 61

Wang, Y., Uchida, T., Westferro, F., Rivers, M. L., Nishiyama, N., Gebhardt, J., Lesher, C. E., and Sutton, S. R. (2005). High-pressure x-ray tomography microscope: Synchrotron computed microtomography at high pressure and temperature. *Review of Scientific Instruments*, 76(7):0737091–0737097. 10.1063/1.1979477. 56

Warpinski, N. R., Mayerhofer, M. J., Vincent, M. C., Cipolla, C. L., and Lolon, E. P. (2008). Stimulating unconventional reservoirs: Maximizing network growth while optimizing fracture conductivity. In *SPE Unconventional Reservoirs Conference*, volume SPE-114173. 10.2118/114173-MS. 48

Willson, C. S., Lu, N., and Likos, W. J. (2012). Quantification of grain, pore, and fluid microstructure of unsaturated sand from x-ray computed tomography images. *Geotechnical Testing Journal*, 35(6):20120075. 10.1520/GTJ20120075. 61

Wornstaff, V., Hagen, S., Ignacz, T., Hughes, B., Chorney, M., and Pedersen, B. (2014). Solid paraffin inhibitors pumped in hydraulic fractures increase oil recovery in viking wells. pages 1–7, Lafayette, Louisiana, USA. Society of Petroleum Engineers. 10.2118/168147-MS. 48

Wyllie, M. R. J. and Spanger, M. B. (1952). Application of electrical resistivity measurements to problem of fluid flow in porous media. *American Association of Petroleum Geologists Bulletin*, 36(2):359–403. 70

Ye, X., Tonmukayakul, N., Weaver, J. D., and Morris, J. F. (2012). Experiment and simulation study of proppant pack compression. In *SPE International Symposium and Exhibition on Formation Damage Control*, volume SPE-151647, pages 15–17, Lafayette, Louisiana, USA. Society of Petroleum Engineers. 10.2118/151647-MS. 50, 51

Zhan, X., Schwartz, L. M., Toksöz, M. N., Smith, W. C., and Morgan, F. D. (2010). Pore-scale modeling of electrical and fluid transport in Berea sandstone. *Geophysics*, 75(5):F135–F142. 10.1190/1.3463704. 53

Zhao, Z.-c., Cui, B., Yue, Y.-q., Wang, L.-y., and Wu, Y.-x. (2008). Numerical simulation of horizontal migration of proppant*. *Journal of Hydrodynamics, Ser. B*, 20(1):74–80. 10.1016/S1001-6058(08)60030-X. 52

4. Nanoparticle Transport Model

4.1 Abstract

Nanoparticles (NPs) have been widely used commercially and have the potential to be extensively used in petroleum engineering as stabilizers in enhanced oil recovery operations or as tracers or sensors to detect rock and fluid properties. In spite of a wide range of applications, many NP transport details are still unknown. Column experiments, where a NP solution is injected and effluent concentration history is measured, are currently the most common approach to understand NP mobility and deposition. However, this approach does not provide any insights into the pore-level processes and the system must be destroyed to analyze deposition. Modified colloid filtration theory (CFT) has also been used for many years to understand colloid transport, and most recently, NP transport. Again, this model fails to provide pore-level details of the processes affecting particle fate and transport. Micromodels have a transparent top cover that allows researchers to see particles traveling the domain. They have been used to overcome "visualization" issues and to investigate pore-level mechanisms.

In this work, we describe a NP transport model that can be used to better understand the impact of pore-scale hydrodynamics and surface forces on NP transport. First, an unstructured mesh is created based on the pore space of a segmented x-ray computed tomography image of a Berea sandstone and a 2.5D micromodel. Finite element method (FEM) of Stokes flow is implemented to solve for pressure and velocity at the mesh nodes. The NP transport code accounts for three main transport processes: hydrodynamic forces, Brownian motion, and surface forces. However, the flexibility of the numerical scheme allows the addition of forces.

The effects of particle size, attractive and repulsive surface forces, flow rate, particle density, and surface capacity (site blocking), and surface forces mapped to XCT-image based mineralogy were studied. Larger particles traveled, on average, faster than smaller particles. Consistent with experimental and modeling results, attractive surface forces decreased effluent concentrations whereas repulsive surface forces increased effluent concentration. In the presence of attractive surface forces, NP recovery increased as particle diameter increased. Flow rate (micromodel only) showed the biggest impact on NP recovery when attractive surface forces were present, especially for bigger particles. An increase in flow rate increased NP recovery. Particle density showed a negligible effect, which disagreed with experimental results. Compared to unlimited attachment, surface capacity decreased particle retention in the Berea by limiting the number of particles that could attach to the wall.

4.2 Introduction

Nano engineered materials have emerged as a new technology with application across many areas such as drug delivery, contaminant remediation, oil and gas exploration and production, and cosmetics. Government-reported investment in nanotechnology around the world has increased more than six times from 1997 to 2003, from $430 million to $3 billion, and is expected to reach $1 trillion by 2015 (Roco, 2003). At the same time, concerns regarding health and environmental safety have also increased, with peer-reviewed publications growing more than ten times in thirteen years, from about 100 in 2000 to more than 1,300 in 2013 (Maynard, 2014). One of the issues addressed by some of these publications is particle fate and transport, the area that this work concentrates on.

Particularly, we are interested in nanoparticle (NP) transport in porous media at the pore scale and the mechanisms that cause retention and/or facilitated transport of NPs.

Studies that address NP transport in porous media generally use an experimental approach. Although experiments provide valuable information (e.g., effluent curves, adsorption rates) about factors that affect NP transport in porous media (e.g., flow rate, NP concentration, types of porous media, etc.), some details remain hard to identify, especially those related to visualization of NPs inside the porous media, for example, the location of adsorption sites and the effect of complex geometry at the pore scale.

A common modeling approach is the modified colloid filtration theory (CFT), which has brought new insights and improved our understanding about the mechanisms that affect NP retention in porous media. However, as with column experiments, it does not provide location and visualization of retention sites neither allows the modeling of favorable and unfavorable forces simultaneously.

In order to provide more insights on fluid flow and particle transport behaviors in porous media, researchers have used micromodels (Park et al., 2012). Micromodels are typically 2D artificial geometries that are idealized patterns or represent real rocks by honoring rock geometry, topology, or dynamic flow parameters such as velocity and permeability (Buchgraber et al., 2011; Park et al., 2012). Most importantly, the transparency of midromodels allows direct observation of flow and transport processes. Due to their ease of visualization, micromodels have been widely used to investigate two-phase flow displacement instabilities (e.g., Chuoke et al. (1959), Clemens et al. (2013), Buchgraber et al. (2011)), two-phase flow in fractured media (e.g, Rangel-German and Kovscek (2006)), two-phase flow in dual porosity media (e.g., Buchgraber et al. (2012)), and particle transport (e.g., Yoon et al.

(2006)) – detailed reviews of micromodels can be found in Buckley (1991) and Wan et al. (1996).

In addition to theoretical and experimental methodologies, numerical modeling has also been used to understand fluid flow and particle transport in porous media. Two general approaches are commonly used to model particle transport: Eulerian-Eulerian (EE) and Eulerian-Lagrangian (EL).

The EE approach uses continuity and momentum equations to simulate flow and particle transport; particles and fluid are considered separate phases that interpenetrate (Larimi et al., 2014; Tu et al., 2013). Various methods exist to link the particle and fluid phases. For example, when volumetric fractions of phases are used, a net rate of mass transfer term is introduced in the continuity equation. Similarly, a momentum exchange term is added to the momentum equations. This term includes the particle forces such as drag, lift, buoyancy, etc. (Tu et al., 2013). EE methodology is commonly used to investigate fine and ultrafine aerosol deposition (Broday, 2004; Shi et al., 2006). Although the EE approach provides a robust and computationally efficient formulation based on first principles that can be applied to dense and dilute solutions, it does not consider microscopic transport processes (e.g. inertial, electrostatic effects) (Longest and Xi, 2007; Tu et al., 2013). Moreover, it would be a cumbersome method to apply in a very complex geometry such as porous medium.

The EL approach solves the Navier-Stokes equations for the fluid phase using an Eulerian method (e.g., lattice Boltzmann, finite element, finite difference) and, after the flow field is resolved, Lagrangian particle tracking (LPT) is applied. In the Lagrangian method, particles are individually tracked using Newton's second law of motion and the position equation,

respectively (Guha, 2008; Larimi et al., 2014; Tu et al., 2013):

$$m_p \frac{d\mathbf{v}_p}{dt} = \sum \mathbf{F} \tag{4.1}$$

$$\frac{d\mathbf{x}_p}{dt} = \mathbf{v}_p \tag{4.2}$$

where m_p is the particle mass, $\mathbf{v}_p$ is the particle velocity, and $\mathbf{F}$ represents the forces acting on the particle, and $\mathbf{x}_p$ is the particle position. These coupled ordinary differential equations (ODEs) can be numerically integrated and the particle trajectory determined within the domain. $\mathbf{F}$ is generally composed of the following forces: drag, lift, buoyancy, thermophoretic, force due to Brownian motion, Magnus, and Basset, but other forces may be added according to the system studied (Guha, 2008; Larimi et al., 2014; Tu et al., 2013) – Larimi et al., for example added a magnetic term.

Particles interchange mass, momentum, and energy with the fluid phase. Interaction between the particle and fluid phases is classified into three categories depending on how particles and fluid interact and exchange forces as well as the interaction between particles. Elghobashi (1994) classified these interactions based on particle volume fraction, α (particle volume divided by the total volume). *One-way* coupling, for dilute solutions with $\alpha < 10^{-6}$, occurs when the fluid phase influences particles but particle forces on the fluid can be neglected – because their volume fraction is negligible. *Two-way* coupling, for solutions with $10^{-6} < \alpha < 10^{-3}$, occurs when fluid affects particle trajectories and particles affect fluid flow. *Four-way* coupling, for dense solutions $\alpha > 10^{-3}$, means that not only the forces between fluid and particle need to be taken into account, but also particle-particle interactions.

The EL approach is commonly used to model aerosol transport where solutions of fine and ultrafine particles are typically dilute, thus allowing one-way coupling to be used (Robinson et al., 2006; Zamankhan et al., 2006). Wang et al. (2005) implemented an EL methodology to model aerosol particles in gas in a 2D geometry of aerodynamic lenses. They included drag and force due to Brownian motion. Mehel et al. (2010) modeled micro- and nano-particle deposition in wall-bounded turbulent 3D vertical and horizontal channel flows as well as circular pipe flows. In addition to drag and force due to Brownian motion, they also included lift and gravity. Longest and Xi (2007) modeled deposition of ultrafine aerosols in upper oral airways of the human respiratory system by considering drag and force due to Brownian motion. These simulations represent additional geometric complexity compared to most other previous works and thus are more relevant to our work.

Advances in computational methods for flow in porous media involving porous media characterization (e.g. x-ray computed micro tomography) and flow modeling have allowed the development of LPT models in porous media. However, only a few studies investigated particle transport in porous media using the EL approach. The complex pore-scale geometries observed in many natural porous media represent a significant challenge for implementation because particle-surface interactions are more common in porous media and they need to be handled carefully in the numerical scheme. In addition, porous media can exhibit low-flow and backward-flow zones, creating zones that particles can be trapped, but not necessarily attached to a surface (Li et al., 2012). Pham et al. (2014) developed an EL methodology using lattice Boltzmann simulations in porous media method and successfully validated against experimental effluent concentration. Nevertheless, the geometry consisted of a sphere pack (an ideal porous media) with only a few pores and they introduced particle

attachment through a probabilistic term. Li et al. also developed a LPT algorithm based on lattice Boltzmann simulations. They performed image-based flow simulations in glass beads under favorable[1] conditions (based on DLVO theory – for details on DLVO theory, see Lyklema et al. (1999)) and studied particle retention for different colloid sizes and flow conditions.

In this study, we develop a nanoparticle transport model for porous media using an EL approach. The presented methodology uses an unstructured mesh built from an XCT image of a real material and employs the finite element method to solve Stokes flow. Unlike LBM methods that use structured grids, unstructured meshing can decouple image resolution from mesh resolution. This decoupling makes FEM less computationally intensive and thus allowing simulations in larger domains. In addition, unstructured meshing allows finer resolution in specific areas of interest to improve local accuracy and resolution. For example, a narrow throat that is only a few voxels wide whereas most of the domain features have hundreds to voxels. In general, FEM is more computationally efficient than LBM when solving Stokes flow in porous media. However, attention is necessary when using local refinement because it can considerably increase the mesh size and, therefore, affect its computational efficiency.

Simulations in this work were performed in a real rock (Berea sandstone), but most simulations were performed in a novel performed in a novel 2.5D micromodel system developed by Park et al. (2012). The 2.5D micromodel allowed ease of visualization and

[1]Favorable/unfavorable is a common term in colloid transport that means favorable/unfavorable, respectively, for particle retention.

more intuitive geometry – when compared with a 3D porous medium – that helped us interpret the results.

4.3 Materials and Methods

4.3.1 Assumptions

We assume one-way coupling is valid because NP concentration is low and because NP are stable and do not aggregate. These are reasonable assumptions considering several experiments used low concentration and stable solutions to quantify adsorption in which they also disregarded aggregation effects (Zhang et al., 2014). Previous modeling works in fine and ultrafine aerosol transport (e.g. Longest and Xi (2007); Zamankhan et al. (2006)) and colloid transport in porous media also assumed one-way coupling (e.g. Johnson et al. (2007); Pham et al. (2014)). Given these premises, it is plausible to track particle paths independently, one particle at a time.

In general, particles may be retained in the porous media through straining, attachment, gravitational sedimentation, and Brownian diffusion (Figure 4.1). For conventional reservoir rocks, NP size is 2-3 orders of magnitude smaller than pore throats (Zhang et al., 2014). Therefore, straining is negligible (considering particles do not aggregate) and retention is only caused by particle-surface forces (Nowack and Bucheli, 2007).

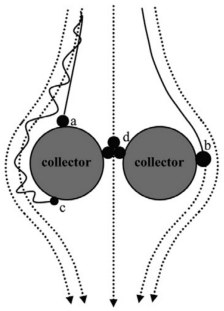

Figure 4.1: Retention processes: (a) gravitational sedimentation, (b) interception, (c) Brownian diffusion, and (d) NP aggregation, from Lin et al. (2010)

4.3.2 Micromodel XCT Image

A rock-based polymethylmethacrylate (PMMA) micromodel ($2\times2\times1.3$ mm^3), designed and fabricated by Park et al. (2012), was imaged using XCT at a voxel resolution of 2.3 μm at the Advanced Photon Source GSECARS at Argonne National Laboratory. The image was reconstructed using a filtered-back projection algorithm (Rivers, http://cars9.uchicago.edu/software/idl/tomography.html), smoothed by anisotropic diffusion and segmented by interactive thresholding using the commercial software Avizo. (Image collection and processing were performed by Godfrey Mills and the details of that part of the work will be published in the future). The dimensions of the final segmented image were $870\times871\times56$ voxels, corresponding to $2.00\times2.00\times0.13$ mm^3.

4.3.3 Berea XCT Image

A Berea sample, 5 mm in diameter and $\sim$15 mm in length, was imaged using XCT at a voxel resolution of 4.12 μm at the Advanced Photon Source GSECARS at Argonne National Laboratory and produced a scanned imaged that was $\sim$12 mm long (Mills et al., 2013). After reconstruction, the image was processed (filtered and segmented) using various methods to generate a multi-phase image with defined mineralogy. The final multi-phase image was composed of void and three minerals with dimensions $850\times850\times551$ voxels, corresponding to $3.50\times3.50\times2.27$ mm^3. In this work, a $200\times200\times300$ voxels or $0.84\times0.84\times1.24$ mm^3 cropped section of the XCT image (Figure 4.2, a.) segmented into void and three minerals (Figure 4.2, b.) was used.

A thin section of the Berea was analyzed using x-ray diffraction (XRD) at Louisiana State University to identify the minerals. The mineralogical composition is displayed in Table 4.1.

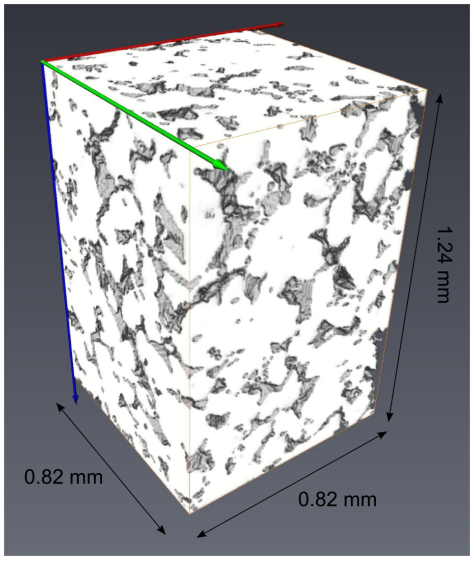

(a) Volume rendering of cropped section of Berea XCT image.

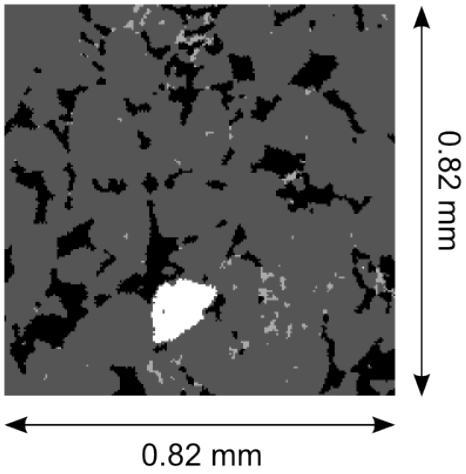

(b) Cross section of multi-phase segmented image.

Figure 4.2: Berea XCT image.

Table 4.1: Berea mineralogical composition (Thompson, 2014 AEC Annual Report).

Mineral	Thin Slice (XRD)	XCT
Quartz/Feldspar	95	97.8
Clay	5.0	1.50
$CaCO_3$	trace	0.73

4.3.4 Unstructured Mesh and Finite Element Method Flow Modeling

Taylor-Hood elements (Figure 2.4) are tetrahedrons containing four pressure nodes (vertices) and ten velocity nodes (four vertices and six edges' mid-points). An in-house code described by Lane (2011) was used to created an unstructured mesh of Taylor-Hood elements. Meshes of increasing resolution were generated to assess whether the flow rate, velocity profiles, and particle deposition efficiency were sensitive to mesh resolution.

Stokes flow was solved using FEM as implemented by Lane (2011). Constant traction (normal component) boundary conditions were imposed at the inlet and outlet of the domain

with flow in the y-direction. No-slip boundary conditions were imposed on the other six faces of the domain as well as on the interior solid/void surfaces..

4.3.5 Image-Based Mineralogy

In order to understand the effect of different minerals in reservoir rocks on NP transport, the unstructured mesh was labeled according to the multi-phase segmented image (Figure 4.2b). Only wall surface elements need to be labeled since pore elements correspond to the void phase. The mesh labeling was performed per tetrahedron face. Each tetrahedron face (i.e., a triangle) has three nodes. Based on the node location and where it corresponds in the XCT image, a phase was assigned. Table 4.2 shows the XCT and mesh mineralogical composition.

Table 4.2: Berea mineralogical composition.

Mineral	XCT	Mesh
Quartz/Feldspar	97.8	97.7
Clay	1.50	2.03
$CaCO_3$	0.73	0.27

It is important to note that the mesh values indicate percentage of tetrahedron faces whereas XCT values indicate percent volume. In addition, the XCT values were obtained from the full domain 850×850×551 voxels or 3.50×3.50×2.27 mm^3 and the mesh values from the cropped section, 200×200×300 voxels or 0.84×0.84×1.24 mm^3 (Figure 4.2a). Although different values are compared, for the purpose of this work as a proof of concept, the results are acceptable.

4.3.6 Nanoparticle Transport Model

The governing equations for particle tracking are given by Newton's second law and the position equation, Equations (4.1) and (4.2), respectively. Because NPs have such small mass, in the order of 10^{-9} kg, inertia is negligible (Longest and Xi, 2007) and the particle response to the fluid flow is instantaneous, i.e. the particle velocity is the same as the fluid velocity. Therefore, Equation (4.1) and (4.2) can be simplified and the governing equations become:

$$\sum \mathbf{F} = 0 \tag{4.3}$$

$$\frac{d\mathbf{x}_p}{dt} = \mathbf{v}_f \tag{4.4}$$

where $\mathbf{v}_f$ is the fluid velocity. Equation (4.3) can be combined to Equation (4.4) by calculating the resisting drag, $\mathbf{F}_{\text{drag}*}$, created when the particle is moved due to surface forces, gravity, etc. (excluding the driving hydrodynamic drag, i.e. the fluid velocity). The sum of forces can be expanded:

$$\sum \mathbf{F} = \mathbf{F}_{\text{drag}*} + \mathbf{F}_{\text{gravity}} + \mathbf{F}_{\text{surface}} + \cdots = 0 \tag{4.5}$$

There are numerous formulations for $\mathbf{F}_{\text{drag}*}$ that account and approximate different physical behaviors. Ma et al. (2009), for example, accounts for drag normal and tangential to the surface as well as drag surface from near a wall. Here, $\mathbf{F}_{\text{drag}*}$ is simply described by Stokes drag:

$$\mathbf{F}_{\text{drag}*} = 6\pi\mu r_p \left(-\mathbf{v}_{\text{forces}}\right) \tag{4.6}$$

Substituting Equation (4.5) into Equation (4.6) yields

$$\mathbf{v}_{\text{forces}} = \frac{1}{6\pi\mu r_p}\left(\mathbf{F}_{\text{gravity}} + \mathbf{F}_{\text{surface}} + \cdots\right) \tag{4.7}$$

where μ is the fluid dynamic viscosity and r_p is the particle radius. The relevant forces in the system can be added to Equation (4.7).

Finally, Brownian motion is added Equation (4.4) as a random displacement (Nelson and Ginn, 2005):

$$\mathbf{B} = \mathbf{n}\sqrt{2D_M\Delta t} \tag{4.8}$$

where $\mathbf{n}$ is a vector with components in x, y, z directions that are random numbers of a Gaussian distribution with zero mean and unity variance, D_M is the diffusion coefficient, and Δt is the time step during the displacement. D_M is diffusion coefficient for spherical particles given by the Stokes-Einstein law of diffusion (Dill and Bromberg, 2011)

$$D_M = \frac{k_B T}{6\pi\mu r_p} \tag{4.9}$$

where $k_B = 1.3806488 \times 10^{-23}$ m^2 kg s^{-2} K^{-1}, the Boltzmann constant, T is the absolute temperature, and μ is the dynamic viscosity.

Combining Equations (4.4, 4.7, and 4.8), the governing equation to be discretized in this study becomes:

$$\frac{d\mathbf{x}_p}{dt} = \mathbf{v}_f + \mathbf{v}_{\text{forces}} + \mathbf{B} \tag{4.10}$$

4.3.6.1 Numerical Scheme

An operator splitting scheme is implemented to numerically integrate Equation (4.10). The first step of the operator splitting computes the first term of the right hand side (RHS) of Equation (4.10) using fourth order Runge-Kutta:

$$\mathbf{x}_p^{'} = \mathbf{x}_p^n + \frac{1}{6}\left(k_1 + 2k_2 + 2k_3 + k_4\right) \tag{4.11}$$

where n is the discrete time and

$$\begin{aligned} k_1 &= \Delta t\ \mathbf{v}_f\left(\mathbf{x}_p^n\right) \\ k_2 &= \Delta t\ \mathbf{v}_f\left(\mathbf{x}_p^n + \frac{k_1}{2}\right) \\ k_3 &= \Delta t\ \mathbf{v}_f\left(\mathbf{x}_p^n + \frac{k_2}{2}\right) \\ k_4 &= \Delta t\ \mathbf{v}_f\left(\mathbf{x}_p^n + k_3\right) \end{aligned} \tag{4.12}$$

and Δt is an adaptive time step that is dependent on the gap distance, d_{gap}, the distance between the particle surface and the solid surface:

$$\Delta t = \alpha\ \frac{d_{\text{gap}}}{\|\mathbf{v}_f\|} \tag{4.13}$$

where α is the time step multiplication factor. The choice of Δt is to improve computations time by allowing large displacements away from the surface – most likely in large pores – and small displacements close the surface, most likely in pore throats. The rationale for the adaptive time step is, assuming the particle was moving straight at the surface (i.e., perpendicular to the surface), Δt would be the the time the particle would take to reach the

wall. In most cases, however, particles do not move perpendicular to the wall and therefore, Δt provides a conservative time step.

The second step of the operator splitting solves the second term on the RHS of Equation (4.10) with a Euler discretization:

$$\mathbf{x}_p^{''} = \mathbf{x}_p^{'} + \Delta t \; \mathbf{v}_{\text{forces}} \tag{4.14}$$

The third and final step adds the Brownian displacement:

$$\mathbf{x}_p^{n+1} = \mathbf{x}_p^{''} + \mathbf{B} \tag{4.15}$$

The initial condition for Equation (4.11) is the inlet location provided by a function that is flow-rate biased, i.e., inlet channels with high flow rate receive more particles than low flow rate channels.

4.3.6.2 Forces

1. Gravity: the force due to gravity is

$$\mathbf{F}_{\text{gravity}} = (\rho_p - \rho_{\text{fluid}})\, V_p \, \mathbf{g} \tag{4.16}$$

   where ρ_p is the particle density, ρ_{fluid} is the fluid density, V_p is the particle volume, $\mathbf{g}$ is the acceleration of gravity.

2. Surface forces: the model developed in this study has a flexible scheme to implement surface forces with a "black box" approach. This type of approach allows the use of surface forces acquired by various methods (e.g., numerical simulations, theoretical,

experimental) to be implemented. As long as the surface force data is in the format "force *vs.* distance", then it can be incorporated into the model. Options we have implemented include tabulated data from molecular dynamics simulation results (Figure 4.3, a.) or formulas based on Derjaguin-Landau-Verwey-Overbeek (DLVO) theory (Figure 4.3, b.) from Zypman (2006). However, only the DLVO theory results were presented. The force *vs.* distance profile from Zypman was chosen due to its application to colloid transport in porous media.

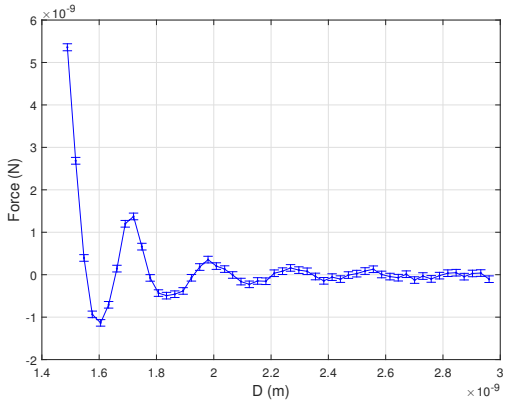

(a) Molecular dynamics simulation (D.E. Nikitopoulos, personal communication).

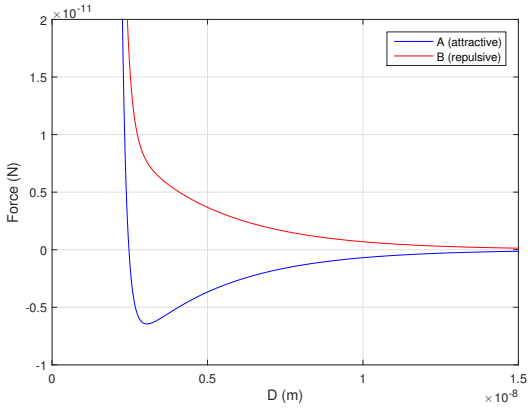

(b) DLVO, from Zypman (2006).

Figure 4.3: Examples of surface forces acting on the particle in the direction normal and away from the surface (towards the particle) which means that a positive force is repulsive and a negative force is attractive.

4.3.6.3 Brownian Motion

The displacement due to Brownian motion was implemented according to Nelson and Ginn (2005) and Dill and Bromberg (2011) using Equations (4.8, 4.9). When Brownian motion caused the particle to reach a wall, an elastic collision was performed. It is also possible to perform inelastic collision to simulate energy losses. Figure 4.4 illustrates particle movement due only to Brownian motion. These simulations were run as part of the debugging

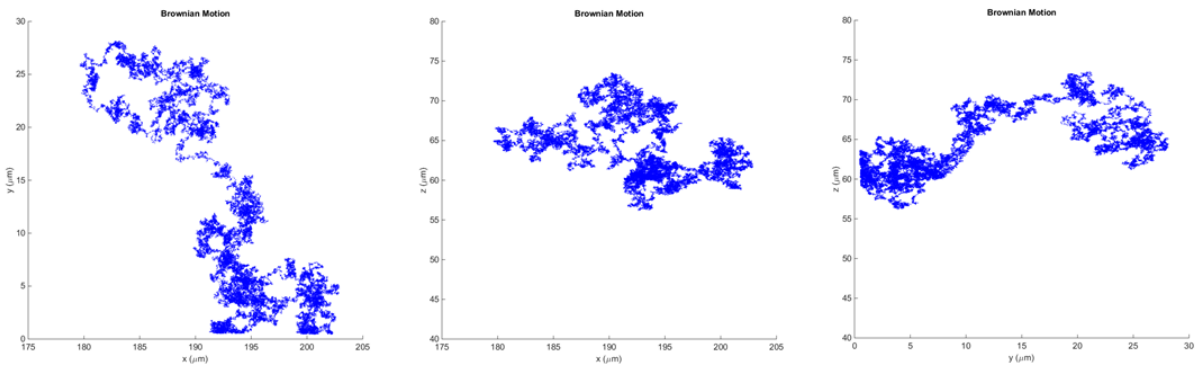

Figure 4.4: Displacement during 6.68 s due to Brownian motion only for a 30-nm particle at 293 K in water. Left: displacement in the xy-plane. Middle: displacement in the xz-plane. Right: displacement in the yz-plane

process and to ensure that the stochastic algorithm was producing diffusion consistent with continuum-scale behavior and length/time scales.

4.3.6.4 Particle Initial Conditions

The initial position of each particle is randomly distributed but with a flow-rate bias, which means that higher flow rate areas receive more particles than lower flow rate areas – as it occurs in experimental setups. The flow rate bias is implemented by comparing a random number between 0 and 1 and the normalized cumulative flow rate across the entry plane. The flow rate bias initial condition provides a more realistic initial condition than simply randomly distributed because the number of particles across the entrance plane relates to the flow pattern whereas simply randomly distributed does not.

For the various simulations in the micromodel domain, the particles were attributed the same initial positions. Thereby, when a parameter (e.g., flow rate or particle diameter) was changed, this single parameter was the only change and simulations could be directly compared. Although just one parameter was changed at time for most cases, it is important to note that there was still a random component due to Brownian motion. This procedure

of attributing the same initial position was also performed for the simulations in the Berea domain.

4.3.6.5 Rolling and Ray Tracing

Two procedures have been instituted to increase numerical efficiency that we will refer to as *rolling* and *ray tracing*. These are two similar procedures that help prevent numerical problems when the particle is very close to the surface (user-defined distance) and Δt is extremely small resulting $\Delta \mathbf{x}_p'' = \|\mathbf{x}_p'' - \mathbf{x}_p^n\| < \epsilon$. These procedures approximate the particle displacement by moving the particle to the next tetrahedron.

Rolling is performed only on neutral surfaces (no surface forces) and when the particle is within a user-defined distance from the wall. The particle moves towards the wall until it touches the wall and then travels parallel to the wall until it reaches the adjacent tetrahedron. The direction of the movement is determined by the tangential component of v_f. After rolling is performed, the regular scheme for time step advance is performed at least twice before rolling is allowed to be performed again.

Ray tracing is performed when $\Delta \mathbf{x}_p'' < \epsilon$ and the particle is within five times the user-defined distance from the wall. Ray tracing approximates particle displacement by moving the particle to the adjacent tetrahedron in the direction of the fluid velocity. This position is calculated by finding the intersection of the velocity vector and the tetrahedron using an algorithm from Moller and Trumbore (2005).

4.3.6.6 Surface Forces and Active Surfaces

When surface forces are turned on, it is possible to select – randomly or in a pattern – which surfaces are actually active (i.e., some surface may remain neutral). For the micromodel simulations, when surface forces were present, the top cover was still considered

neutral. For the Berea, when surface forces were on, all surfaces were active (except for XCT image-based mineralogy).

4.3.6.7 Particle Retention

A particle is considered attached to the wall when the surface forces are dominant compared to other forces. We have used the criterion

$$\frac{\mathbf{F}_{\text{surface}}}{\mathbf{F}_{\text{other}}} > 1000 \tag{4.17}$$

for when the particle is considered attached to the surface. However, the value of this ratio may need to be revisited in the future by comparing with experimental results.

4.3.6.8 Breakthrough Curves (BTCs)

In order to produce breakthrough curves, each particle is given a random entrance time during the injection process. After injection of NP solution, a solution without any particles is injected. The effluent time is given by the sum of the the random entrance time and the particle travel time.

Due to computational limitation, particles are tracked up to ten pore volumes (PV). When a particle is still traveling in the pore space (i.e., not attached) after 10 PV, it is given a different tag and simulation is stopped to proceed with the next particle.

The number of pore volumes injected is attributed during post processing. After consideration of two, three, four, and five pore volumes of injection, we decided to present results for 4-PV injection because the differences between curves were more distinguishable. In addition, using 4 PV resulted in a volume fraction $\alpha < 10^{-6}$ and, therefore, satisfied the one-way coupling condition.

4.3.6.9 Surface Capacity (S_{max})

Surface capacity (or site blocking) is introduced by limiting surface coverage by NPs. In other words, when $S_{max} = 0.10$, up to 10% of the surface may be covered by a monolayer to NPs such that there is no overlap between particles. The maximum monolayer coverage occurs in a hexagonal packing, covering ∼91% of the surface (Weisstein).

Surface capacity calculation consists of, first, calculating the surface area of each wall surface tetrahedron face (i.e. triangle). The nodes A, B, C of the tetrahedron face are known. Then, the area is given by

$$\text{Area} = \frac{|AB \times AC|}{2} \tag{4.18}$$

where AB is the vector from node A to node B. With a known surface area, the cross-sectional area projection of a NP, and a maximum surface coverage, then the maximum number of NPs per tetrahedron face can be calculated.

4.4 Results and Discussion

4.4.1 Micromodel

4.4.1.1 Sensitivity Analysis

A sensitivity analysis on the mesh resolution was performed to verify what mesh resolution was sufficient. Our in-house unstructured mesh generator allows variable refinement such that close to the surface the mesh is fine and away from the surface, in large pores, the mesh is coarse. In addition, it provides user-defined localized refinement. Initially, uniform refinement was used for the full domain (870×830×56 voxels or 2.00×1.91×0.13 mm^3). However, due to the large domain, variable refinement was soon necessary. In Figure

4.5, a., flow rate seems to converge at about 2 to 3.5 million elements. User-defined local refinement generated a mesh with 1.11 million elements that predicted a similar flow rate. To ensure convergence was achieved, a uniform refinement was performed in a smaller domain, 480×300×56 voxels or 1.10×0.69×0.13 mm^3, and compared with the parameters used in the 3.4 and 2.2 million element full domain meshes (Figure 4.5, b.), which supported that the flow rate had converged.

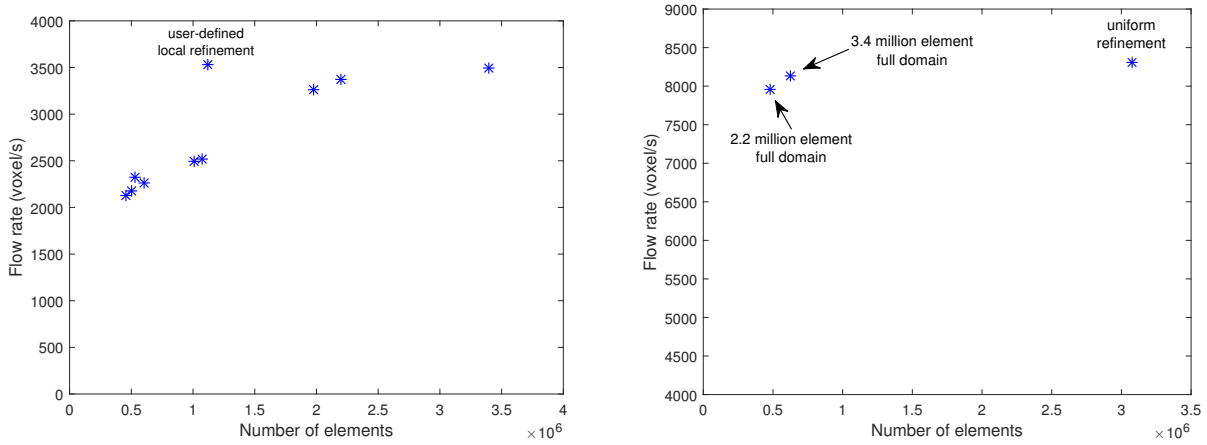

(a) Full domain, 870×830×56 voxels or 2.00×1.91×0.13 mm^3.

(b) Small domain, 480×300×56 voxels or 1.10×0.69×0.13 mm^3.

Figure 4.5: Mesh refinement sensitivity analysis: flow rate convergence.

Velocity profiles can provide more evidence that a sufficiently fine mesh has been achieved. Figure 4.6 shows the streamlines obtained by the FEM Stokes flow solver and the location where the velocity profiles of Figure 4.7 come from. According to the velocities profiles, it can be seen that when the number of elements is about two million or more, the velocities converge to the same curve. In addition, the mesh with user-defined local refinement shows good agreement except for V_z from ∼150 to 200 voxels.

Based on results from Figures 4.5 and 4.7, three domains – 1.1 (with user-defined local refinement), 2.2, and 3.4 million elements – were chosen to analyze particle deposition

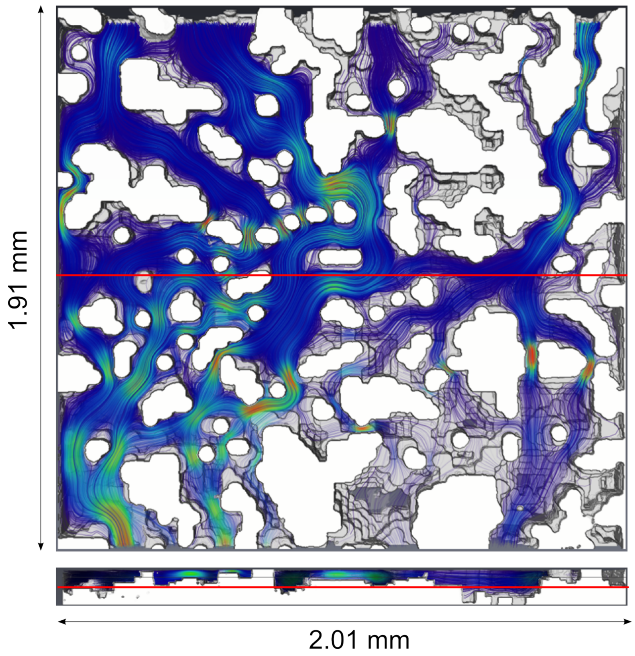

Figure 4.6: Streamlines obtained by the FEM Stokes flow solver. Top: top view superimposed on the micromodel XCT image. Bottom: cross-section at the red line indicated on the top view.

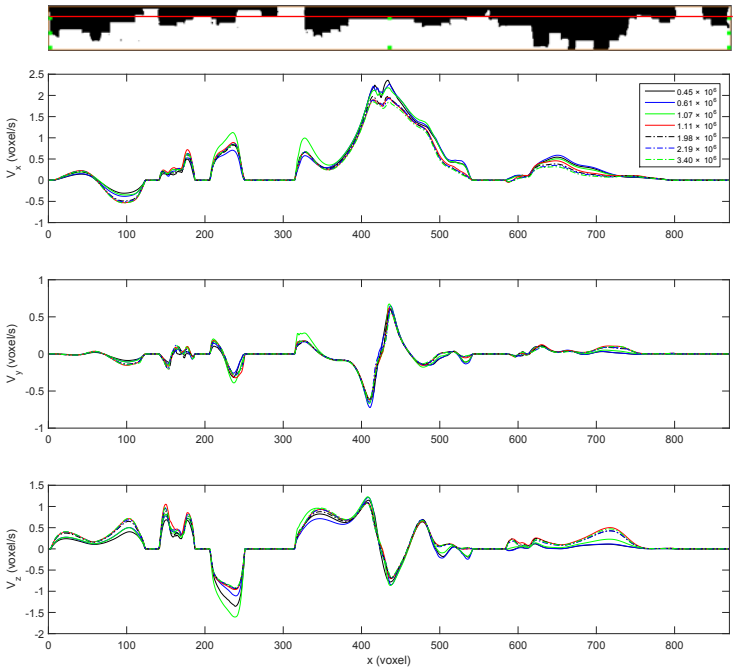

Figure 4.7: Velocity profiles at the locations shown in Figure 4.6. At the top, the cross-section where white represents the solid phase and black represents the pore space.

efficiency for three different particle diameters (d_p): 10, 50 and 300 nm (Figure 4.8). Due to the small differences in deposition efficiency between meshes with 2.2 and 3.4 million elements, the 2.2 million element mesh was chosen to be used in this study.

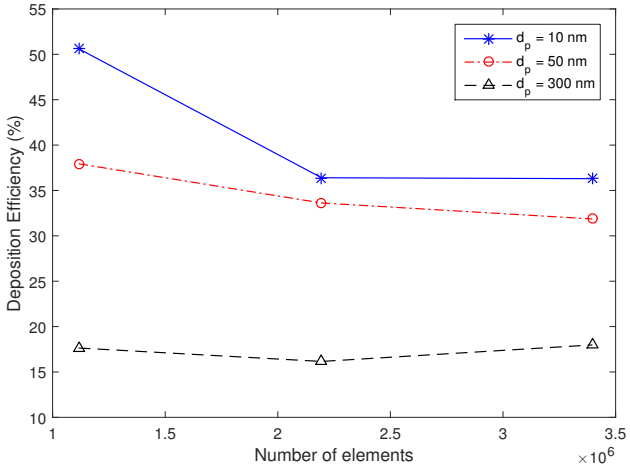

Figure 4.8: Particle deposition efficiency for different mesh refinements and particle diameters.

In addition to mesh refinement, it is also important to determine the sensitivity of deposition efficiency to the number of particles simulated. Figure 4.9 shows that as the number of particles increased, the variation in deposition efficiency decreased. Based on these results, all of the following simulations used 30k particles.

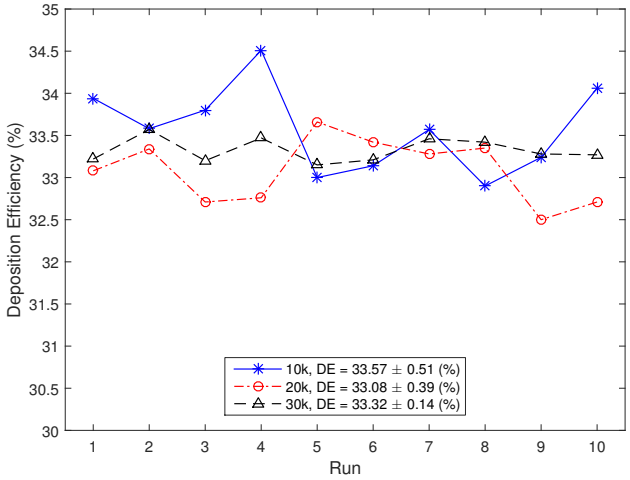

Figure 4.9: Variation of particle deposition efficiency for ten runs ($d_p = 50$ nm).

4.4.1.2 Particle Diameter Effect

Five different particle diameters (2, 10, 50, 100, and 300 nm) were simulated with the same flow rate (and surface forces turned off) to understand the effect of particle size on NP transport. Figure 4.10 shows that larger particles travel, on average, faster than smaller particles and exit earlier producing an earlier BTC and lower tail. Compared to larger particles, smaller particles were able to reach lower velocities in slower streamlines that were close to the surface. In addition, Brownian motion had a more pronounced effect for smaller particles.

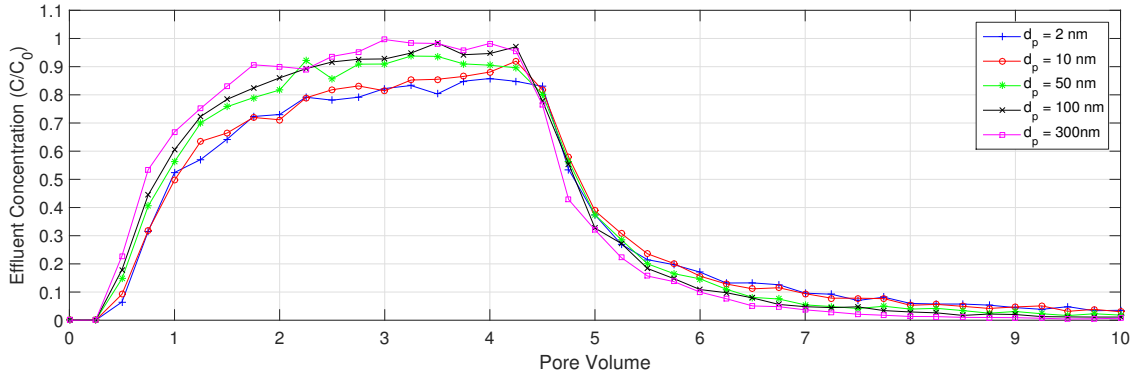

Figure 4.10: Breakthrough curves of various particle diameters without surface forces and constant flow rate.

Table 4.3 shows more evidence that smaller particles on average travel slower than larger particles. The percent recovered in 10 PV increased as particle diameter increased.

Table 4.3: Simulations with varying particle diameter (d_p) and other parameters fixed

d_p (nm)	Surface Forces	Reynolds Number	ρ_p (kg/m^3)	Recovered in 10 PV (%)	In the domain after 10 PV (%)	Attached (%)
2	-	3.10e-04	1000	93.46	6.54	0
10	-	3.10e-04	1000	95.34	4.66	0
50	-	3.10e-04	1000	98.35	1.65	0
100	-	3.10e-04	1000	99.26	0.74	0
300	-	3.10e-04	1000	99.82	0.18	0

However, when rolling and ray tracing (Section 4.3.6.5) were not active and Runge-Kutta was used near the surface, particle diameter seemed to have no effect on particle transport (Figure 4.11). It is clear that particle-surface interaction had an important role and the time that each particle spent close to the surface had impact on the overall particle transport. Further investigation (e.g., comparison with experimental results) is necessary to determine which algorithm is more accurate. It is important to note that when surface forces were present rolling and ray tracing did not occur – this effect was only seen when surface forces were neutral.

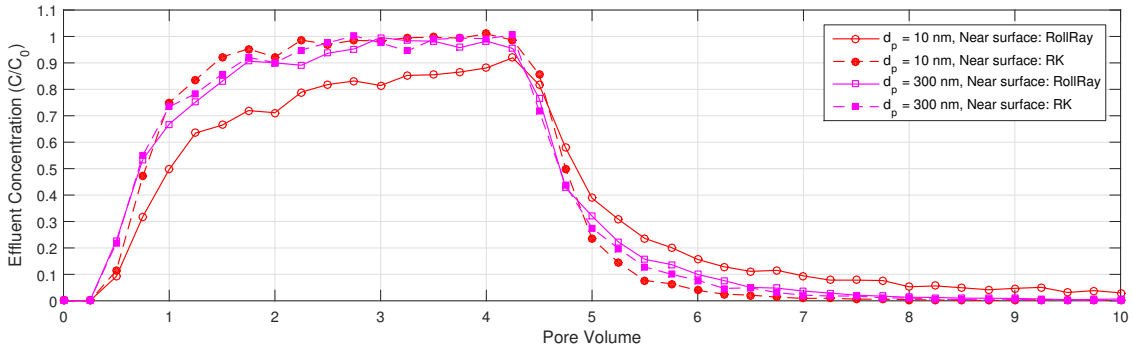

Figure 4.11: Breakthrough curves comparing different algorithms near the surface for $d_p = 10$ and 300 nm without surface forces and constant flow rate. RollRay: see Section 4.3.6.5, RK: Runge-Kutta (Section 4.3.6.1).

4.4.1.3 DLVOA – Attractive Surface Force Effect

In the presence of attractive surface forces (DLVOA, Figure 4.3, b., red curve), NP attachment decreased as particle diameter increased (Figure 4.12). The same trend was found by Nelson and Ginn (2005) when using modified colloid filtration theory in a Happel sphere and $10 \leq d_p \leq 626$ nm. Longest and Xi (2007), while investigating NP (ultra fine aerosol) deposition in the upper airways using an EL methodology that neglects particle inertia, also found a decreasing trend in DE as particle diameter increased from 1 to 120 nm. Li et al. (2012) investigated NP transport using LBM and LPT in a pack of glass beads that

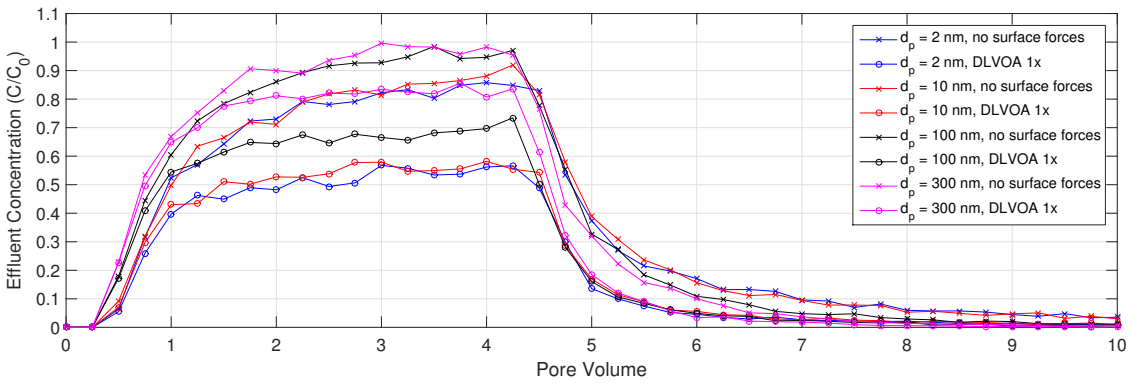

Figure 4.12: Breakthrough curves of four particle diameters (2, 10, 100, and 300 nm) when attractive surface forces (DLVOA, Figure 4.3, b., red curve) are present. DLVOA: attractive surface force.

was imaged using XCT and found a decrease in particle deposition for $100 \leq d_p \leq 500$ nm for constant flow rate within Darcy regime.

It is reasonable to argue that smaller particles are able to reach slower streamlines close to the wall and thus, have a higher chance of depositing on the surface. In addition, smaller particles are more subject to Brownian motion which could cause movement towards the wall. Evidence of these behaviors can be found when comparing no surface forces *vs.* DLVOA: larger particles recovery was less affected by DLVOA (Table 4.4). For example, when $d_p =$ 2 nm, recoveries in 10 PV were 93.46% and 53.38% for no surface forces and DLVOA, respectively, whereas when $d_p = 300$ nm the recoveries were 99.82% and 84.11%.

In order to understand the effect of surface force strength, the magnitude of attractive surface forces (DLVOA) was increased and/or decreased by two orders of magnitude for $d_p = 10$ and 100 nm. Figure 4.13 shows that, for 10-nm particles, the increased (DLVOA 100×) surface forces did not increase particle retention nor modify the BTC pattern. The lack of a difference between DLVOA 1× and 100× indicated that the DLVOA 1× was strong enough to retain all the particles that approached the surface. The DLVOA 0.01× results

Table 4.4: Simulations with attractive surface forces with other parameters fixed for four particle diameters. DLVOA: attractive surface force; DLVOA 100×: attractive surface force × 100.

d_p (nm)	Surface Forces	Reynolds Number	ρ_p (kg/m^3)	Recovered in 10 PV (%)	In the domain after 10 PV (%)	Attached (%)
2	-	3.10e-04	1000	93.46	6.54	0
2	DLVOA	3.10e-04	1000	53.38	2.74	40.88
10	-	3.10e-04	1000	95.34	4.66	0
10	DLVOA	3.10e-04	1000	59.56	1.96	38.48
10	DLVOA 0.01×	3.10e-04	1000	77.59	2.20	20.21
10	DLVOA 100×	3.10e-04	1000	59.64	2.01	38.35
100	-	3.10e-04	1000	99.26	0.74	0
100	DLVOA	3.10e-04	1000	70.40	0.42	29.18
100	DLVOA 100×	3.10e-04	1000	67.25	0.39	32.36
300	-	3.10e-04	1000	99.82	0.18	0
300	DLVOA	3.10e-04	1000	84.11	0.08	15.81

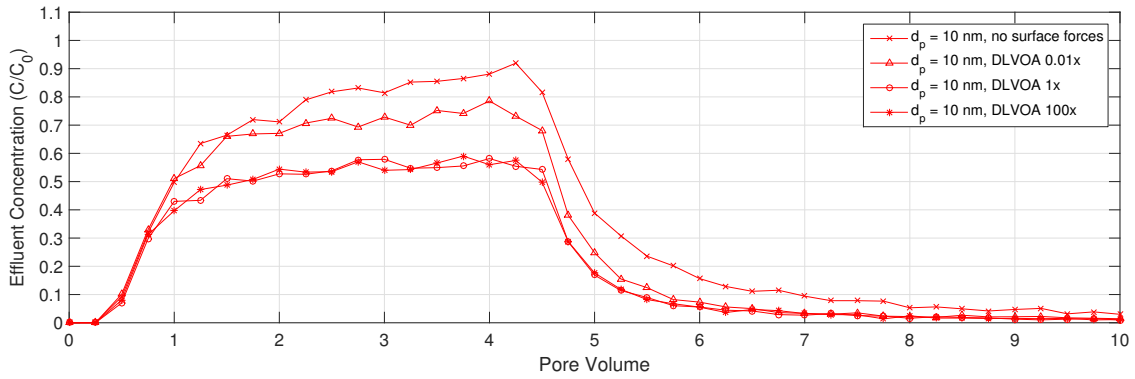

Figure 4.13: Breakthrough curves of 10-nm particles when attractive surface forces (DLVOA) of various strengths are present.

also support this argument: decreasing the strength of attractive surface forces yielded less particle retention and a BTC profile that sits between no surface forces and DLVOA 1×. These behaviors also showed that the competing hydrodynamic and surface forces were an important factor for particle retention. Figure 4.14 shows the effect of increasing attractive surface forces (DLVOA) by a factor of 100 when $d_p = 100$ nm. For this larger particle, there

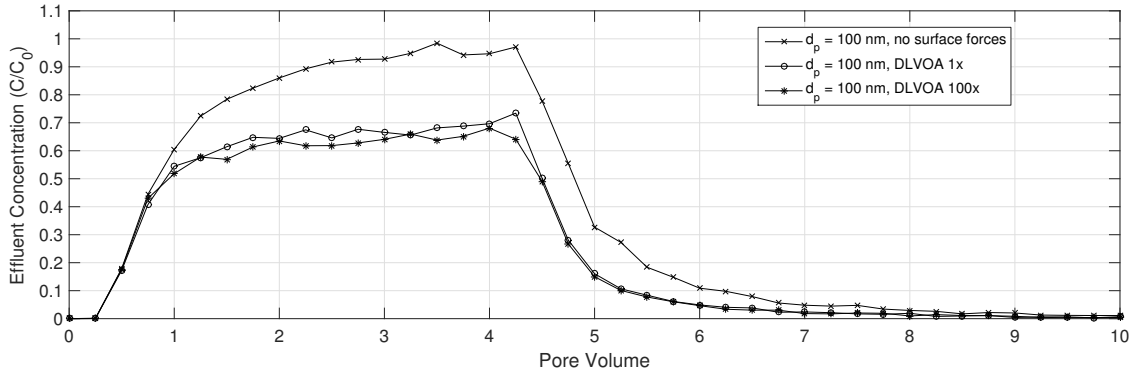

Figure 4.14: Breakthrough curves of 100-nm particles when attractive surface forces (DLVOA) of two different strengths are present.

was a slight increase of particle retention, from 29.18% to 32.36% (Table 4.4) which can also be seen by the higher plateau of the BTC (Figure 4.14).

4.4.1.4 DLVOB – Repulsive Surface Force Effect

The effect of repulsive surface forces (DLVOB, Figure 4.3, b., blue curve) was investigated for 10 and 100-nm particles. Figure 4.15 and Table 4.5 show a small increase in particle recovery for 10-nm particles in the presence of repulsive surface forces. In addition,

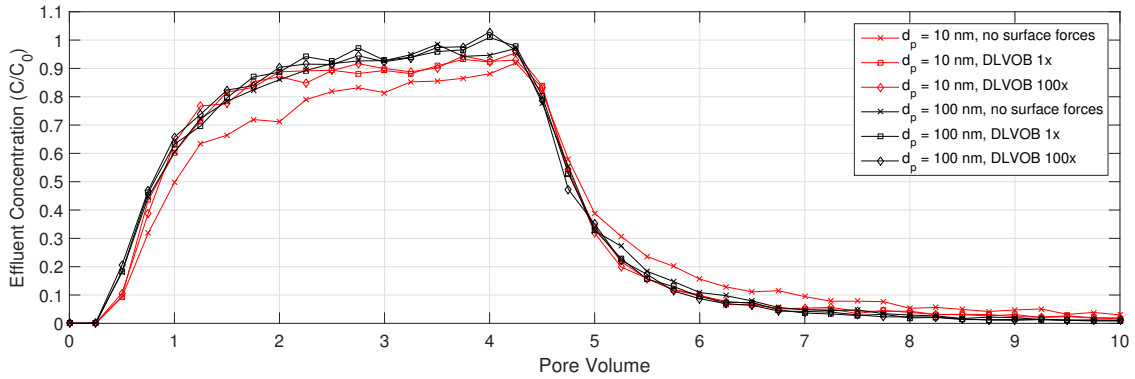

Figure 4.15: Breakthrough curves of two particle diameters (10 and 100 nm) when repulsive surface forces (DLVOB, Figure 4.3, b., blue curve) are present. DLVOB: repulsive surface force; DLVOB 100×: repulsive surface force × 100

DLVOB BTCs showed a higher shoulder and lower tail when compared with no surface forces. These findings suggest that repulsive surface forces prevented particles from moving to slower streamlines closer to the surface and exiting the domain earlier. This is also

Table 4.5: Simulations with repulsive surface forces with other parameters fixed for two particle diameters. DLVOB: repulsive surface force; DLVOB 100×: repulsive surface force × 100.

d_p (nm)	Surface Forces	Reynolds Number	ρ_p (kg/m^3)	Recovered in 10 PV (%)	In the domain after 10 PV (%)	Attached (%)
10	-	3.10e-04	1000	95.34	4.66	0
10	DLVOB	3.10e-04	1000	97.30	2.70	0
10	DLVOB 100×	3.10e-04	1000	97.28	2.72	0
100	-	3.10e-04	1000	99.26	0.74	0
100	DLVOB	3.10e-04	1000	99.48	0.52	0
100	DLVOB 100×	3.10e-04	1000	99.43	0.57	0

supported when comparing 10 *vs.* 100-nm particles: particles with $d_p = 10$ nm could get closer to the wall in slower streamlines than 100-nm particles. With repulsive surface forces acting, these particles were moved away from the wall into faster streamlines and causing the 10-nm BTC shoulder to move up more than the 100-nm BTC shoulder, relative to the non-repulsive base cases.

There was not a considerable difference for 100-nm particles when comparing no surface forces and repulsive surface forces (DLVOB), indicating that larger particles travel on faster streamlines away from the surface. Thus, the presence of repulsive surface forces did not have a considerable impact on 100-nm particles.

A stronger repulsive force was simulated for $d_p = 10$ and 100 nm to investigate the effect of surface force strength. Figure 4.15 and Table 4.5 show no apparent changes when the strength of repulsive surface forces were 100× stronger, which indicates that the DLVOB 1× was strong enough to repel all of the particles that got close to the surface.

An interesting finding by Li et al. (2012) for particle transport under unfavorable conditions (i.e., repulsive surface forces) was that the number of particles still in the domain

after 7 PV increased as repulsive surface forces increased. Our results for $d_p = 10$ nm (Tables 4.4 and 4.5) also show this trend: more particles were still traveling in the domain after 10 PV in presence of repulsive surface forces (DLVOB) than in the presence of attractive surface forces (DLVOA), 2.70% *vs.* 1.96%, respectively.

4.4.1.5 Flow Rate Effect

In the presence of attractive surface forces (DLVOA), the increase in flow rate caused a higher particle recovery (Figures 4.16, 4.17, Table 4.6), a trend also found by Li et al. (2012) when flow rate was increased from 1.71×10^{-5} to 3.42×10^{-5} m/s for $100 \leq d_p \leq 500$ nm. Longest and Xi (2007) also showed a decrease in particle deposition with increased flow rate from 15 to 60L/min and fixed particle size.

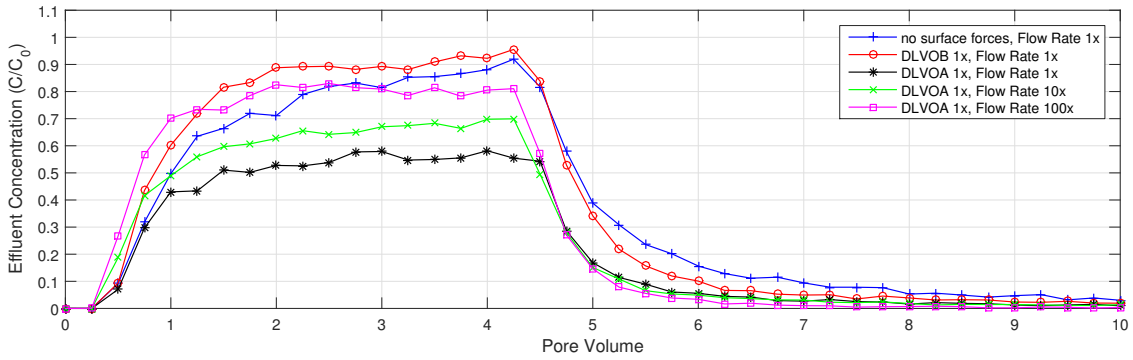

Figure 4.16: Breakthrough curves when attractive (DLVOA) or repulsive (DLVOB) surface forces are present with varying flow rate and $d_p = 10$ nm.

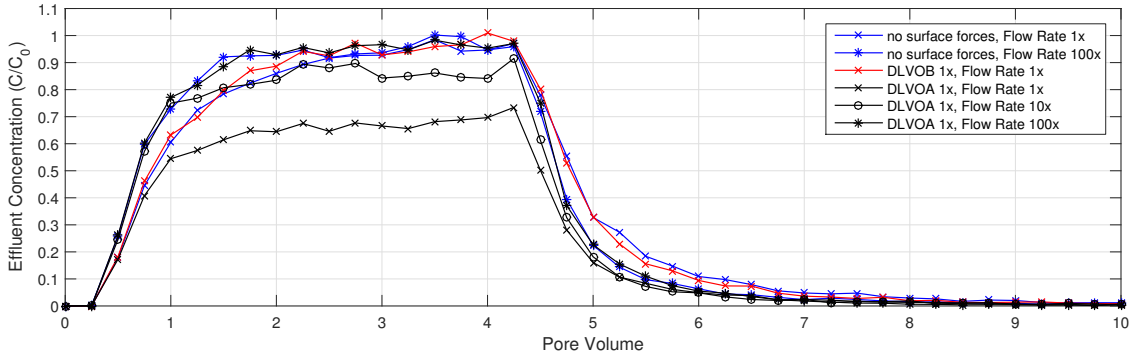

Figure 4.17: Breakthrough curves when attractive (DLVOA) or repulsive (DLVOB) surface forces are present with varying flow rate and $d_p = 100$ nm.

Table 4.6: Simulations with different Reynolds number (i.e., flow rates) with other parameters fixed for two particle diameters. DLVOA: attractive surface force; DLVOA 100×: attractive surface force × 100; DLVOB: repulsive surface force; DLVOB 100×: repulsive surface force × 100.

d_p (nm)	Surface Forces	Reynolds Number	ρ_p (kg/m^3)	Recovered in 10 PV (%)	In the domain after 10 PV (%)	Attached (%)
10	-	3.10e-04	1000	95.34	4.66	0
10	DLVOB	3.10e-04	1000	97.30	2.70	0
10	DLVOA	3.10e-04	1000	59.56	1.96	38.48
10	DLVOA	3.10e-03	1000	69.50	1.91	28.59
10	DLVOA	3.10e-02	1000	82.66	1.59	15.76
100	-	3.10e-04	1000	99.26	0.74	0
100	DLVOB	3.10e-04	1000	99.48	0.52	0
100	DLVOA	3.10e-04	1000	70.40	0.42	29.18
100	DLVOA	3.10e-03	1000	89.40	0.65	9.96
100	DLVOA	3.10e-02	1000	98.82	0.33	0.84

In addition, Table 4.6 shows that the effect of flow was more prominent for 100-nm particle than for 10-nm particles. Longest and Xi (2007), however, found the opposite trend: when flow rate was increased from 15 to 60 L/min, it smaller particles more than bigger particles for the particle size range $1 \leq d_p \leq 120$ nm and.

An interesting observation in Figure 4.16 is the earlier BTC when flow rate is 100× higher and d_p is constant. This behavior was also found by Zhang (2012) experimentally and numerically (using modified colloid filtration theory with two-site model) when flow rate increased from 1 to 10 mL/min for two salt tolerant silica particles ($d_p = 15$ nm) and iron-oxide particles ($d_p = 150$ nm). He et al. (2009) found a similar trend of earlier BTCs experimentally and when simulating carboxymethyl cellulose stabilized iron nanoparticles in porous media and flow velocity increased from 0.0176 to 0.0706 cm/s.

This earlier BTC for higher flow rate could either be the effect of surface forces or Brownian motion. Surface forces could delay smaller particles more than it delays

bigger particles. Brownian motion, in turn, could play a bigger role when the competing hydrodynamic forces are lower and thus delaying the effluent concentration more when flow rates are lower.

To verify the main factor causing an earlier BTC for higher flow rates, first, we turned off surface forces and compared BTCs. Figure 4.18 shows that even without surface forces, the high flow rate presented an earlier BTC than the low flow rate.

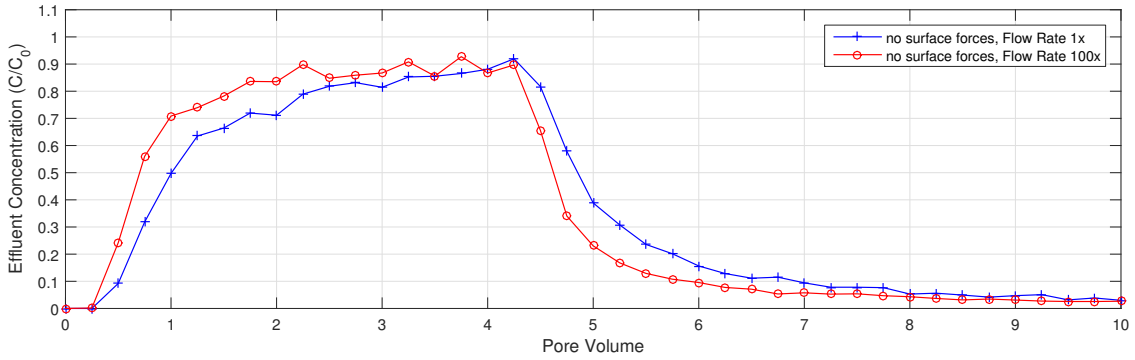

Figure 4.18: Breakthrough curves with no surface forces, varying flow rate, and $d_p = 10$ nm.

Second, Brownian motion was turned off (i.e., streamline tracking). Figure 4.19 confirmed that Brownian motion caused particles to delay exiting from the domain. From Figures 4.16 and 4.17, it is also evident that the delay of BTC due to Brownian motion was more important for $d_p = 10$ nm than $d_p = 100$ nm.

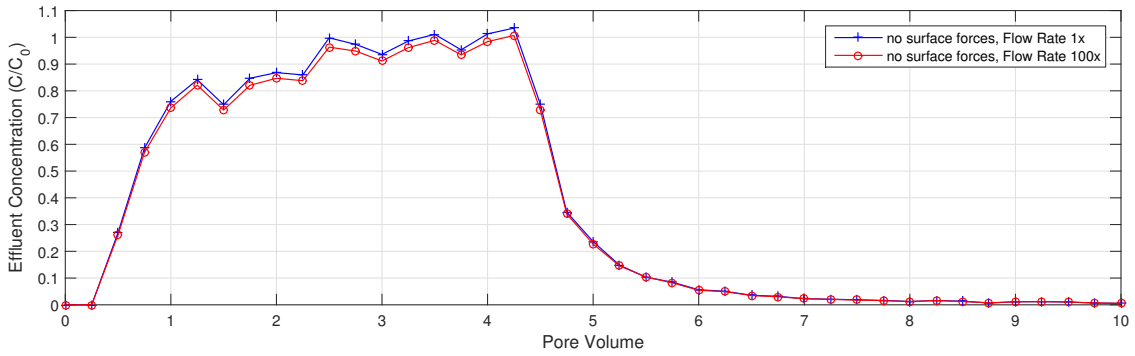

Figure 4.19: Breakthrough curves with Brownian motion turned off (i.e., streamline tracking), no surface forces, varying flow rate and $d_p = 10$ nm.

4.4.1.6 Particle Density Effect

In order to understand the effect of particle density in effluent concentrations, silver and "air" NPs ($\rho_p = 10490$ and $\rho_p = 1.3$ kg/m^3, respectively) were simulated. Note that although NPs have "air" density, they behave as solid particles with a very low density.

Figures 4.20 and 4.21 and Table 4.7 show no apparent difference in the effluent concentration and particle deposition for the different densities. One could argue that NPs have such small mass (in the order of 10^{-25}-10^{-21} kg) that the difference in particle density is negligible.

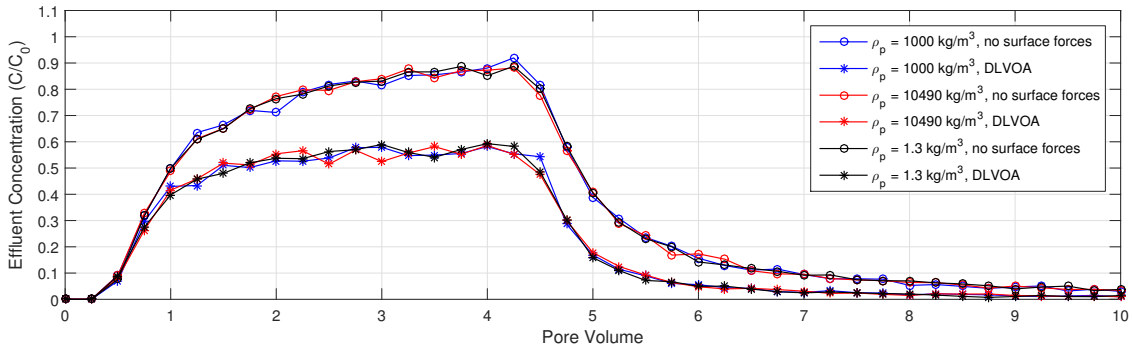

Figure 4.20: Breakthrough curves with varying particle density, surface forces on (DLVOA) or off, and $d_p = 10$ nm.

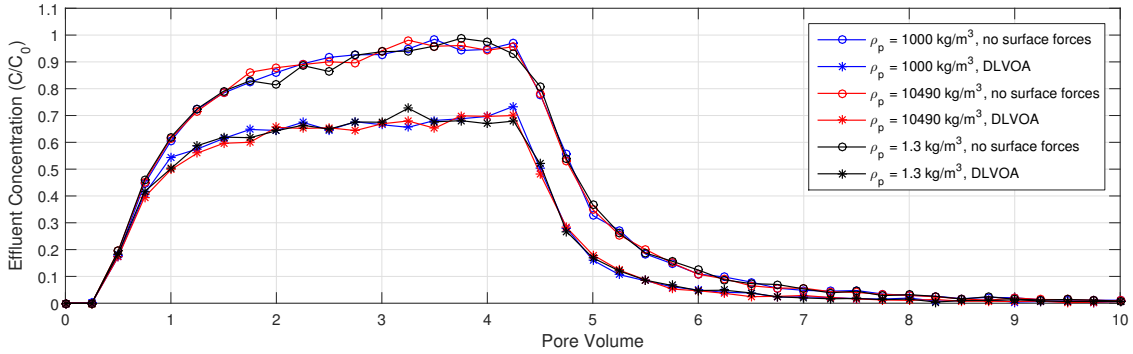

Figure 4.21: Breakthrough curves with varying particle density, surface forces on (DLVOA) or off, and $d_p = 100$ nm.

Table 4.7: Simulations with different particle density (ρ_p = 1000, 10490, 1.3 kg/m^3, water, silver, and air, respectively) with other parameters fixed for two particle diameters. DLVOA: attractive surface force.

d_p (nm)	Surface Forces	Reynolds Number	ρ_p (kg/m^3)	Recovered in 10 PV (%)	In the domain after 10 PV (%)	Attached (%)
10	-	3.10e-04	1000	95.34	4.66	0
10	DLVOA	3.10e-04	1000	59.56	1.96	38.48
10	-	3.10e-04	10490	95.23	4.77	0
10	DLVOA	3.10e-04	10490	59.50	1.97	38.53
10	-	3.10e-04	1.3	95.38	4.62	0
10	DLVOA	3.10e-04	1.3	59.50	1.89	38.62
100	-	3.10e-04	1000	99.26	0.74	0
100	DLVOA	3.10e-04	1000	70.40	0.42	29.18
100	-	3.10e-04	10490	99.38	0.38	0
100	DLVOA	3.10e-04	10490	69.05	0.23	30.72
100	-	3.10e-04	1.3	99.38	0.62	0
100	DLVOA	3.10e-04	1.3	70.25	0.46	29.29

4.4.1.7 Surface Capacity Effect

Two different surface capacities, S_{max} = 10% and 1%, were tested for d_p = 300 nm. Figure 4.22 shows that when S_{max} = 10%, there was no apparent difference in the BTCs. When, S_{max} = 1%, the shoulder was slightly higher but the maximum value of C/C_0 was the same as when S_{max} = 10% and when attachment was unlimited. Table 4.8 also shows a smaller percentage of attached particles, 14.59%, than when there was unlimited attachment, 15.81%. The differences between the three BTCs (Figure 4.22) and percent attached (Table 4.8) were small and it would be more appropriate (in a future investigation) to perform multiple simulations to ensure that the differences were statistically significant.

4.4.2 Berea

Preliminary simulations on a XCT image of Berea sandstone were performed to demonstrate that the nanoparticle transport model presented in this work can be used in

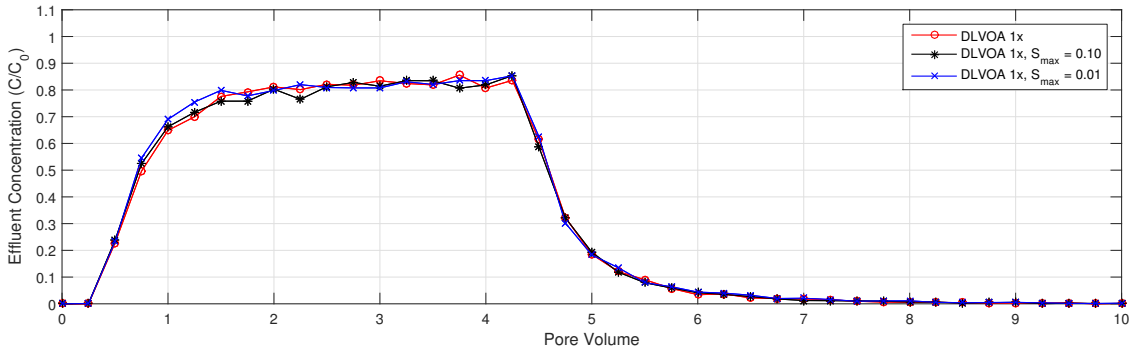

Figure 4.22: Breakthrough curves with attractive surface forces (DLVOA) on and varying surface capacity (S_{max}) for $d_p = 300$ nm.

Table 4.8: Simulations with different surface capacities (S_{max}) with other parameters fixed for $d_p = 300$ nm. DLVOA: attractive surface force.

d_p (nm)	Surface Forces	Reynolds Number	ρ_p (kg/m^3)	S_{max}	Recovered in 10 PV (%)	In the domain after 10 PV (%)	Attached (%)
300	DLVOA	3.10e-04	1000	-	84.11	0.08	15.81
300	DLVOA	3.10e-04	1000	0.10	83.71	0.09	16.20
300	DLVOA	3.10e-04	1000	0.01	85.33	0.08	14.59

real rocks to study NP fate and transport in very complex geometries. A detailed sensitivity analysis was not completed because the purpose is to show the potential of the code developed in this work. Nonetheless, streamlines were plotted against the XCT image (Figure 4.23) and showed good agreement for the purpose of these simulations.

4.4.2.1 Particle Diameter Effect

The effect of particle size in the Berea was similar to the micromodel. As particle size increased, particles traveled through the domain faster and exited the domain earlier. Thus, larger particles had earlier BTCs with higher shoulders and lower tails (Figure 4.24).

The same rationale from the micromodel applies to the Berea: smaller particles traveled on slower streamlines close to the surface and had a higher chance to move to these slower streamlines because they were more susceptible to Brownian motion. Larger particles, on

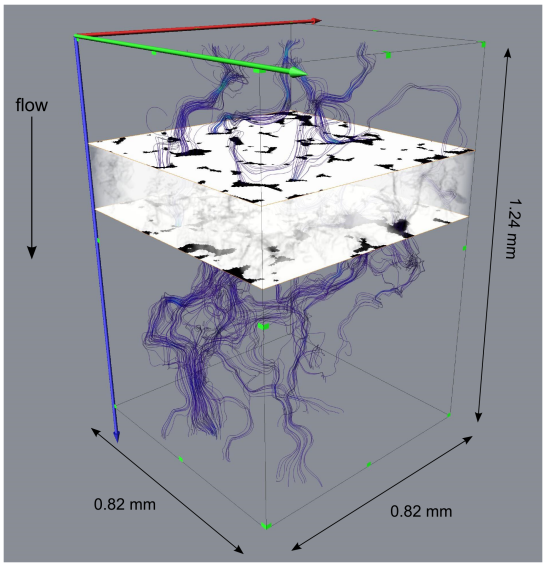

Figure 4.23: Cross section of Berea XCT image and streamlines obtained from FEM simulation.

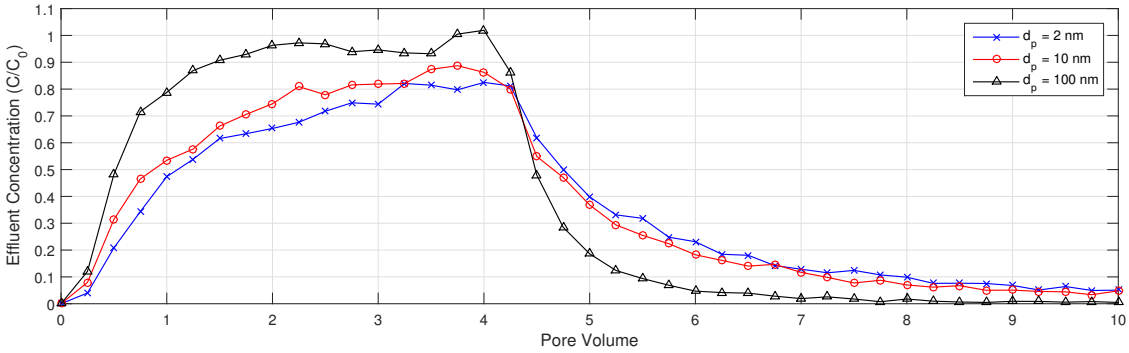

Figure 4.24: Breakthrough curves with no surface forces for varying particle diameters.

the other hand, traveled on faster streamlines away from the surface and were less subject to Brownian motion. Table 4.9 shows that the percent recovered within 10 PV increased with particle diameter. In addition, the percent still in the domain after 10 PV decreased by about a half when d_p doubled from 2 to 10 nm. However, it decreased by an order of magnitude (from 3.64% to 0.47%) when d_p increased by a factor of 10. This finding provided more evidence of the relationship between particle size and particle recovery.

Table 4.9: Berea simulations with varying particle diameter (d_p) and other parameters fixed

d_p (nm)	Surface Forces	Reynolds Number	ρ_p (kg/m^3)	Recovered in 10 PV (%)	In the domain after 10 PV (%)	Attached (%)
2	-	3.37e-04	1000	93.80	6.20	0
10	-	3.37e-04	1000	96.36	3.64	0
100	-	3.37e-04	1000	99.53	0.47	0

The retardation effect on smaller particles seemed to be greater for NPs in the Berea than in the micromodel. For the micromodel, the BTCs for d_p =2, 10, and 100 nm (Figure 4.10) generally have the same shape, with small changes in the shoulder and tail. For the Berea (Figure 4.24), when $d_p = 2$ and 10 nm, the BTCs were similar, but when $d_p = 100$ nm, the shoulder is much higher and the tail much lower. This difference between micromodel and Berea was reasonable because the pores and throats in the Berea are a lot smaller than the ones in the micromodel. Therefore, smaller particles in the Berea have a higher chance of traveling on slow streamlines than in the micromodel.

Figure 4.25 shows that this difference between particle diameters was not seen when rolling and ray tracing (Section 4.3.6.5) were not active and Runge-Kutta (Section 4.3.6.1) was used near the surface. As seen with the micromodel simulations (Section 4.4.1.2), the time spent close to the surface had impact on the overall particle transport. Further investigation is necessary to determine which algorithm is more accurate.

4.4.2.2 Surface Forces Effects

Attractive (DLVOA), repulsive (DLVOB), and neutral (no surface forces) surface forces were simulated for $d_p = 10$ nm to understand their impact on NP transport. Figure 4.26 shows that repulsive surface forces aided NP transport through the Berea, similarly to effect

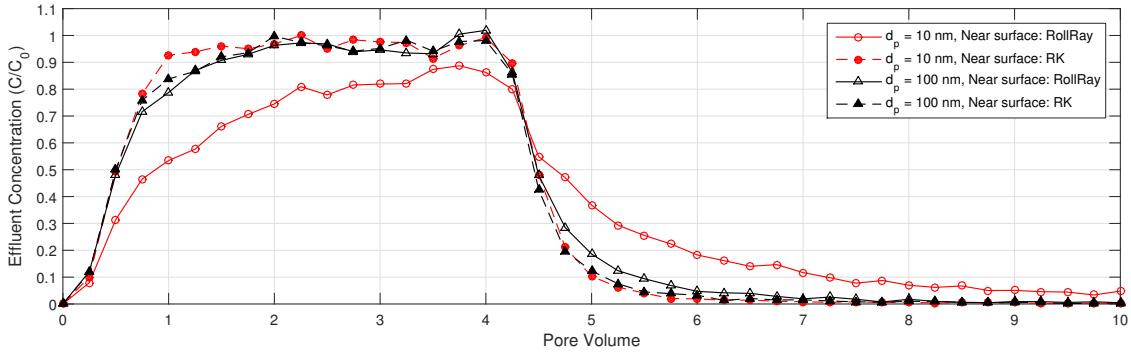

Figure 4.25: Breakthrough curves comparing different algorithms near the surface for $d_p = 10$ and 100 nm without surface forces and constant flow rate. RollRay: see Section 4.3.6.5, RK: Runge-Kutta (Section 4.3.6.1).

seen in the micromodel. With the repulsive surface forces, particles were kept away from the surface. Thus, they traveled on faster streamlines and exited earlier.

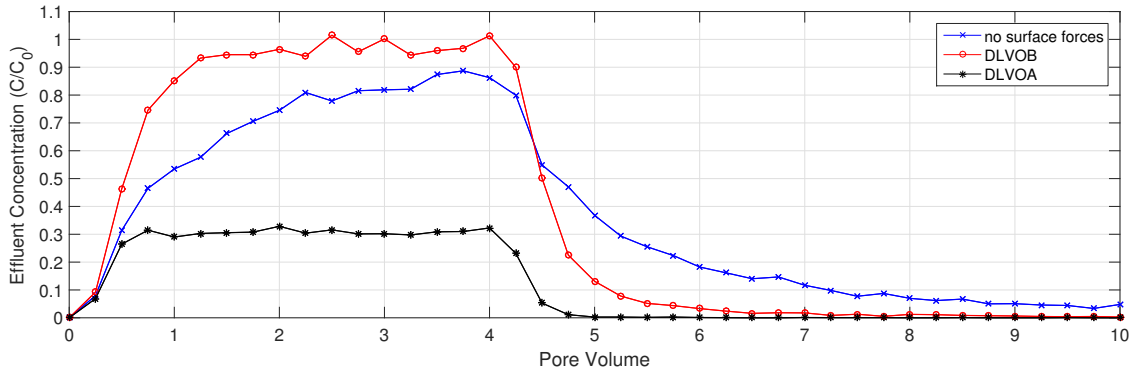

Figure 4.26: Breakthrough curves with varying surface forces and fixed particle diameter ($d_p = 10$ nm). DLVOA: attractive surface force; DLVOB: repulsive surface force.

Attractive surface forces (DLVOA) greatly reduced particle recovery, from ~96% to 31%, as shown in Table 4.10. The effect of attractive surface forces in the Berea was greater than in the micromodel (Tables 4.4 and 4.10). As mentioned above in Section 4.4.2.1, the Berea has smaller pores and throats than the micromodel and therefore, NPs were more likely to attach to the surface in the Berea.

The different BTC shapes between neutral and DLVOA/B in Figure 4.26 was caused by the time the particles spend near the surface. The same behavior was evident when

Table 4.10: Berea simulations with different surface forces and other parameters fixed for $d_p = 10$ nm. DLVOA: attractive surface force; DLVOB: repulsive surface force.

d_p (nm)	Surface Forces	Reynolds Number	ρ_p (kg/m^3)	Recovered in 10 PV (%)	In the domain after 10 PV (%)	Attached (%)
10	-	3.37e-04	1000	96.36	3.64	0
10	DLVOB	3.37e-04	1000	99.35	0.65	0
10	DLVOA	3.37e-04	1000	30.99	0.13	68.89

comparing the different algorithms used when a particle was near the surface (Figure 4.25). When surface forces were neutral (i.e., no surface forces), particles could travel near the surface until they eventually exited the domain. When attractive surface forces (DLVOA) were present and dominant, particles that approached a surface attached to it. And when repulsive surface forces (DLVOB) were present, particles that were near surface were pushed away from it. Due to the DLVOA/B surface forces, particles could not travel close to the surface, which was the main mechanism that caused the delayed BTC with a low shoulder and long tail for neutral surface forces.

4.4.2.3 XCT Image-Based Mineralogy

Previous simulations in the Berea using DLVO forces meant that all wall surfaces were active – as opposed to neutral. Thus, particles were subject to surface forces when close to any wall surface. With XCT image-based mineralogy, clay represented only 2% of wall surfaces which were defined as active. The remaining 98% of wall surfaces, mostly quartz/feldspar were neutral. Although only representing a small percentage, 2%, XCT image-based clay had a relevant impact on particle attachment, retaining 10.25% of the particles. Figure 4.27 shows how the shape of the BTC considerably changed: a much higher shoulder and lower tail than when surface forces were off. A simulation with 2% active surfaces randomly

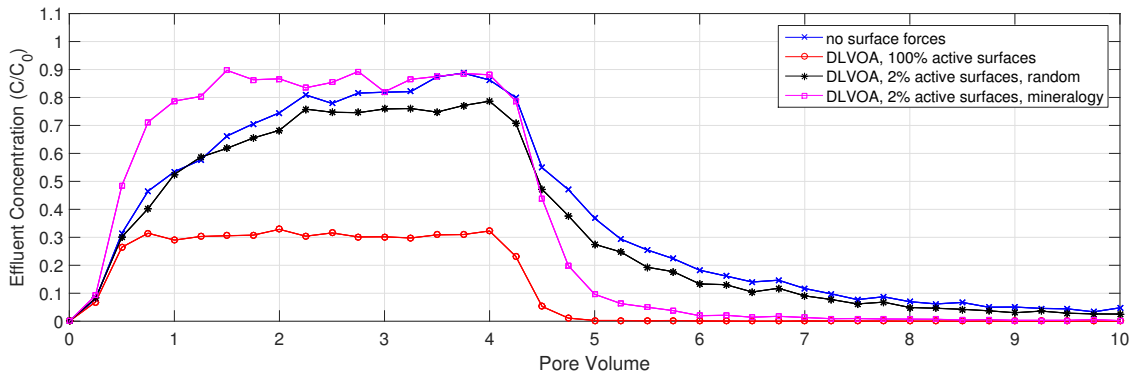

Figure 4.27: Breakthrough curves with attractive surface forces (DLVOA), different distribution of surface forces when $d_p = 10$ nm.

distributed was performed to confirm that XCT image-based mineralogy was the cause of such drastic change – rather than the decrease of active surfaces. Indeed, the simulation (Figure 4.27 and Table 4.11) showed that the location of the clay was very important in the way particles were retained.

Table 4.11: Berea simulations with and without attractive surface forces(DLVOA). Surface forces were randomly distributed or based on XCT mineralogy. Other parameters were fixed: Reynolds number = 3.37e-04, $\rho_p = 1000$ kg/m^3, $d_p = 10$ nm. SF: surface forces.

d_p (nm)	Active Surfaces (%)	Surface Forces	Distribution of SF	Recovered in 10 PV (%)	In the domain after 10 PV (%)	Attached (%)
10	-	-	-	96.36	3.64	0
10	100	DLVOA	-	30.99	0.13	68.89
10	2	DLVOA	Mineralogy	89.14	0.62	10.25
10	2	DLVOA	Random	85.36	2.77	11.87

Interestingly, the shape of the XCT image-based clay BTC (Figure 4.27) was very similar to the DLVOB (Figure 4.26). They breakthrough approximately at the same time and the tails were very similar. The plateau, however, reached the maximum $C/C_0 = 1$ for DLVOB, but was $\sim$0.9 for XCT image-based clay. The role of repulsive surface forces everywhere (Figure 4.26) seemed to be similar to having a few spots of particle retention determined by

XCT imaging. This leads us to think that certain zones in the Berea had a great impact on the overall particle retention.

Figure 4.28 shows the streamlines through the Berea and where particles attached. For the 2% active forces randomly distributed, red particles attached through the entire domain. On the other hand, for the 2% active forces determined by XCT, green particles attached in clusters where the clay was located.

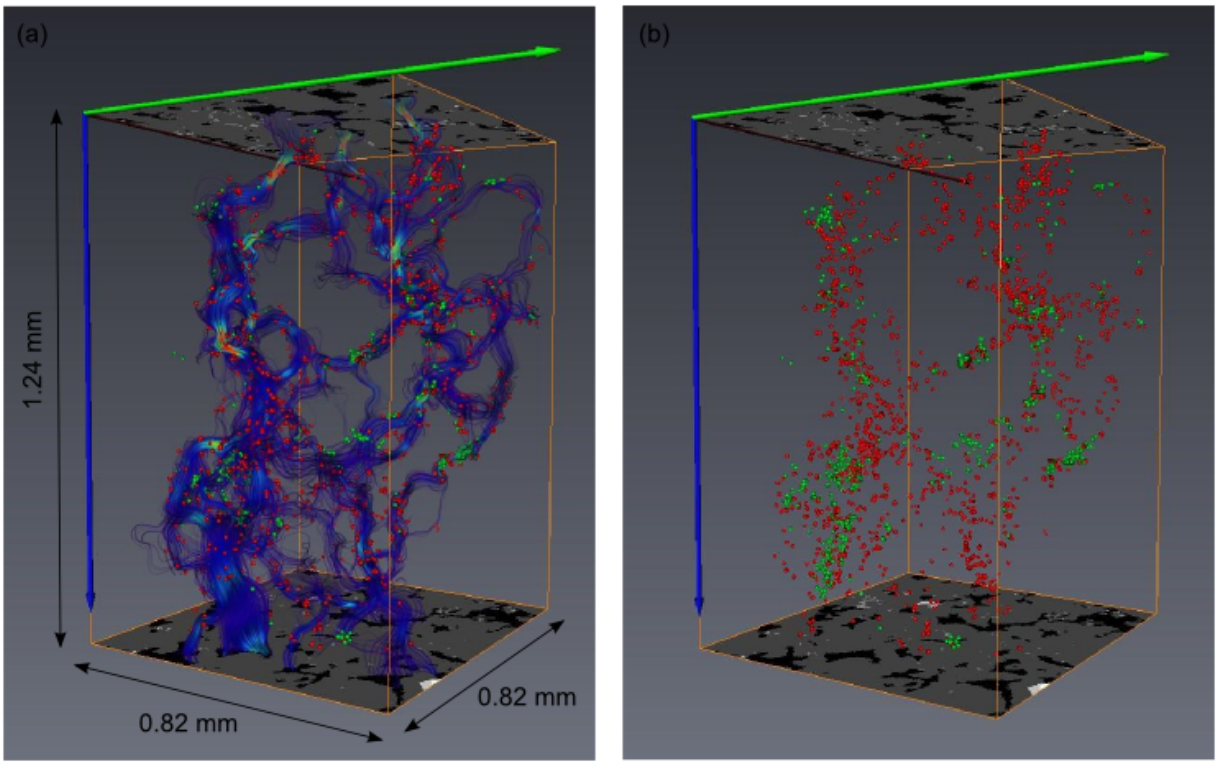

Figure 4.28: Locations of attached particles for 2% active forces randomly distributed (red) and XCT image-based mineralogy (green). (a) Stremlines and particles; (b) particles only. Flow simulated from top to bottom.

The match between XCT image-based mineralogy and particle attachment can be visualized in Figure 4.29. The blue particles (XCT image-based mineralogy active surface forces) laid on top of the clay (light gray) whereas red particles did not.

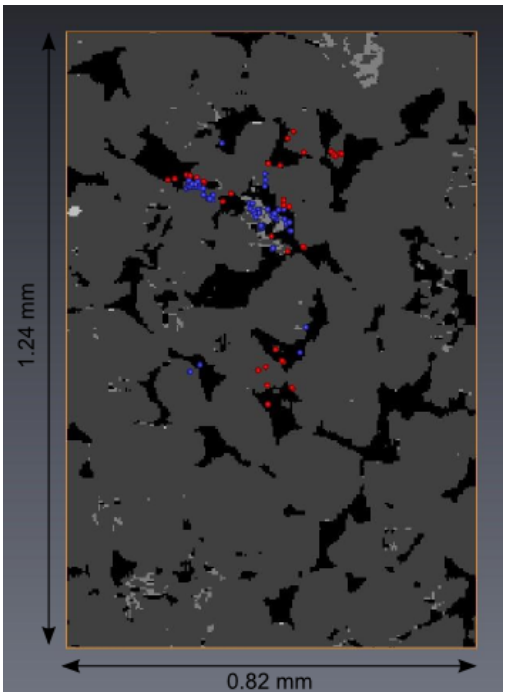

Figure 4.29: Locations of attached particles for 2% active forces randomly distributed (red) and XCT image-based mineralogy (blue) superimposed with XCT slice. In the XCT slice the clay is represented by light gray. Void is black and quartz is dark grey. Note that the attached particles correspond to particles within a thickness perpendicular to the page whereas the XCT slice is a single cross-section.

4.5 Surface Capacity Effect

Surface capacity (site blocking) was also analyzed in the Berea. Figure 4.30 shows that the overall behavior of particle transport remained fairly similar from unlimited capacity to S_{max} = 7e-6: particles breakthrough and exit approximately at the same times. However, the percent attached decreased from ∼69% to ∼64% (Table 4.12) when DLVOA surface forces were present in 100% of the surfaces.

Surface capacity was also simulated for 2% active surface forces determined by XCT mineralogy. Again, a similar trend of BTCs were found between unlimited capacity and S_{max} = 7e-6. However, the plateau was higher for the latter, indicating less particle retention (10.25% and 5.27%, respectively – Table 4.12).

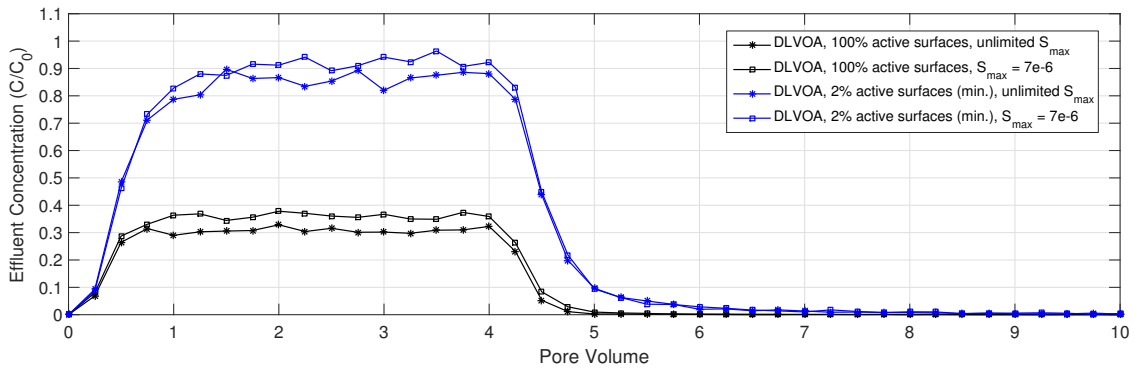

Figure 4.30: Breakthrough curves with unlimited surface capacity (S_{max}) and S_{max} = 7e-6 for two cases of active forces and d_p = 10 nm. DLVOA: attractive surface forces.

Table 4.12: Berea simulations with unlimited surface capacity (S_{max}) and S_{max} = 7e-6 for two cases of active forces. Fixed parameters: attractive (DLVOA) surface forces, Reynolds number = 3.37e-04, ρ_p = 1000 kg/m^3, d_p = 10 nm. SF: surface forces.

d_p (nm)	Active Surfaces (%)	Distribution of SF	S_{max}	Recovered in 10 PV (%)	In the domain after 10 PV (%)	Attached (%)
10	100	-	-	30.99	0.13	68.89
10	100	-	7e-6	36.32	0.17	63.51
10	2	Mineralogy	-	89.14	0.62	10.25
10	2	Mineralogy	7e-6	94.02	0.71	5.27

These results showed that, when S_{max} = 7e-6, some sites were filled and became unavailable for further attachment. Unlimited attachment, on the other hand, allowed more particles to attach on those sites. The maximum effluent concentration $C/C_0 = 1$ was not achieved likely because not enough particles were used in these simulations to fill all of the available sites.

Surface capacity results for the Berea were more prominent than in the micromodel. The smaller number of sites available for attachment in the Berea could be one of the factors that caused this difference.

4.6 Comparison with Other Models

The presented nanoparticle transport model was able to simulate 30,000 particles under different conditions. Compared to Li et al. (2012), the only work to do LPT in an XCT image, this was a great improvement in the number of particles as their simulations ranged from 500-4000 particles (to generate at least 100 particles attached). Some groups were able to simulate a large number of particles, but the geometry they used was simpler than XCT image-based porous media. Pham et al. (2014) simulated 100,000 particles but their computational domain consisted of a few pores. Longest and Xi (2007) simulated 300,000 particles in their airway model. However, the airway model was a much simpler geometry (Figure 4.31).

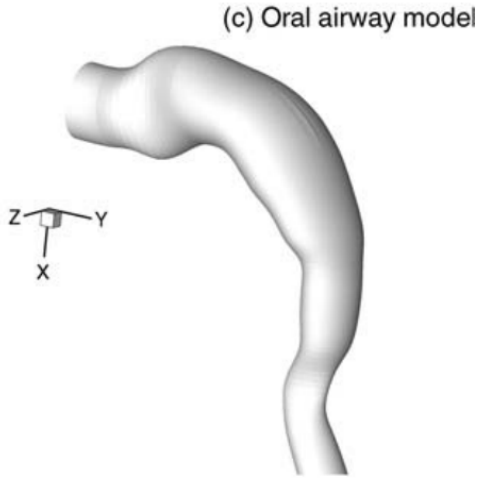

Figure 4.31: CT image-based idealized geometry of upper oral airways of the human respiratory system from Longest and Xi (2007).

The geometries used in this work were considerably more complex than geometries used in aerosol transport. However, aerosol flow fields are generally turbulent and turbulence terms need to be included the in LPT equations, greatly increasing the complexity of the problem.

The LPT methods presented by Longest and Xi (2007); Li et al. (2012); Pham et al. (2014) used a random release of particles at the entrance. This type of particle release could have increased the chance of particles to attach to the surfaces because there is an equal chance of particles starting close or far from a surface. The random flow rate biased particle release presented in this work prevents uniform distribution of particles across the entrance plane.

Finally, none of the LPT models simulated site blocking (or surface capacity) or XCT image-based mineralogy. These last two developments can greatly improve the understanding of NP transport and fate in porous media.

In addition to physical behaviors that were simulated, another advantage of presented model is the ability to track a single particle at each time step along its trajectory. Figure 4.32 gives an example of a few parameters that can be tracked at each time step for a single particle.

Furthermore, combining all of the information: XCT image, FEM results, unstructured mesh, and particle trajectories, into a powerful visualization software can provide valuable insights. Figure 4.33 shows two particle trajectories: one that experienced a lot of Brownian motion because it was close to the top cover (not shown in figure); and another that was away from the surface and the trajectory was smooth.

Figure 4.34 shows how visualization of the micromodel XCT image combined with FEM streamlines and the particle attachment location can enhance our understanding about NP transport. In Figure 4.34, it is clear that the particle was deposited in a stagnation point.

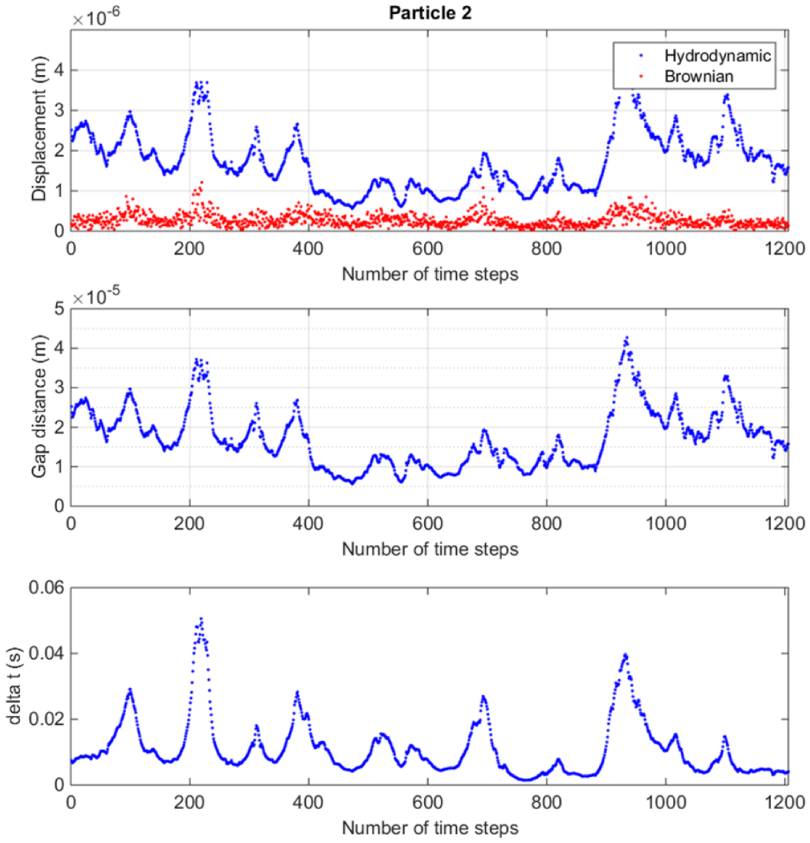

Figure 4.32: Example of different parameters that can be tracked at each time step. Top: Displacement due to hydrodynamic forces and Brownian motion; middle: gap distance (distance between wall and particle surface); bottom: Δt.

4.7 Summary and Conclusions

The model presented in this work successfully simulated nanoparticle transport in two porous media: micromodel and Berea. We compared the effect of particle diameter, attractive and repulsive surface forces, flow rate, particle density, surface capacity (site blocking), and image-based mineralogy.

Particle diameter affected the pattern of effluent concentration: larger particles exited earlier than smaller particles. However, the total NP recovery in 10 PV was not affected considerably. In the presence of attractive surface forces, NP recovery increased with particle

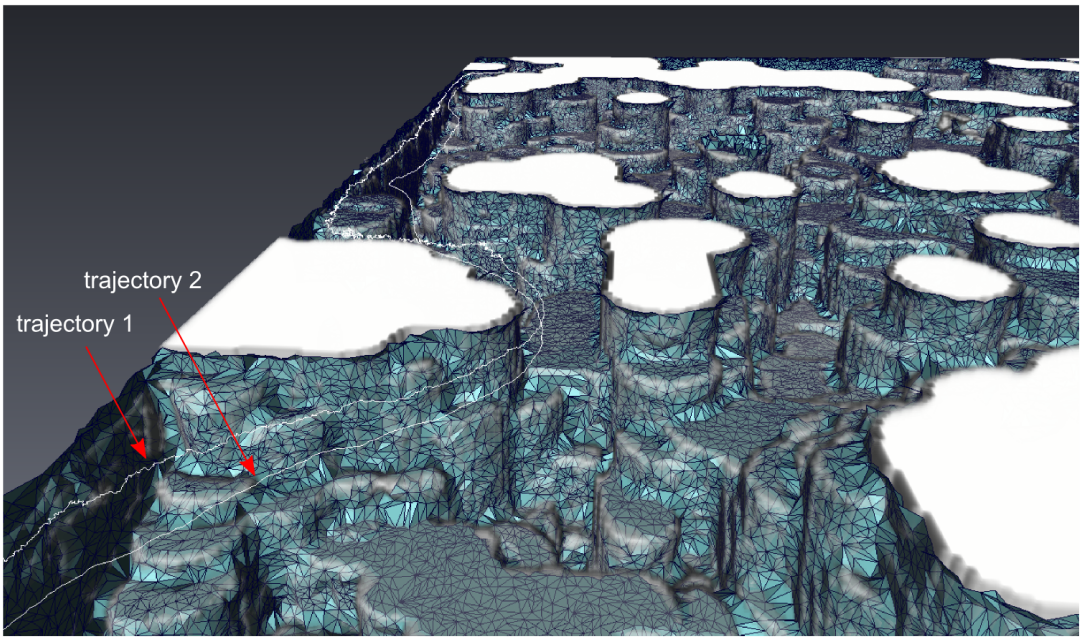

Figure 4.33: Particle trajectories. Trajectory 1: irregular path because particle was close to the top surface (not shown) and experienced a lot of Brownian motion; trajectory 2: smooth path because particle was away from the surface and mainly followed the streamline.

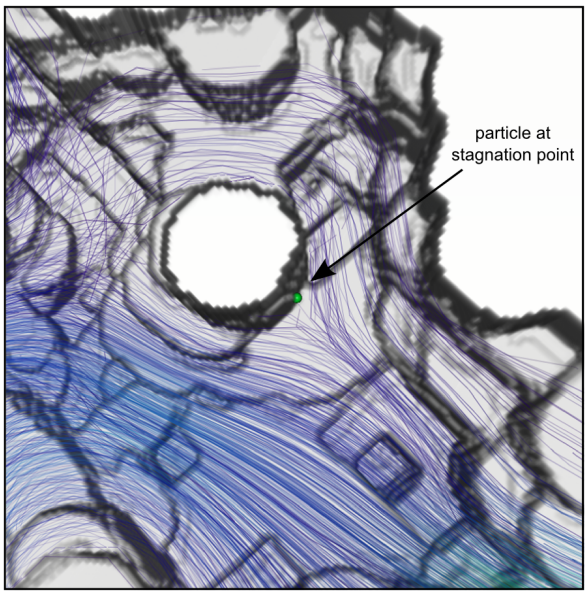

Figure 4.34: Combination of micromodel XCT image, FEM streamlines and particle attachment position shows particle deposited in a stagnation point. Flow is from left side, around circular feature, and down towards the bottom right corner. Note that the NP (green spehere) is not to scale.

diameter increased – an effect more evident in the micromodel. However, the two-orders-of-magnitude increase in surface force strength (micromodel only) had a minor effect in particle deposition. Repulsive surface forces facilitated the transport of NPs, increasing their recovery rate compared to no surface forces. This effect was more evident in the Berea, considerably changing the shape of the BTC. Flow rate (micromodel only) showed the biggest impact on NP recovery when attractive surface forces were present, especially for bigger particles. Particle density varying four orders of magnitude showed a negligible effect in the micromodel. Surface capacity affected particle attachment, a result that was more prominent in the Berea than in the micromodel. The effects of flow rate, attractive and repulsive surface forces were consistent with experimental data. However, increasing surface forces by two orders of magnitude or changing particle density did not affect particle transport, which disagrees with experimental results.

This work provided a methodology to analyze NP transport in porous media and to study factors that affect NP recovery and deposition. More simulations in realistic rocks in bigger domains are necessary to draw relevant conclusion. Direct comparison with experimental data and other models would also be valuable to further validate the presented model.

4.8 Bibliography

Broday, D. (2004). Deposition of Ultrafine Particles at Carinal Ridges of the Upper Bronchial Airways. *Aerosol Science and Technology*, 38(10):991–1000. 10.1080/027868290519076. 90

Buchgraber, M., Al-Dossary, M., Ross, C. M., and Kovscek, a. R. (2012). Creation of a dual-porosity micromodel for pore-level visualization of multiphase flow. *Journal of Petroleum Science and Engineering*, 86-87:27–38. 10.1016/j.petrol.2012.03.012. 89

Buchgraber, M., Clemens, T., Castanier, L., and Kovscek, A. (2011). A microvisual study of the displacement of viscous oil by polymer solutions. *SPE Journal*, 14(3):269–280. 10.2118/122400-PA. 89

Buckley, J. S. (1991). Multiphase displacements in micromodels. *Interfacial Phenomena in Petroleum Recovery*, 36:157–189. 90

Chuoke, R. L., van Meurs, P., and van der Poel, C. (1959). The instability of slow, immiscible, vis- cous liquid-liquid displacements in permeable media. *Petroleum Transactions, AIME*, 216:188–194. 89

Clemens, T., Tsikouris, K., Buchgraber, M., and Castanier, L. (2013). Pore-scale evaluation of polymers displacing viscous oil - computational fluid dynamics simulation of micromodel experiments. *SPE Journal*, 16(02):144–154. 10.2118/154169-PA. 89

Dill, K. A. and Bromberg, S. (2011). *Molecular driving forces: statistical thermodynamics in biology, chemistry, physics, and nanoscience.* London; New York: Garland Science. 99, 102

Elghobashi, S. (1994). On predicting particle-laden turbulent flows. *Applied Scientific Research*, 52(4):309–329. 10.1007/BF00936835. 91

Guha, A. (2008). Transport and deposition of particles in turbulent and laminar flow. *Annual Review of Fluid Mechanics*, 40(1):311–341. 10.1146/annurev.fluid.40.111406.102220. 91

He, F., Zhang, M., Qian, T., and Zhao, D. (2009). Transport of carboxymethyl cellulose stabilized iron nanoparticles in porous media: Column experiments and modeling. *Journal of Colloid and Interface Science*, 334(1):96–102. 10.1016/j.jcis.2009.02.058. 117

Johnson, W. P., Li, X., and Yal, G. (2007). Colloid retention in porous media: Mechanistic confirmation of wedging and retention in zones of flow stagnation. *Environmental Science and Technology*, 41(4):1279–1287. 10.1021/es061301x. 94

Lane, N. M. (2011). *Numerical studies of flow in porous media using an unstructured approach.* PhD thesis, Louisiana State University. 96

Larimi, M., Ramiar, A., and Ranjbar, A. (2014). Numerical simulation of magnetic nanoparticles targeting in a bifurcation vessel. *Journal of Magnetism and Magnetic Materials*, 362:58–71. 10.1016/j.jmmm.2014.03.002. 90, 91

Li, Z., Zhang, D., and Li, X. (2012). Tracking colloid transport in real pore structures: Comparisons with correlation equations and experimental observations. *Water Resources Research*, 48(5):1–11. 10.1029/2012WR011847. 92, 93, 111, 115, 116, 130, 131

Lin, D., Tian, X., Wu, F., and Xing, B. (2010). Fate and transport of engineered nanomaterials in the environment. *Journal of Environment Quality*, 39(6):1896–1908. 10.2134/jeq2009.0423. 94

Longest, P. W. and Xi, J. (2007). Effectiveness of direct Lagrangian tracking models for simulating nanoparticle deposition in the upper airways. *Aerosol Science and Technology*, 41(4):380–397. 10.1080/02786820701203223. 90, 92, 94, 98, 111, 116, 117, 130, 131

Lyklema, J., van Leeuwen, H., and Minor, M. (1999). DLVO-theory, a dynamic re-interpretation. *Advances in Colloid and Interface Science*, 83(1-3):33–69. 10.1016/S0001-8686(99)00011-1. 93

Ma, H., Pedel, J., Fife, P., and Johnson, W. P. (2009). Hemispheres-in-cell geometry to predict colloid deposition in porous media. *Environmental science & technology*, 43(22):8573–8579. 10.1021/es901242b. 98

Maynard, A. D. (2014). A decade of uncertainty. *Nature nanotechnology*, 9(3):159–60. 10.1038/nnano.2014.43. 88

Mehel, A., Tanière, A., Oesterlé, B., and Fontaine, J.-R. (2010). The influence of an anisotropic Langevin dispersion model on the prediction of micro- and nanoparticle deposition in wall-bounded turbulent flows. *Journal of Aerosol Science*, 41(8):729–744. 10.1016/j.jaerosci.2010.04.011. 92

Mills, G., Willson, C. S., Thompson, K. E., and Rivers, M. L. (2013). Assessment of image processing and resolution on permeability and drainage simulations through 3d pore-networks obtained using x-ray computed tomography. In *AGU Fall Meeting*, number H34E-01. American Geophysical Union. 95

Moller, T. and Trumbore, B. (2005). Fast , Minimum Storage Ray/Triangle Intersection. In *ACM SIGGRAPH 2005 Courses*, volume 7, pages 21–28, Los Angeles, CA. ACM. 10.1145/1198555.1198746. 104

Nelson, K. E. and Ginn, T. R. (2005). Colloid filtration theory and the happel sphere-in-cell model revisited with direct numerical simulation of colloids. *Langmuir*, 21(6):2173–84. 10.1021/la048404i. 99, 102, 111

Nowack, B. and Bucheli, T. D. (2007). Occurrence, behavior and effects of nanoparticles in the environment. *Environmental pollution*, 150(1):5–22. 10.1016/j.envpol.2007.06.006. 94

Park, D. S., Bou-Mikael, S., King, S., Thompson, K. E., and Willson, C. S. (2012). Design and fabrication of rock-based micromodel. In *ASME 2012 International Mechanical Engineering Congress and Exposition*, volume 9, pages 1–7, Houston, TX. ASME. 10.1115/IMECE2012-88501. 89, 93, 95

Pham, N. H., Swatske, D. P., Harwell, J. H., Shiau, B.-J., and Papavassiliou, D. V. (2014). Transport of nanoparticles and kinetics in packed beds: A numerical approach with lattice Boltzmann simulations and particle tracking. *International Journal of Heat and Mass Transfer*, 72:036304. 92, 94, 130, 131

Rangel-German, E. R. and Kovscek, a. R. (2006). A micromodel investigation of two-phase matrix-fracture transfer mechanisms. *Water Resources Research*, 42(3):1–13. 10.1029/2004WR003918. 89

Robinson, R. J., Oldham, M. J., Clinkenbeard, R. E., and Rai, P. (2006). Experimental and numerical smoke carcinogen deposition in a multi-generation human replica tracheobronchial model. *Annals of Biomedical Engineering*, 34(3):373–383. 10.1007/s10439-005-9049-5. 92

Roco, M. C. (2003). Broader societal issues of nanotechnology. *Journal of Nanoparticle Research*, 5(3-4):181–189. 10.1023/A:1025548512438. 88

Shi, H., Kleinstreuer, C., and Zhang, Z. (2006). Laminar airflow and nanoparticle or vapor deposition in a human nasal cavity model. *Journal of biomechanical engineering*, 128(5):697–706. 10.1115/1.2244574. 90

Tu, J., Inthavong, K., and Ahmadi, G. (2013). *Computational Fluid and Particle Dynamics in the Human Respiratory System*. Springer Netherlands, 1 edition. 10.1007/978-94-007-4488-2. 90, 91

Wan, J., Tokunaga, T. K., Tsang, C. F., and Bodvarsson, G. S. (1996). Improved glass micromodel methods for studies of flow and transport in fractured porous media. *Water resources ...*, 32(7):1955–1964. 10.1029/96WR00755. 90

Wang, X., Gidwani, A., Girshick, S. L., and McMurry, P. H. (2005). Aerodynamic Focusing of Nanoparticles: II. Numerical Simulation of Particle Motion Through Aerodynamic Lenses. *Aerosol Science and Technology*, 39(7):624–636. 10.1080/02786820500181950. 92

Weisstein, E. W. (n.d.). Circle packing. http://mathworld.wolfram.com/CirclePacking.html. 106

Yoon, J. S., Germaine, J. T., and Culligan, P. J. (2006). Visualization of particle behavior within a porous medium: Mechanisms for particle filtration and retardation during downward transport. *Water Resources Research*, 42(6):1–16. 10.1029/2004WR003660. 89

Zamankhan, P., Ahmadi, G., Wang, Z., Hopke, P. K., Cheng, Y.-S., Su, W. C., and Leonard, D. (2006). Airflow and deposition of nano-particles in a human nasal cavity. *Aerosol Science and Technology*, 40(6):463–476. 10.1080/02786820600660903. 92, 94

Zhang, T. (2012). *Modeling of Nanoparticle Transport in Porous Media.* Doctor, The University of Texas at Austin. 117

Zhang, T., Murphy, M. J., Yu, H., Bagaria, H. G., Yoon, K. Y., Neilson, B. M., Bielawski, C. W., Johnston, K. P., Huh, C., and Bryant, S. L. (2014). Investigation of nanoparticle adsorption during transport in porous media. *SPE Journal*, preprint(preprint):1–11. 94

Zypman, F. R. (2006). Exact expressions for colloidal plane-particle interaction forces and energies with applications to atomic force microscopy. *Journal of Physics: Condensed Matter*, 18(10):2795–2803. 10.1088/0953-8984/18/10/005. 102

5. Conclusions

X-ray computed tomography (XCT) successfully characterized proppant packs, proppant-filled fractures, and reservoir rocks under varying loading stress from 0 to 20 kpsi. The impact of loading stress on proppant packing structure, pore space morphology, and flow properties was investigated using XCT images and image-based flow modeling by two different methods: finite element (FEM) and Lattice Boltzmann (LBM).

XCT images of bulk proppant between Berea sandstone cores captured structural changes (e.g. arrangement, embedding) for different loading stresses and failure of proppants at the highest loading stresses. These results are consistent with other studies that indirectly measured these changes. Flow simulations showed that the reduction of high velocity was due to elimination of the largest flow channels, which in turn led to a more uniform velocity field.

XCT images of proppant monolayer between shale cores showed that crushing did not occur at high loading stress. However, proppant embedment was much more pronounced, which decreased the fracture width as well as fracture conductivity. As loading stress increased, narrowing of the main flow channels led to a more uniform velocity field.

The two image-based flow simulation approaches used here, FEM and LBM, predicted very similar permeabilities within the applied loading stresses. Finally, it is noteworthy that the permeability was essentially independent of loading at the lower stresses (below 12 kpsi or 83 MPa). This result differs from the manufacturer's data, which shows a correlation between loading and permeability over the entire range.

An increase in loading stress does not necessarily affect proppant packing and pore space morphology. As seen the the Berea-proppant system, minor changes occurred from 0 to 8

kpsi. Changes started to develop at 12 kpsi when a few proppants crushed. Major changes in proppant packing and pore space occurred at 20 kpsi when many proppants crushed. Thus, crushing was the most important effect that caused changes in packing and pore structure which, in turn, affected flow behavior.

The initial research questions from Section 1.1 can be answered:

1. Does the decrease in pore space due to increase in loading stress cause permeability reduction in the proppant-filled fractures?

   Yes, but only when the pore space actually decreased. At lower stresses, below 12 kpsi (83 MPa), the pore space remained fairly the same and so did permeability. When the pore space started to change as 12 kpsi, then permeability started to reduce. At 20 kpsi, when many proppants crushed and the porosity reduced, permeability also reduced.

2. How are the flow patterns affected when the pore space and morphology are changed?

   As loading stress increased, main channels were narrowed, leading to a more uniform velocity field with less spots of high velocity.

3. Is permeability reduction due to the increased loading stress greater in proppant monolayer than in bulk proppant?

   For the same range of loading stress (0 to 12 kpsi), the fracture permeability of the monolayer of proppants decreased more than the bulk permeability. However, the decrease in permeability for the bulk proppant from 0 to 20 kpsi was similar to the fracture permeability reduction from 0 to 12 kpsi.

As the second part of this work, a Lagrangian particle tracking (LPT) algorithm based on first principles of physics was successfully developed to model nanoparticle (NP) transport in porous media. This program can be used to study the effect of porous medium geometry, flow rate, particle size, and particle-surface forces on NP retention behavior. It provides effluent concentrations, location of retention sites, particle trajectories, and each component of particle displacement (e.g., displacement due to hydrodynamic drag or Brownian motion) at each time step. In addition, it allows visualization of retention sites and particle trajectories in combination with the porous media and flow field. This type of visualization can greatly increase our understanding about the mechanisms that affect particle fate and transport.

The two different geometries presented in this work, a Berea sandstone and a micromodel, showed the relevance of porous media geometry in NP transport. Although NP transport presented similar trends on both geometries, surface forces effects were more pronounced in the Berea. This showed the importance of using real rocks in NP transport models – as opposed to idealized structures used in other models.

The developed model successfully allows the implementation of realistic surface forces obtained experimentally, numerically, or empirically. The surface force data can be tabulated or a mathematical formulation, as for example, the DLVO forces used in this work.

The algorithms implemented when surface forces were neutral and particles were near the surface need to be further investigated. The use of two different algorithms resulted in considerably different particle transport behavior. A comparison with experimental data would allow us to determine the more accurate algorithm.

In order to make this code available to other researchers, further documentation is necessary. In addition, a user-friendly version needs to be written.

The research questions from Section 1.1 can be answered:

1. Does Lagrangian particle tracking accurately model nanoparticle transport in porous media?

   The effects of flow rate, attractive and repulsive surface forces were consistent with experimental data. However, increasing surface forces by two orders of magnitude or changing particle density did not affect particle transport, which disagrees with experimental results. Further validation is necessary to assert that LPT *accurately* model NP transport in porous media.

2. Does the addition of surface forces from molecular dynamics simulations and/or experiments improve NP transport model by providing more realistic results (when compared to core flooding experimental results)?

   Yes. The results of attractive surface forces and repulsive surface forces were consistent with experimental sand pack/core flood experiments. In addition, when flow rate was varied in the presence of attractive surface forces, our results presented similar trends as sand pack/core flood experiments and modified Colloid Filtration Theory (CFT).

3. Does the inclusion of XCT-determined mineralogy in NP transport model produce more realistic results?

   In the work presented here, only a comparison between XCT-determined mineralogy and no mineralogy was performed which seemed to improved the results. However, it is important to have a direct comparison with experimental results. For example, by using an XCT image of the same type of core that was used in a core flood experiment.

4. Can the NP transport model provide more detailed pore-scale information on NP deposition than current core flooding experiments by producing curves of effluent concentration and 3D map of particle deposition?

   A 3D map of particle deposition was fairly easy to be created in the micromodel because of its transparent top cover. For real rocks, the data is available to create a 3D map of particle deposition. However, further visualization attempts are necessary to produce valuable visual data.

A. Appendix – Article Sharing

Chapter 3 is a published article with DOI: http://dx.doi.org/10.1016/j.petrol.2015.09.017 and according to Elsevier Publishing "can be posted publicly by the awarding institution with DOI links back to the formal publications on ScienceDirect." (Attached below).

Article Sharing

Authors who publish in Elsevier journals can share their research by posting a free draft copy of their article to a repository or website. Researchers who have subscribed access to articles published by Elsevier can share too. There are some simple guidelines to follow, which vary depending on the article version you wish to share.

Published Journal Article

Policies for sharing published journal articles differ for subscription and gold open access articles:

Subscription articles

- If you are an author, please share a link to your article rather than the full-text. Millions of researchers have access to the formal publications on ScienceDirect, and so links will help your users to find, access, cite, and use the best available version
- Theses and dissertations which contain embedded PJAs as part of the formal submission can be posted publicly by the awarding institution with DOI links back to the formal publications on ScienceDirect
- If you are affiliated with a library that subscribes to ScienceDirect you have additional private sharing rights for others' research accessed under that agreement. This includes use for classroom teaching and internal training at the institution (including use in course packs and courseware programs), and inclusion of the article for grant funding purposes
- Otherwise sharing is by agreement only

Gold open access articles

- May be shared according to the author-selected end-user license and should contain a CrossMark logo, the end user license, and a DOI link to the formal publication on ScienceDirect.

Vita

Paula Sanematsu was born in São Paulo, Brazil. After she complete high school at Colégio Assunção, she attended Siena Heights University, Adrian, MI, where she played collegiate soccer and graduated in 2007 with a Bachelor of Science in Applied Mathematics and a Bachelor of Arts in Computer and Information Systems. In August 2010, she graduated from University of Tennessee Space Institute with a Master of Science in Mathematics degree. In December 2013, she was accepted as a doctoral candidate by the Interdepartmental Program in Engineering Science at Louisiana State University.